Study on Solid-Phase Crystallization Mechanism of Hydrogen-Doped Indium Oxide for Thin-Film Transistor Application

by

Xiaoqian Wang
Student ID Number: 1258011

A dissertation submitted to the
Engineer course, Department of Engineering,
Graduate School of Engineering,
Kochi University of Technology,
Kochi, Japan

in partial fulfillment of the requirements for the degree of
Doctor of Engineering

Assessment Committee:

Mamoru Furuta
Norbert Frühauf, University of Stuttgart
Toshiyuki Kawaharamura, Kochi University of Technology
Chaoyang Li, Kochi University of Technology
Hisao Makino, Kochi University of Technology

March 2025

Abstract

Study on Solid-Phase Crystallization Mechanism of Hydrogen-Doped Indium Oxide for Thin-Film Transistor Application

With the rapid development of computer and network technologies, there is an increasing requirement for personalized and intelligent information exchange interfaces. These advancements are inseparable from the development of new display technologies and materials. Flat panel display (FPD) technology, as a significant component of the display technology field, has gradually been applied to various aspects of daily life and industrial applications. Thin-film transistors (TFTs), which play a crucial role in FPD technology, have attracted considerable attention. In particular, the performance of thin film materials used in TFT devices is a critical factor that directly determines the display quality and performance of FPD.

Metal oxide semiconductors have attracted great attention for use as channel layers of thin film transistors (TFTs) for next-generation flat-panel displays, gas sensors, biosensors, and so on. Compared to amorphous Si TFTs, which show field-effect mobility of approximately 1 cm^2/Vs, and LTPS (low temperature polycrystalline silicon), which requires a fabrication temperature above 600°C, metal oxide semiconductors, represented by In-Ga-Zn-O (IGZO), can be deposited at room temperature and exhibit high field-effect mobility of more than 10 cm^2/Vs. However, further improvement in field-effect mobility is required to expand their applications. Many oxide semiconductors with various cation combinations have been reported. The composition of amorphous oxide semiconductors becomes more complex.

Among metal oxide semiconductors, single-crystal indium oxide exhibits a considerably high Hall mobility of as high as 160 cm^2/Vs, making it a candidate material for high-performance thin-film transistor (TFT) applications. The large spatial spread and significant overlap of the In 5s orbital facilitate efficient electron transport, resulting in high electron mobility. However, InO_x films show a high carrier density of over 10^{19} cm^{-3}, which is unsuitable for TFT application. Currently, impurities having a high bond dissociation energy with oxygen, such as Sn, Ti, W, Ce, Zn, and Ga, were doped into amorphous indium oxide (InO_x) films to suppress the carrier density of the film. However, the dopant of impurity element reduces the mobility of amorphous oxide semiconductors (AOS), requiring a trade-off between these factors.

In addition to AOS, polycrystalline semiconductors are also considered promising materials due to their excellent electrical properties. Hydrogen is one of the most common types of impurities, which usually acts as a shallow donor in semiconductors. It is reported that hydrogen-doped InO_x (InO_x:H) films showed a high Hall mobility of over 100 cm^2/Vs after annealing in N_2 at 250℃ with film converted to a polycrystalline phase. A thin film transistor with field-effect mobility of 139 cm^2/Vs was fabricated using InO_x:H films as the channel layer. Nevertheless, despite the fact that H is the most common impurity, its role and influence in each particular case can vary significantly. The mechanism of crystallization and metal-semiconductor transition and the role of hydrogen in polycrystalline film require further study and comprehensive analysis, while the mechanism still remains without proper explanation.

In this study, in order to improve electrical properties of InO_x:H films and enable its application in TFT fabrication, the mechanisms of solid-phase crystallization (SPC) and metal-semiconductor transition were systematically investigated. In addition, hydrogen,

as a dopant in InO_x:H, was investigated for its role in solid-phase crystallization (SPC) and metal-semiconductor transition (MST)

The purpose of this dissertation is to comprehensively elucidate the characteristics of InO_x before and after crystallization, the significant changes in electrical properties caused by hydrogen doping, and their fundamental mechanism. To achieve nondegenerate InO_x/InO_x:H films, the roles and variations of critical factors throughout the process—from film deposition to the completion of post-deposition treatment—are systematically investigated to understand the mechanism of metal-semiconductor transition.

Chapter 1 Introduction

As a background of this dissertation, this chapter shows an overview of the background and current development of semiconductors for application on thin film transistors. Then, we present and compare the performance of various channel materials, providing an overview of the characteristics, advantages, and limitations of these semiconductor materials. The subsequent sections focus on the history, development, recent advancements, and characteristics of metal oxide semiconductors. The chapter focuses on the role and effect of hydrogen in amorphous and polycrystalline semiconductors. The change in electrical properties, passivation of defects, and improvement in device performance were discussed.

Chapter 2 Fabrication techniques and characterization techniques

The working principles, apparatus structures, and parameters of the fabrication techniques (magnetron sputtering, rapid thermal annealing) and characterization techniques (Hard X-ray photoelectron spectroscopy, Scanning Electron Microscopy, X-

ray diffraction, Thermal Desorption Spectroscopy, and Hall measurement) were systematically described.

Chapter 3 Improvement of electrical properties of indium oxide films by hydrogen doping

This chapter describes the research of InO_x and InO_x:H film with different deposition conditions before and after annealing.

It was preliminarily demonstrated that undoped InO_x film did not show a significant improvement in electrical properties even after annealing in N_2. In contrast, hydrogen-doped InO_x film exhibited a notable increase in Hall mobility of ~70 cm^2/Vs after annealing at 250 ℃ in N_2.

In comparison to InO_x films, the introduction of hydrogen caused a decrease in Hall mobility of as-deposited film due to an increase of impurity scattering from hydrogen. Then, Hall mobility increased significantly after annealing at above 200 ℃ in N_2, regardless of the hydrogen flow ratio. On the other hand, a decrease of the oxygen flow ratio increases the SPC temperature of InO_x:H film. Therefore, oxygen deficiency in the InO_x:H film prevents the formation of a substantial amount of hydrogen-oxygen bonds, leading to the presence of significant amount of hydrogen as interstitial hydrogen within the film. Excess interstitial hydrogen was desorbed as H_2 and H_2O during SPC, which require more energy.

Even extending the annealing time to 60 min, electrical properties, and grain size did not change, indicating good stability for TFT application.

Chapter 4 Solid phase crystallization mechanism in Hydrogen-doped InO_x

films

It is presented that SPC occurred when hydrogen-doped InO_x film was annealed at a low temperature of 250 ℃ in N_2, resulting in a significant increase of Hall mobility. Most of the SPC poly-InO_x:H have focused on their film thickness of more than 100 nm for TCO applications. On the other hand, there are few papers on the study of the SPC poly-InO_x:H for TFT applications with a thickness of less than 50 nm. The understanding of SPC process for very thin (<50 nm) InO_x:H film, such as nucleation density and lateral growth rate, is essential for TFT applications.

In this chapter, nucleation and grain growth were discussed as a means of clarifying the mechanism of the rapid solid phase crystallization (SPC) process from H_2-doped amorphous indium oxide (InO_x:H) films. H_2-doping in InO_x:H films reduced nucleation density at 250 ℃ from 4.1 to 1.1 μm^{-2}, resulting in an increase of grain size and Hall mobility of the poly-InO_x:H films. Lateral growth rate from the nucleus was estimated to be 220 nm/min for the InO_x:H film at 250 ℃. Thus, an amorphous InO_x:H film could be converted to a poly-InO_x:H film within 3 min owing to a fast lateral growth rate from the nucleus. Almost the same grain size, Hall mobility, and carrier density could be obtained from the poly-InO_x:H films after annealing at 250 ℃ only for 3 min, irrespective of the ramp rate. The results demonstrated a wide range of processing windows of the SPC for poly-InO_x:H films.

Chapter 5 Metal-semiconductor transition mechanism of InO_x:H film

In this chapter, Nondegenerate poly-InO_x:H films were formed by rapid SPC in air. Defect passivation and band structure were discussed as a means of clarifying the mechanism of metal-semiconductor transition. Hydrogen in InO_x:H films act as shallow

donors, providing free carriers, resulting in degenerate as-deposited InO_x:H films with higher carrier density than InO_x films. Ionized H, which provided a portion of carrier, was desorbed as H_2O at temperature of 200 ℃, causing reduction of carrier density. The doping of H promoted the formation of V_O. Reduction in relative area ratio of V_O was observed after annealing in N_2, caused by crystal rearrangement. Oxygen vacancy decreased with the decrease of near E_F states, indicating that oxygen vacancy acts as shallow donor in InO_x:H films. Finally, these caused the decrease in carrier density.

Carrier density of the InO_x:H films significantly decreased to ~10^{17} cm^{-3} after SPC in air at 250 ℃. Relative area ratio of V_O in InO_x:H films shows a more substantial decrease as compared to the films annealed in air, decreasing from 37.10% to 3.23%, with near E_F states decreasing to extreme low state. In contrast, the near VBM states increased with annealing, caused by -OH. Extremely low relative area ratio of the V_O and the suppression of carriers by -OH jointly result in the formation of nondegenerate InO_x:H films.

Intrinsic oxygen in InO_x:H films, controlled by deposition conditions, plays an important role in the metal-semiconductor transition at low temperature. Degenerate InO_x:H films with sufficient intrinsic oxygen can be converted to a nondegenerate state after annealing in air at temperature below 250 ℃.

Chapter 6 Conclusion

The main results obtained from this research work are summarized.

Table of contents

Chapter 3

Improvement of electrical properties of indium oxide films by hydrogen doping

Chapter 4

Solid phase crystallization mechanism in Hydrogen-doped InO_x films

List of Figures

List of Tables

Chapter 1

Introduction

1.1 Background

In the modern digitalizing society, one of the core components of visual output devices is display, the development of which plays a crucial role in enhancing interactivity and efficiency in information transmission. Display technology developed from cathode ray tube displays (CRTs)[1] to liquid crystal displays (LCD)[2], organic light emitted diode (OLED)[3], as well as other advanced technology, since the early 20th century. As technology evolves and consumer requirements diversify, display technology encounters unparalleled opportunities and challenges for development. Currently, the rising popularity of augmented reality (AR) and virtual reality (VR) devices highlights the significance of display technology.

Figure 1. 1[4] shows the difference between the image qualities for different display pixel density. The pixel density of a typical smartphone is about 400 ppi. So, it looks rough when the display is enlarged with a VR device lens. Thus, higher pixel density is required for display for the application of VR equipment.

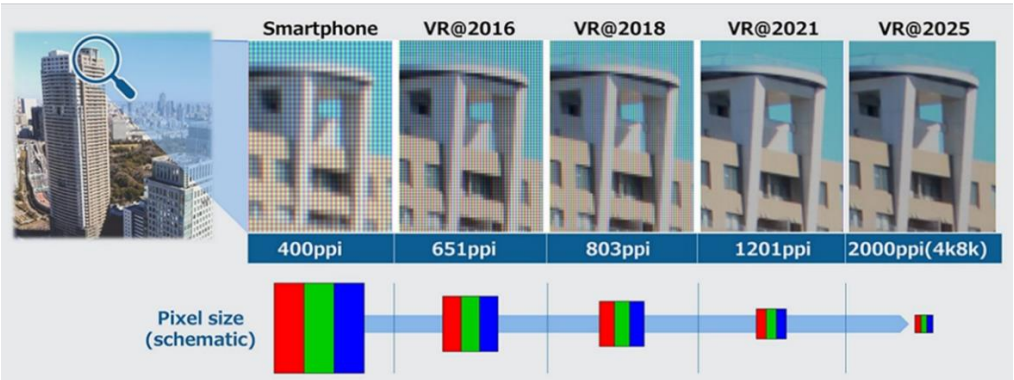

Figure 1. 1 Difference between the image qualities for different display pixel density.[4]

The essential feature of VR devices is the sense of immersion into the world of images. Therefore, realistic image quality, motion blur suppression, and low latency are necessary. To achieve devices with high performance, resolution, pixel density, and refresh rate were required, as shown in Figure 1. 2.[4]

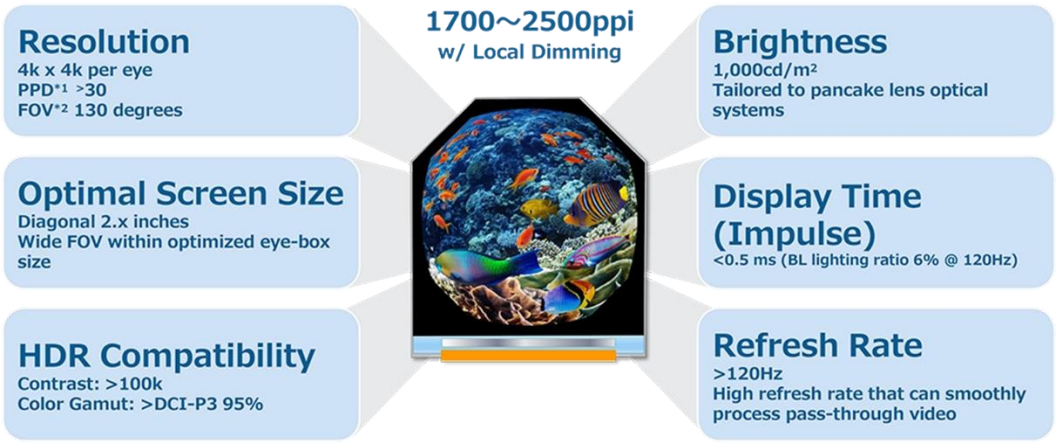

Figure 1. 2 Requirements for displays in VR devices.[4]

In addition to displays, electronic devices, such as sensors and nonvolatile memories, are also required to achieve high performance as well as upgraded energy efficiency, reduced costs, and improved integration for further application. A fundamental component of these technologies is the transistor, particularly the thin-film transistor (TFT) used for operating flat-panel displays (FPD) and sensors. Figure 1. 3 shows the required field effect mobility of active matrix TFTs for next-generation displays. To achieve super-high-definition TVs and operate various devices, the required mobility increased to be over 10 cm^2/Vs, which is an impossible value for amorphous silicon technology (< 1 cm^2/Vs). Polycrystalline Si exhibited high field effect mobility of ~100 cm^2/Vs. It is possible to crystallize by supplying a large amount of thermal energy (≈1000 ℃). However, the substrates that are usually used cannot withstand the high

annealing temperature above 600 ℃. Oxide semiconductors exhibited a high field effect of 10 cm^2/Vs with lower process temperature and cost than LTPS, making them a strong candidate for TFT.

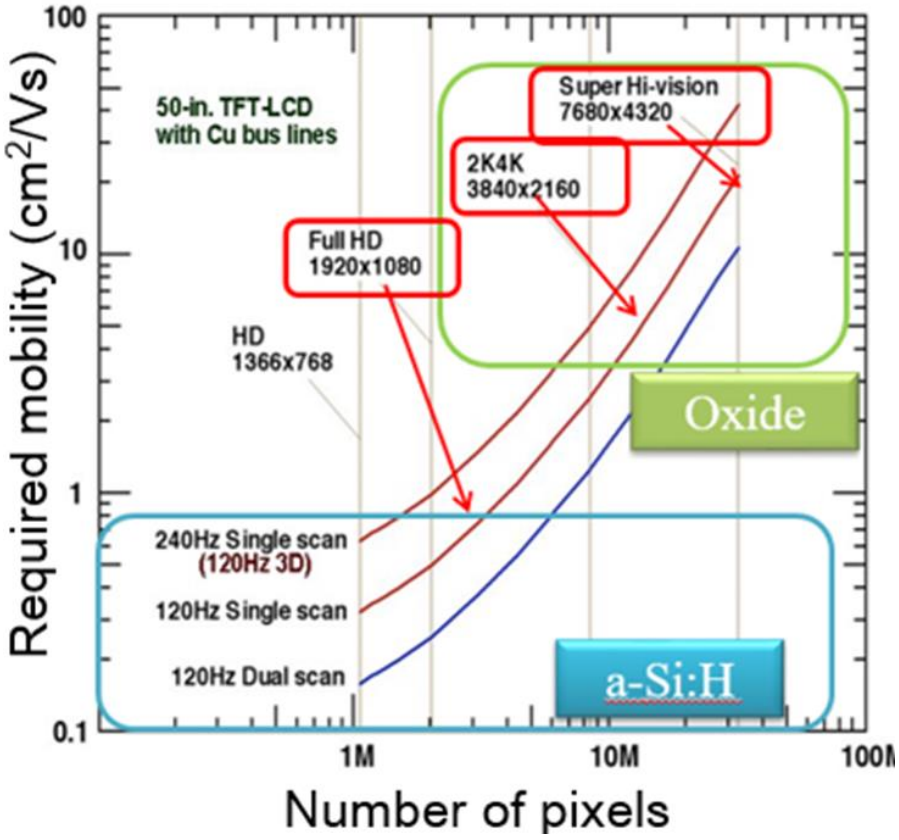

Figure 1. 3 Required field effect mobility of active matrix TFTs for next-generation displays.[5]

Table 1. 1 summarizes common semiconductor materials. Electrical properties, fabrication conditions, and cost were compared. Polycrystalline oxide semiconductors have big advantages compared with a-Si and LTPS, such as Higher mobility, low process temperature, and production cost, making them strong candidates for next-generation displays.

Table 1. 1 Summary of semiconductor properties, formation condition, and cost.

TFT properties	a-Si:H	LTPS	Amorphous oxide semiconductor	Polycrystalline oxide semiconductor
Field effect mobility (cm^2/Vs)	< 1	~300	> 10	> 60
Formation method	PECVD	PECVD + Excimer Laser Annealing (ELA)	Sputtering	Sputtering + solid phase crystallization
Process temperature (℃)	150 ~ 350	> 400	RT~300	RT~300
Thermal Process time		A few tens of nanoseconds	60 ~ 90 min	3 ~ 90 min
Cost	Low	High	Low	Low

The fundamental operation of TFTs heavily relies on semiconductor materials, which are essential to the transistor structure. Understanding the role of semiconductors in TFT technology is crucial for enhancing display performance and efficiency since semiconductors directly influence speed, energy consumption, and the overall quality of electronic displays. In addition to TFTs, semiconductors are involved in nearly all fields related to electronics and information technology, making them the core foundation of modern electronics industry. The worldwide semiconductor market is anticipated to rise from $600 billion in 2021 to $1 trillion by 2030, as shown in Figure 1. 4.

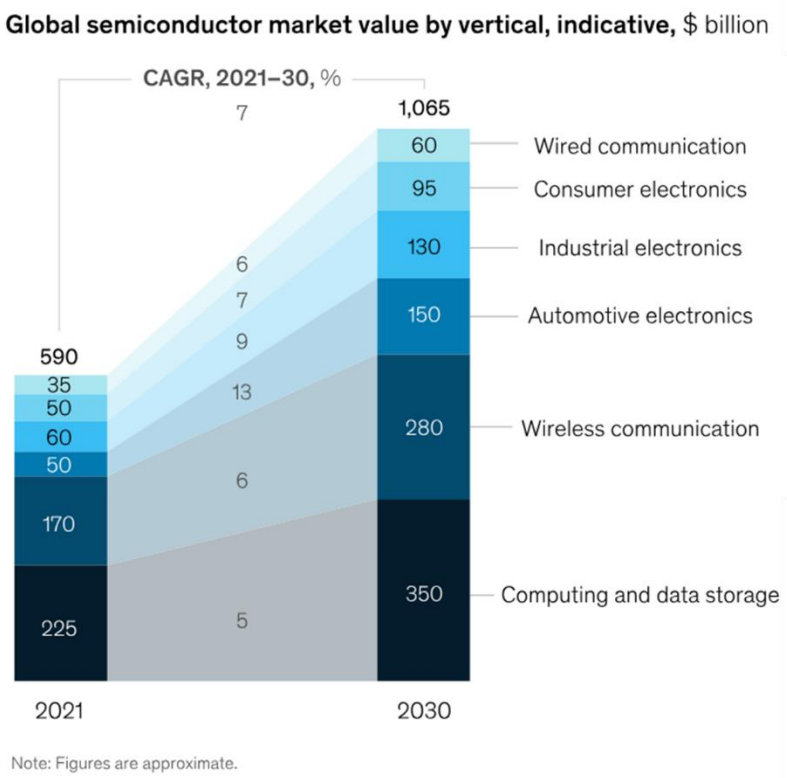

Figure 1. 4 Global semiconductor market.[6]

1.2 Historical overview of oxide semiconductors

The history of semiconductor development for display technology applications begins in the middle of the last century. Figure 1. 5 shows the timeline of semiconductor and TFT development. The initial bipolar transistor was introduced by Bell Telephone Laboratories in the 1940s, promoting the evolution of computers from room-sized ENIAC to desktop devices.[7,8] In the late 1960s, the first operational thin-film transistor was designed using CdS by Weimer et al.[9] Subsequently, Klasens and Koelmans successfully employed a semiconducting metal oxide in TFTs in 1964.[10] Le Comber and Spear proposed photoelectric properties of amorphous silicon. Amorphous silicon cannot be used for TFT fabrication due to its high carrier density. Spear et al. utilized hydrogenated amorphous silicon (a-Si:H) as a thin-film transistor material for operating

active-matrix LCD.[11] The development of a-Si:H attracted attention due to its low-cost, large-area semiconductor films, which are suitable for TFTs and solar cell fabrication.[12] LCD driven by a-Si:H replaced CRT displays, making TV, mobile phone, and computer screens thinner and lighter with lower costs. With the improvements in thin-film deposition and doping techniques, polycrystalline silicon (poly-Si) emerged as a key semiconductor material for TFTs in displays. Poly-Si TFTs offered higher carrier mobilities and better stability than a-Si:H, paving the way for advanced display backplane technologies.[13] Hosono et al. proposed transparent electronic conducting amorphous semiconductors, demonstrating amorphous metal oxides exhibited both high transparency and semiconductor properties in 1996.[14] A major breakthrough in transparent and flexible electronics was the demonstration of Indium Gallium Zinc Oxide (IGZO) TFTs by Hosono in 2004.[15,16] IGZO offered higher electron mobility and better uniformity than a-Si:H film, enabling next-generation and flexible displays. At the beginning of 2010, Kris Myny and Paul Heremans developed the organic transistor, an innovative nanoelectronics device.[17] The research indicated substantial progress in organic electronics and enabled the growth of flexible and printable electronics. Currently, TFT with further enhancement in electrical properties, process temperature, and cost is required. Magari et al. reported TFT with high field effect mobilities of 139 cm^2/Vs using In_2O_3:H as a channel layer in 2022.[18]

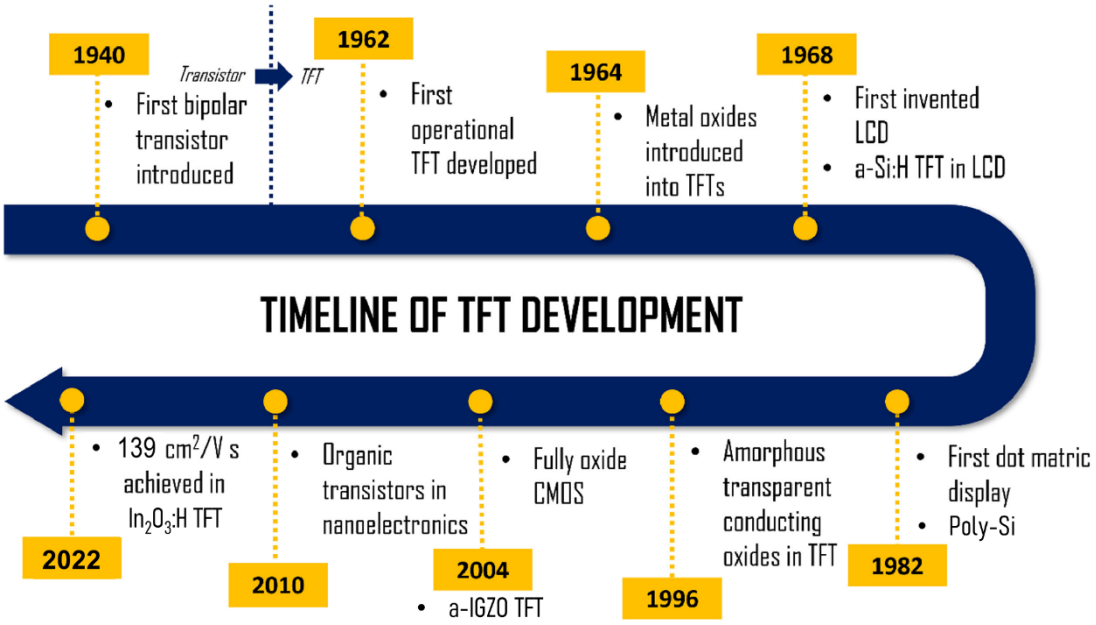

Figure 1. 5 Diagram indicating the recorded timeline of TFT development.[19]

1.3 Amorphous oxide semiconductors (AOS)

Oxide semiconductors are a class of materials widely known for their diverse electronic, optical, and chemical properties. They have attracted significant attention in recent decades due to their transparency, simple fabrication process, low fabrication temperature, and high electrical properties. Compared to LTPS, oxide semiconductors require low process temperature and cost, making it a wider application aspect, such as next-generation flat-panel displays [20–22], gas sensors [23,24], biosensors [25], neuromorphic systems [26], and nonvolatile memories [27] and high power electronics, as shown in Figure 1. 6.

Figure 1. 6 A variety of applications and emerging technologies based on wide bandgap oxide semiconductors.[28]

1.3.1 Electronic structure and unique feature of AOS

Following the progression of hydrogenated amorphous silicon (a-Si:H), high-temperature annealed polycrystalline silicon (HTPS), laser-annealed low-temperature polycrystalline silicon (LTPS), and organic semiconductors, AOS has emerged as a novel material system uniquely suited for large-area semiconductor devices.

AOS is a new semiconductor material system for large-area semiconductor devices that came into prominence following hydrogenated amorphous silicon (a-Si:H), high-temperature annealed polycrystalline silicon (HTPS), laser-annealed low-temperature

polycrystalline silicon (LTPS), and organic semiconductors.

Hosono et al. reported transparent electronic conducting amorphous semiconductors, demonstrating amorphous metal oxides exhibited both high transparency and semiconductor properties with wide band gap. An electronic configuration, according to equation 1.1 for heavy metal cations (HMC), was proposed as a new material design concept.

$$M\text{: } (n-1)d^{10}ns^{0}\ (n \geq 5), \tag{1.1}$$

where M is metal cation, n is principal quantum number, describes the electron's state.[29] Figure 1. 7 shows the schematic illustration of the carrier transport paths in covalent semiconductor and oxide semiconductors. In a crystalline system such as silicon, electrons may be envisioned as traveling along the sp^3 orbitals of the constituent atoms, which overlap in a regular lattice arrangement commonly referred to as sp^3 hybridization (illustrated in Figure 1. 7(a), top). However, if the crystal structure is disrupted by defects, or the material is amorphous, this conduction pathway is broken (Figure 1. 7(a), bottom), leaving electrons to hop between orbitals in a process known as tail-state hopping.[30] This dramatically reduces the mobility of the material from 1000 cm^2/Vs to 0.05 cm^2/Vs.[31] In contrast, metal oxide semiconductors do not depend on the overlap of sp^3 orbitals to form the conduction band pathway. Instead, they rely on different mechanisms to facilitate electronic conduction. The large s orbitals associated with the transition metal cations overlap to provide a conduction path, as shown in Figure 1. 7(b). Because the s orbitals are spherically symmetrical, this overlap is the same whether the atoms are ordered in a regular crystal structure or completely disordered in the amorphous form.[32,33] It should be noted that the mobility in the a-IGZO is also lower than that of c-IGZO, which is also due to the presence of a large number of different defects. However,

to obtain the single-crystalline films of such complex structure oxides, a high temperature of about 1400 °C is required. Based on the same theoretical system, a-$AgSbO_3$, a-Cd_2GeO_4, and a-Cd_2PbO_4, with Hall mobility about 10 cm^2 /Vs, which are one order larger compared to a-Si:H, were reported.[15] There are two research directions for further study: polycrystalline and amorphous.

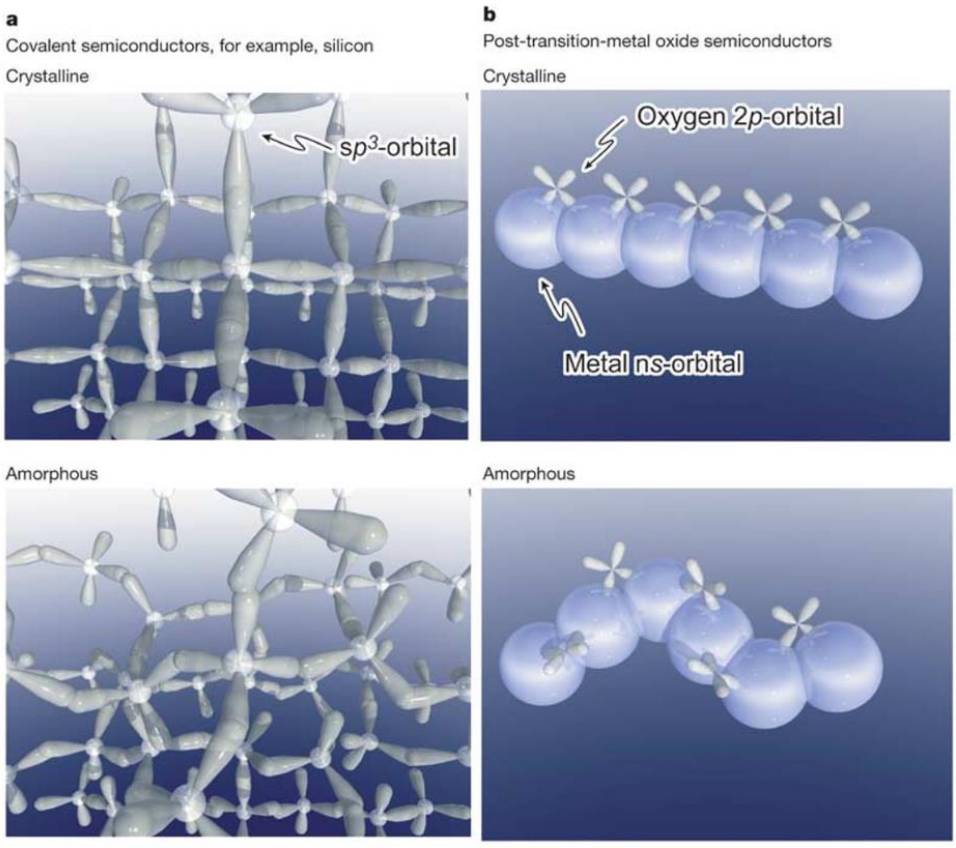

Figure 1. 7 Schematic illustration of the carrier transport paths in covalent semiconductor and oxide semiconductors: (a) c-Si; (b) a-Si; (c) c-IGZO; (d) a-IGZO.[15]

1.3.2 Electronic transport and origin of high mobility

The electron transport properties exhibit a peculiar behavior, as shown in Figure 1. 8(a). Compared to conventional covalent amorphous semiconductors, definite Hall voltages,

and electron mobilities can be observed for AOSs through usual Hall measurements. Hall mobility increased with the increase of carrier density. This trend is opposite to that observed in simple crystalline semiconductors and may be explained by percolation conduction as shown[32] in Figure 1. 8(b).

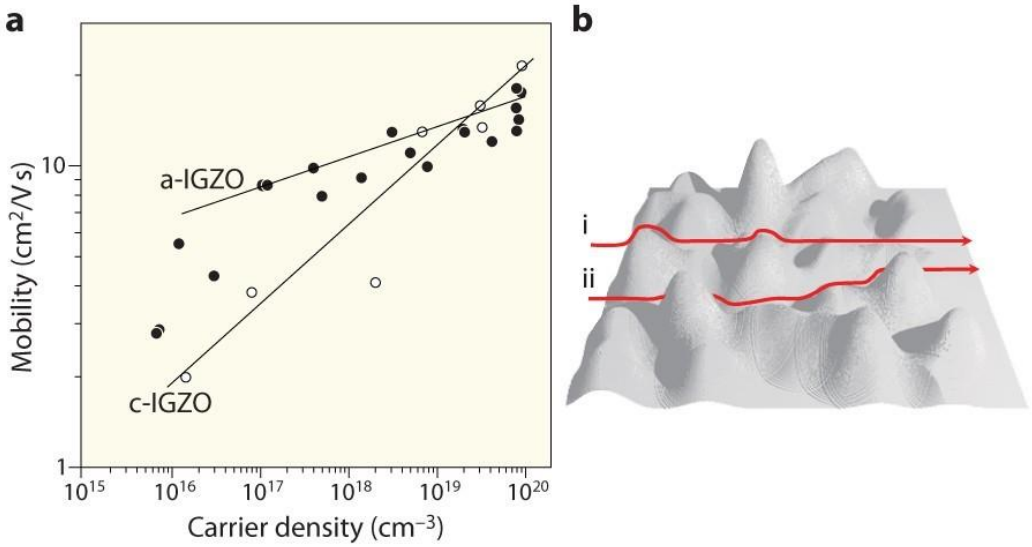

Figure 1. 8 Carrier transport in a-IGZO. (a) Relationship between Hall mobility and carrier density for c-IGZO and a-IGZO. (b) Illustration of percolation conduction showing examples of (i) a shorter path and (ii) a longer winding path. The isosurface represents the electron potential in the conduction band.[32]

Amorphous IGZO TFTs exhibit high field-effect mobility of more than 10 cm^2/Vs and excellent uniformity.[15,34] However, instability in amorphous IGZO thin-film transistors is problematic, especially light instability, which originates from V_O and hydrogen-related defects.[35] In addition to instability, further improvement in field-effect mobility is required to expand their applications. Active efforts have been performed to increase field-effect mobility and stability of AOS TFTs, such as optimization of the composition of the AOSs,[36–38] develop other IGZO thin film fabrication technologies[39], film thickness reduction[40], surface treatment, and

annealing in high oxygen atmosphere[41–43]. In addition, impurities having a high bond dissociation energy with oxygen, such as Sn, Ti, W, Ce, Zn, and Ga, were doped into amorphous indium oxide (InO_x) films to improve field-effect mobility of AOSs TFTs. [44–49] Multi-component AOSs have been widely investigated for use in TFTs. [50–52] However, the use of multi-component AOSs complicates the control of film composition and electrical properties.

1.4 Polycrystalline oxide semiconductors

Until now, many oxide semiconductors with various cation combinations have been reported. The composition of amorphous oxide semiconductors becomes more complex. Figure 1. 9 shows the relationship between the mobility and the composition of indium oxide, gallium oxide, and zinc oxide. Compared to AOSs, single crystalline or polycrystalline oxide semiconductors exhibited high mobility and low concentration of defects such as V_O.[53,54] Among them, indium oxide is a promising material for high-mobility TFTs since single-crystal Hall mobility of 160 cm^2/Vs has been reported.[55] The fabrication of single-crystal indium oxide requires stringent equipment and experimental conditions, which makes large-scale production challenging.[55]

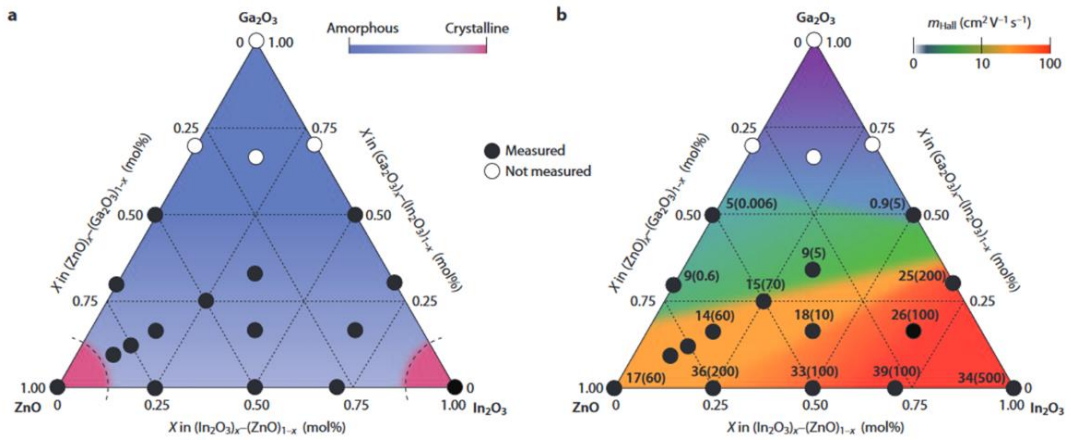

Figure 1. 9 (a) Amorphous and crystalline formation and (b) electron transport properties of thin films in relation to different compositions. [32]

In the 1950s, polysilicon was used as a substitute for single-crystal silicon in the fabrication of early transistors. During the 1990s, low temperature polycrystalline silicon (LTPS) was obtained with high field effect mobility of ~300 cm^2/Vs, which are essential for high performance macroelectronics due to their higher field-effect mobility.[56,57] To achieve LTPS films with high electrical performance, excimer laser annealing (ELA) method is an essential technique for crystallization, as shown in Figure 1. 10.[58–61]

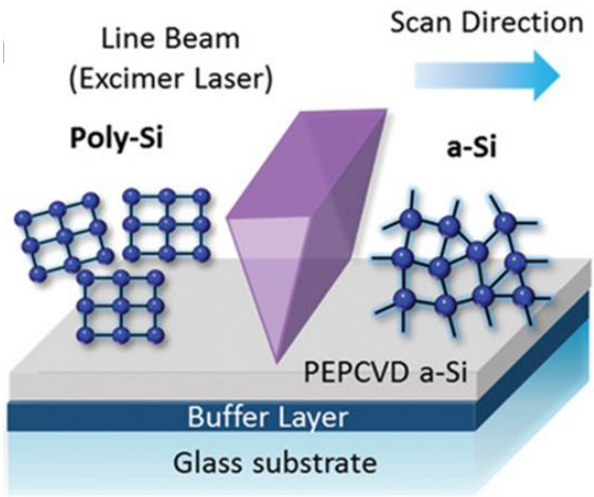

Figure 1. 10 Schematic of ELA-induced phase transformation from a-Si to LTPS.[58]

In the 2000s, polycrystalline ZnO was used in varistors and UV detectors.[62] Polycrystalline In_2O_3 was used as a transparent conductive oxide (TCO) in touch screens due to its high electrical properties. Thus, the crystallization of oxide semiconductors has attracted widespread attention.

Amorphous oxide semiconductors show long-range disorder, short-range order, and no grain boundaries. Polycrystalline oxide semiconductors show long-range order and grain boundaries. Polycrystalline oxide semiconductors showed high electrical properties due to the existence of crystal. Oxygen vacancy contributed to the free carrier as shallow donor. The mobility of polycrystalline oxides is determined by two main mechanisms: electron transport in the grains themselves and grain boundary scattering.[63]

1.5 Role of hydrogen in oxide semiconductors

Hydrogen is one of the most common types of impurity and displays a range of complex behaviors when introduced in semiconductors. Hydrogen can be found in deposition chamber in a form of residual H_2O or H_2 molecules.

Hydrogenated amorphous silicon (a-Si:H) is the most commonly used material for large-area electronic and optoelectronic devices because it can be deposited as thin layers, which absorb light much more efficiently than crystalline silicon, in which crystal momentum conservation restricts optical transitions, and because it can be doped both n-type and p-type, allowing the manufacture of junction devices and thin-film transistor.[64,65] Hydrogenation is important for controlling native defect density. The role of hydrogen in passivation of the dangling bonds in a-Si:H was shown in Figure 1. 11. a-Si:H was commonly used to fabricate back panel of LCD, with field effect mobility below 1 cm^2/Vs [66]. a-Si:H has advantages in low process temperature, low cost, and

high uniformity. However, a-Si:H has a disadvantage in terms of its bias instability and low electrical performance, which make it difficult to meet the requirements for high-performance TFTs.

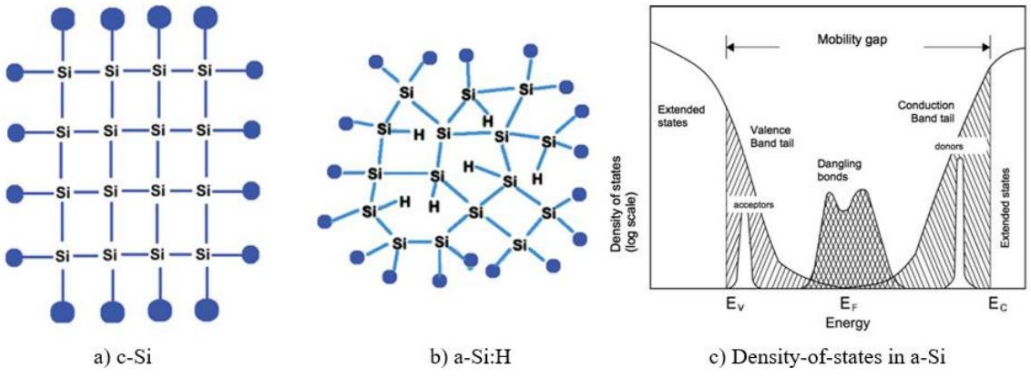

Figure 1. 11 Schematic representation for the structures of (a) c-Si; (b) a-Si:H; (c) density-of-states in subgap of a-Si.[67]

Hydrogen usually exists in oxide semiconductors in the form of interstitial H, substitutional H, and -OH by first-principles calculations, as shown in Figure 1. 12. Oxygen vacancy increased with the introduction of hydrogen, resulting in the increase of electron density from 4.0×10^{19} cm^{-3} to 3.1×10^{20} cm^{-3}.[68] Koida et al. have reported polycrystalline hydrogen-doped In_2O_3:H with high Hall mobility of over 100 cm^2/Vs, making it a promising candidate for TCO. However, there are few researches about crystallization and metal-semiconductor mechanism of thin poly-In_2O_3 films.

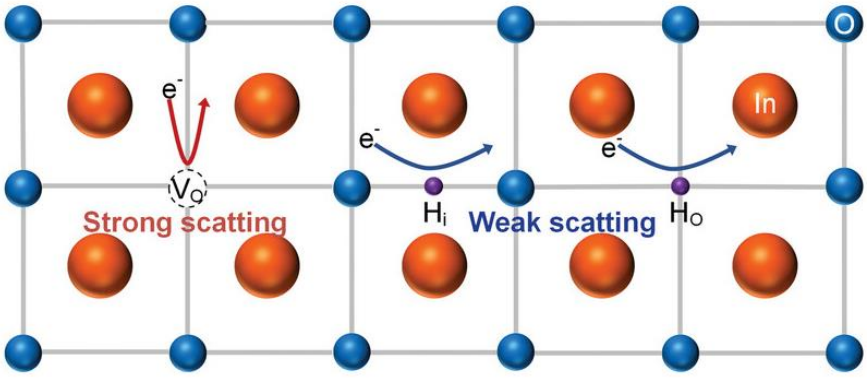

Figure 1. 12 Schematic diagram of In_2O_3:H Crystal structure, including defect scattering.[68]

References

1. Badano, A. Principles of Cathode-Ray Tube and Liquid Crystal Display Devices.
2. Kawamoto, H. The History of Liquid-Crystal Displays. Proceedings of the IEEE 2002, 90, 460–500, doi:10.1109/JPROC.2002.1002521.
3. Geffroy, B.; le Roy, P.; Prat, C. Organic Light-Emitting Diode (OLED) Technology: Materials, Devices and Display Technologies. Polymer International 2006, 55, 572–582, doi:10.1002/pi.1974.
4. Metaverse (Ultra-High Definition Display) | Products & Technologies Available online: https://www.j-display.com/en/product_tech/metaverse.html (accessed on 26 February 2025).
5. Matsueda, Y. Required Characteristics of TFTs for Next Generation Flat Panel Display Backplanes; 2010;
6. The Semiconductor Decade: A Trillion-Dollar Industry | McKinsey Available online: https://www.mckinsey.com/industries/semiconductors/our-insights/the-semiconductor-decade-a-trillion-dollar-industry#/ (accessed on 26 February 2025).
7. Shockley, W. The Theory of P-n Junctions in Semiconductors and p-n Junction Transistors. Bell System Technical Journal 1949, 28, 435–489, doi:10.1002/j.1538-7305.1949.tb03645.x.
8. Bardeen, J.; Brattain, W.H. The Transistor, A Semi-Conductor Triode. Phys. Rev. 1948, 74, 230–231, doi:10.1103/PhysRev.74.230.
9. Weimer, P.K. The TFT A New Thin-Film Transistor. Proceedings of the IRE 1962, 50, 1462–1469, doi:10.1109/JRPROC.1962.288190.
10. Klasens, H.A.; Koelmans Reference, H.; Weimer, P.K. Solid-State Electronics Pergamon Press. Radio Engrs 1964, 50, 702–704.
11. Le Comber, P.G.; Spear, W.E. Electronic Properties of Doped Amorphous Si and Ge. AIP Conference Proceedings 1976, 31, 284–295, doi:10.1063/1.30769.
12. Zhao, Y.; Zhang, X.; Yan, B. Hydrogenated Amorphous Silicon Thin Film. In Handbook of Photovoltaic Silicon; Yang, D., Ed.; Springer: Berlin, Heidelberg, 2019; pp. 639–692 ISBN 978-3-662-56472-1.
13. Zhang, S.; Zhu, C.; Sin, J.K.O.; Mok, P.K.T. A Novel Ultrathin Elevated Channel Low-Temperature Poly-Si TFT. IEEE Electron Device Letters 1999, 20, 569–571, doi:10.1109/55.798046.
14. Hosono, H.; Yasukawa, M.; Kawazoe, H. Novel Oxide Amorphous

Semiconductors: Transparent Conducting Amorphous Oxides. Journal of Non-Crystalline Solids 1996, 203, 334–344, doi:10.1016/0022-3093(96)00367-5.

15. Nomura, K.; Ohta, H.; Takagi, A.; Kamiya, T.; Hirano, M.; Hosono, H. Room-Temperature Fabrication of Transparent Flexible Thin-Film Transistors Using Amorphous Oxide Semiconductors. Nature 2004, 432, 488–492, doi:10.1038/nature03090.
16. Nomura, K.; Kamiya, T.; Hosono, H. Highly Stable Amorphous In-Ga-Zn-O Thin-Film Transistors Produced by Eliminating Deep Subgap Defects. Applied Physics Letters 2011, 99, 053505, doi:10.1063/1.3622121.
17. Myny, K.; Steudel, S.; Smout, S.; Vicca, P.; Furthner, F.; van der Putten, B.; Tripathi, A.K.; Gelinck, G.H.; Genoe, J.; Dehaene, W.; et al. Organic RFID Transponder Chip with Data Rate Compatible with Electronic Product Coding. Organic Electronics 2010, 11, 1176–1179, doi:10.1016/j.orgel.2010.04.013.
18. Magari, Y.; Kataoka, T.; Yeh, W.; Furuta, M. High-Mobility Hydrogenated Polycrystalline In2O3 (In2O3:H) Thin-Film Transistors. Nat. Commun. 2022, 13, 1078, doi:10.1038/s41467-022-28480-9.
19. Yap, B.K.; Zhang, Z.; Thien, G.S.H.; Chan, K.-Y.; Tan, C.Y. Recent Advances of In2O3-Based Thin-Film Transistors: A Review. Applied Surface Science Advances 2023, 16, 100423, doi:10.1016/j.apsadv.2023.100423.
20. Hsieh, H.; Lu, H.; Ting, H.; Chuang, C.; Chen, C.; Lin, Y. Development of IGZO TFTs and Their Applications to Next-generation Flat-panel Displays. J. Inf. Disp. 2010, 11, 160–164, doi:10.1080/15980316.2010.9665845.
21. Arai, T. Oxide-TFT Technologies for next-Generation AMOLED Displays. J. Soc. Inf. Disp. 2012, 20, 156–161, doi:10.1889/JSID20.3.156.
22. Park, S.H.K.; Hwang, C.S.; Lee, J.I.; Chung, S.M.; Yang, Y.S.; Do, L.M.; Chu, H.Y. 4.3: Transparent ZnO Thin Film Transistor Array for the Application of Transparent AM-OLED Display. In Proceedings of the SID Symp. Dig. Tech. Pap.; 2006; Vol. 37, pp. 25–28.
23. Mahajan, S.; Jagtap, S. Metal-Oxide Semiconductors for Carbon Monoxide (CO) Gas Sensing: A Review. Appl. Mater. Today 2020, 18, 100483, doi:10.1016/j.apmt.2019.100483.
24. Gurlo, A.; Ivanovskaya, M.; Bârsan, N.; Schweizer-Berberich, M.; Weimar, U.; Göpel, W.; Diéguez, A. Grain Size Control in Nanocrystalline In2O3 Semiconductor Gas Sensors. Sens. Actuators B Chem. 1997, 44, 327–333,

doi:10.1016/S0925-4005(97)00199-8.

25. Rim, Y.S. Review of Metal Oxide Semiconductors-Based Thin-Film Transistors for Point-of-Care Sensor Applications. J. Inf. Disp. 2020, 21, 203–210, doi:10.1080/15980316.2020.1714762.
26. Kimura, M. Emerging Applications Using Metal-Oxide Semiconductor Thin-Film Devices. Jpn. J. Appl. Phys. 2019, 58, 090503, doi:10.7567/1347-4065/ab1868.
27. Ding, S.J.; Wu, X. Superior Atomic Layer Deposition Technology for Amorphous Oxide Semiconductor Thin-Film Transistor Memory Devices. Chem. Mater. 2020, 32, 1343–1357, doi:10.1021/acs.chemmater.9b03237.
28. Shi, J.; Zhang, J.; Yang, L.; Qu, M.; Qi, D.-C.; Zhang, K.H.L. Wide Bandgap Oxide Semiconductors: From Materials Physics to Optoelectronic Devices. Advanced Materials 2021, 33, 2006230, doi:10.1002/adma.202006230.
29. Hosono, H. Ionic Amorphous Oxide Semiconductors: Material Design, Carrier Transport, and Device Application. Journal of Non-Crystalline Solids 2006, 352, 851–858, doi:10.1016/j.jnoncrysol.2006.01.073.
30. Troughton, J.; Atkinson, D. Amorphous InGaZnO and Metal Oxide Semiconductor Devices: An Overview and Current Status. J. Mater. Chem. C 2019, 7, 12388–12414, doi:10.1039/C9TC03933C.
31. Li, S.S.; Thurber, W.R. The Dopant Density and Temperature Dependence of Electron Mobility and Resistivity in n-Type Silicon. Solid-State Electronics 1977, 20, 609–616, doi:10.1016/0038-1101(77)90100-9.
32. Kamiya, T.; Hosono, H. Material Characteristics and Applications of Transparent Amorphous Oxide Semiconductors. NPG Asia Mater. 2010, 2, 15–22, doi:10.1038/asiamat.2010.5.
33. Ma, J.; Sinha, S. Thermoelectric Properties of Highly Doped N-Type Polysilicon Inverse Opals. Journal of Applied Physics 2012, 112, 073719, doi:10.1063/1.4758382.
34. Kamiya, T.; Nomura, K.; Hosono, H. Present Status of Amorphous In–Ga–Zn–O Thin-Film Transistors. Technol. Adv. Mater 2010, 11, 044305, doi:10.1088/1468-6996/11/4/044305.
35. Kim, T.; Kim, M.J.; Lee, H.; Xu, H.; Choi, C.H.; Kim, J.-K.; Jeong, J.K. Origin of Ambipolar Behavior in P-Type Tin Monoxide Semiconductors: Impact of Oxygen Vacancy Defects. IEEE Transactions on Electron Devices 2021, 68, 4467–4472, doi:10.1109/TED.2021.3099081.

36. Xu, W.; Hu, L.; Zhao, C.; Zhang, L.; Zhu, D.; Cao, P.; Liu, W.; Han, S.; Liu, X.; Jia, F.; et al. Low Temperature Solution-Processed IGZO Thin-Film Transistors. Appl. Surf. Sci. 2018, 455, 554–560, doi:10.1016/j.apsusc.2018.06.005.

37. Kim, G.H.; Du Ahn, B.; Shin, H.S.; Jeong, W.H.; Kim, H.J.; Kim, H.J. Effect of Indium Composition Ratio on Solution-Processed Nanocrystalline InGaZnO Thin Film Transistors. Appl. Phys. Lett. 2009, 94, 233501, doi:10.1063/1.3151827.

38. Furuta, M.; Koretomo, D.; Magari, Y.; Aman, S.G.M.; Higashi, R.; Hamada, S. Heterojunction Channel Engineering to Enhance Performance and Reliability of Amorphous In–Ga–Zn–O Thin-Film Transistors. Jpn. J. Appl. Phys. 2019, 58, 090604, doi:10.7567/1347-4065/ab1f9f.

39. Sheng, J.; Hong, T.; Lee, H.-M.; Kim, K.; Sasase, M.; Kim, J.; Hosono, H.; Park, J.-S. Amorphous IGZO TFT with High Mobility of ~70 Cm2/(V s) via Vertical Dimension Control Using PEALD. ACS Appl. Mater. Interfaces 2019, 11, 40300–40309, doi:10.1021/acsami.9b14310.

40. Mativenga, M.; Um, J.G.; Jang, J. Reduction of Bias and Light Instability of Mixed Oxide Thin-Film Transistors. Applied Sciences 2017, 7, 885, doi:10.3390/app7090885.

41. Chowdhury, M.D.H.; Ryu, S.H.; Migliorato, P.; Jang, J. Effect of Annealing Time on Bias Stress and Light-Induced Instabilities in Amorphous Indium–Gallium–Zinc-Oxide Thin-Film Transistors. Journal of Applied Physics 2011, 110, 114503, doi:10.1063/1.3662869.

42. Effect of High-Pressure Oxygen Annealing on Negative Bias Illumination Stress-Induced Instability of InGaZnO Thin Film Transistors | Applied Physics Letters | AIP Publishing Available online: https://pubs.aip.org/aip/apl/article/98/10/103509/122083 (accessed on 23 November 2024).

43. Ahn, B.D.; Kim, H.-S.; Yun, D.-J.; Park, J.-S.; Kim, H.J. Improvement of Negative Bias Temperature Illumination Stability of Amorphous IGZO Thin-Film Transistors by Water Vapor-Assisted High-Pressure Oxygen Annealing. ECS J. Solid State Sci. Technol. 2014, 3, Q95, doi:10.1149/2.019405jss.

44. Oh, C.; Jang, H.; Kim, H.W.; Jung, H.; Park, H.; Cho, J.; Kim, B.S. Influence of Oxygen Partial Pressure in In-Sn-Ga-O Thin-Film Transistors at a Low Temperature. J. Alloys Compd. 2019, 805, 211–217, doi:10.1016/j.jallcom.2019.07.091.

45. Noh, H.Y.; Kim, J.; Kim, J.-S.; Lee, M.-J.; Lee, H.-J. Role of Hydrogen in Active Layer of Oxide-Semiconductor-Based Thin Film Transistors. Crystals 2019, 9, 75, doi:10.3390/cryst9020075.

46. Yang, B.; Li, P.; Chen, Z.; Xu, H.; Fu, C.; Ding, X.; Zhang, J. Effect of Titanium Cation Doping on the Performance of In2O3 Thin Film Transistors Grown via Atomic Layer Deposition. Coatings 2023, 13, 605, doi:10.3390/coatings13030605.

47. Furuta, M.; Shimpo, K.; Kataoka, T.; Tanaka, D.; Matsumura, T.; Magari, Y.; Velichko, R.; Sasaki, D.; Kawashima, E.; Tsuruma, Y. 7-4: High Mobility Hydrogenated Polycrystalline In-Ga-O (IGO:H) Thin-Film Transistors Formed by Solid Phase Crystallization. In Proceedings of the Symp. Dig. Tech. Papers; 2021; Vol. 52(1), pp. 69–72.

48. Billah, M.M.; Siddik, A.B.; Kim, J.B.; Yim, D.K.; Choi, S.Y.; Liu, J.; Severin, D.; Hanika, M.; Bender, M.; Jang, J. High-Performance Coplanar Dual-Channel a-InGaZnO/a-InZnO Semiconductor Thin-Film Transistors with High Field-Effect Mobility. Adv. Electron. Mater. 2021, 7, 2000896, doi:10.1002/aelm.202000896.

49. Koretomo, D.; Hashimoto, Y.; Hamada, S.; Miyanaga, M.; Furuta, M. Influence of a SiO_2 Passivation on Electrical Properties and Reliability of In–W–Zn–O Thin-Film Transistor. Jpn. J. Appl. Phys. 2018, 58, 018003, doi:10.7567/1347-4065/aae895.

50. Parthiban S.; Kwon J.Y. Role of dopants as a carrier suppressor and strong oxygen binder in amorphous indium-oxide-based field effect transistor. J. Mater. Res. 2014, 29, 1585–1596, doi:10.1557/jmr.2014.187.

51. Fortunato, E.; Barquinha, P.; Martins, R. Oxide Semiconductor Thin-Film Transistors: A Review of Recent Advances. Adv. Mater. 2012, 24, 2945–2986, doi:10.1002/adma.201103228.

52. Kono, S.; Magari, Y.; Mori, M.; Aman, S.G.M.; Fruehauf, N.; Furuta, H.; Furuta, M. Hydrogenated In–Ga–Zn–O Thin-Film Transistors with Anodized and Fluorinated Al2O3 Gate Insulator for Flexible Devices. Jpn. J. Appl. Phys. 2021, 60, SBBM05, doi:10.35848/1347-4065/abdf74.

53. Zhang, J.; Wen, X.; Hu, L.; Xu, W.; Zhu, D.; Cao, P.; Liu, W.; Han, S.; Liu, X.; Jia, F.; et al. C-Axis Oriented Crystalline IGZO Thin-Film Transistors by Magnetron Sputtering. J. Mater. Chem. C 2017, 5, 2388–2396, doi:10.1039/C7TC00193B.

54. Ebata, K.; Tomai, S.; Tsuruma, Y.; Iitsuka, T.; Matsuzaki, S.; Yano, K. High-Mobility Thin-Film Transistors with Polycrystalline In–Ga–O Channel Fabricated

by DC Magnetron Sputtering. Appl. Phys. Express 2012, 5, 011102, doi:10.1143/APEX.5.011102.

55. Weiher, R.L. Electrical Properties of Single Crystals of Indium Oxide. J. Appl. Phys. 2004, 33, 2834–2839, doi:10.1063/1.1702560.

56. Moschou, D.C.; Theodorou, C.G.; Hastas, N.A.; Tsormpatzoglou, A.; Kouvatsos, D.N.; Voutsas, A.T.; Dimitriadis, C.A. Short Channel Effects on LTPS TFT Degradation. Journal of Display Technology 2013, 9, 747–754, doi:10.1109/JDT.2012.2231049.

57. Matsuo, T.; Muramatsu, T. 21.1: Invited Paper: CG Silicon Technology and Development of System on Panel. SID Symposium Digest of Technical Papers 2004, 35, 856–859, doi:10.1889/1.1821405.

58. Shim, G.W.; Hong, W.; Cha, J.-H.; Park, J.H.; Lee, K.J.; Choi, S.-Y. TFT Channel Materials for Display Applications: From Amorphous Silicon to Transition Metal Dichalcogenides. Advanced Materials 2020, 32, 1907166, doi:10.1002/adma.201907166.

59. Mitani, M.; Endo, T.; Tsuboi, S.; Okada, T.; Kawachi, G.; Matsumura, M. Relationship between Thin-Film Transistor Characteristics and Crystallographic Orientation in Excimer-Laser-Processed Pseudo-Single-Crystal-Silicon Films. Jpn. J. Appl. Phys. 2010, 49, 124001, doi:10.1143/JJAP.49.124001.

60. Nakazaki, Y.; Kawachi, G.; Jyumonji, M.; Ogawa, H.; Hiramatu, M.; Azuma, K.; Warabisako, T.; Matsumura, M. Characterization of Novel Polycrystalline Silicon Thin-Film Transistors with Long and Narrow Grains. Jpn. J. Appl. Phys. 2006, 45, 1489, doi:10.1143/JJAP.45.1489.

61. Sameshima, T.; Usui, S.; Sekiya, M. XeCl Excimer Laser Annealing Used in the Fabrication of Poly-Si TFT's. IEEE Electron Device Letters 1986, 7, 276–278, doi:10.1109/EDL.1986.26372.

62. Pimentel, A.; Gonçalves, A.; Marques, A.; Martins, R.; Fortunato, E. Role of the Thickness on the Electrical and Optical Performances of Undoped Polycrystalline Zinc Oxide Films Used as UV Detectors. Journal of Non-Crystalline Solids 2006, 352, 1448–1452, doi:10.1016/j.jnoncrysol.2006.02.022.

63. Greuter, F.; Blatter, G. Electrical Properties of Grain Boundaries in Polycrystalline Compound Semiconductors. Semicond. Sci. Technol. 1990, 5, 111, doi:10.1088/0268-1242/5/2/001.

64. Fritzsche, H. Development in Understanding and Controlling the Staebler-Wronski

Effect in a-Si:H. Annual Review of Materials Research 2001, 31, 47–79, doi:10.1146/annurev.matsci.31.1.47.

65. Street, R. Technology and Applications of Amorphous Silicon; Springer Science & Business Media, 1999; ISBN 978-3-540-65714-9.

66. Yoo, J.S.; Jung, S.H.; Kim, Y.C.; Byun, S.C.; Kim, J.M.; Choi, N.B.; Yoon, S.Y.; Kim, C.D.; Hwang, Y.K.; Chung, I.J. Highly Flexible AM-OLED Display With Integrated Gate Driver Using Amorphous Silicon TFT on Ultrathin Metal Foil. J. Disp. Technol. 2010, 6, 565–570, doi:10.1109/JDT.2010.2048998.

67. Mandracci, P. Crystalline and Non-Crystalline Solids; BoD – Books on Demand, 2016; ISBN 978-953-51-2445-0.

68. Ge, C.; Liu, Z.; Zhu, Y.; Zhou, Y.; Jiang, B.; Zhu, J.; Yang, X.; Zhu, Y.; Yan, S.; Hu, H.; et al. Insight into the High Mobility and Stability of In2O3:H Film. Small 2024, 20, 2304721, doi:10.1002/smll.202304721.

Chapter 2

Fabrication techniques and characterization techniques

2.1 Fabrication techniques

In terms of fabrication techniques, Indium oxide films were deposited by magnetron sputtering (Shinko, SRL3320). Post-deposition annealing was performed by rapid thermal annealing (RTA).

2.1.1 Magnetron sputtering

Physical vapor deposition (PVD) is a coating method in which thin films are deposited by the condensation of a vaporized form of the film material on the substrate. The PVD method has been used for film deposition for decades, including thermal evaporation and sputtering. Since the primary source of the deposited film is typically a solid target, the PVD method has few limitations in deposition materials, such as metal, semiconductor, insulator, and polymer.

Magnetron sputtering, one of the PVD methods, is cathodic sputtering of target material in magnetron discharge plasma.[1] It overcomes the disadvantages of diode sputtering, such as low deposition rate, uniformity, and film quality, making it an effective method for the deposition of a wide range of thin film materials[2–5]. In a sputtering process, argon was first ionized to electrons and cations (Ar^+) in the vacuum chamber, resulting in the formation of glow discharge. Plasma (almost from Ar^+) was confined in front of the target, which was achieved by the combination of electric and magnetic fields. Then, energetic ions generated in a glow discharge plasma bombard the target, causing the sputtering of target atoms. These sputtered atoms then condense on a substrate, forming a thin film.[3] Figure 2. 1 shows the schematic of the sputtering process.

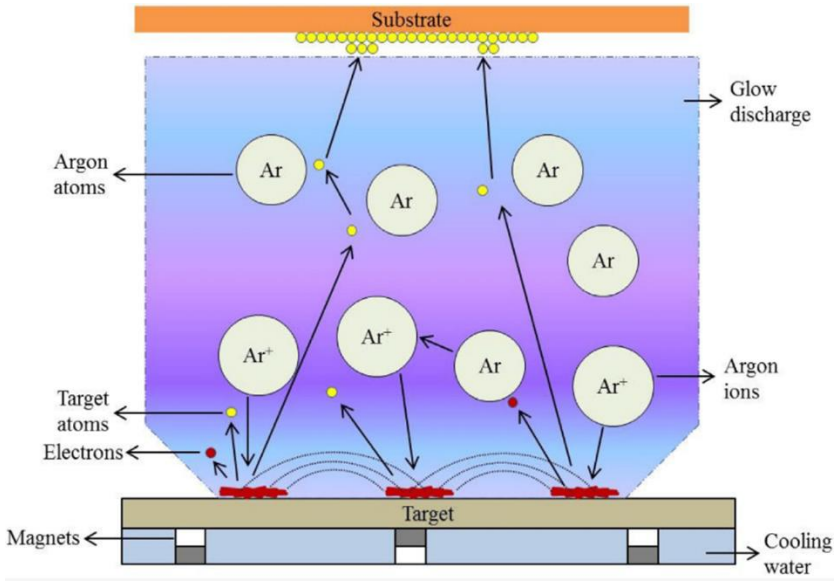

Figure 2. 1 Schematic diagram illustrating the basic components of a magnetron sputtering system.[6]

2.1.2 Rapid thermal annealing

Thermal treatment is a crucial process used to improve the electrical properties and physical structure of materials. In the semiconductor fabrication process, Annealing is usually used to passivate lattice defects, activate dopants, and improve the properties and uniformity of thin films.[7–9] The annealing methods include furnace annealing, rapid thermal annealing (RTA), lasering annealing, and flash lamp annealing. Among annealing methods, RTA achieves thermal treatment in a short time, showing significant advantages in precise adjustment of film properties and accelerating fabrication processes.[10] In this study, RTA was performed to anneal oxide semiconductors.

2.2 Characterization techniques

2.2.1 X-ray diffraction (XRD)

X-ray diffraction is one of the most essential non-destructive measurement methods to

analyze the structure information of solid materials, including ceramics, metals, intermetallics, minerals, inorganic compounds, and so on.[11] Bragg's Law (equation 2.1) is one of the keystones in understanding X-ray diffraction. In this equation, n is an integer number, λ is X-ray wavelength, d is lattice constancy, and θ is the incident angle. Figure 2. 2 shows the working principle of XRD measurement. When an X-ray beam strikes a crystalline sample, constructive interference occurs when the path difference of the scattered beams is an integer multiple of the X-ray wavelength, resulting in a pronounced reflection. Conversely, destructive interference results in the partial or entire cancellation of the reflected beams when the path difference is not an integer multiple of the wavelength. Measuring the intensity of diffracted beams at different angles obtains a characteristic diffraction pattern that reveals essential structural information about the material, including lattice parameters, crystallographic phase, and crystallite size.

$$n\lambda = 2d\sin\theta \qquad (2.1).$$

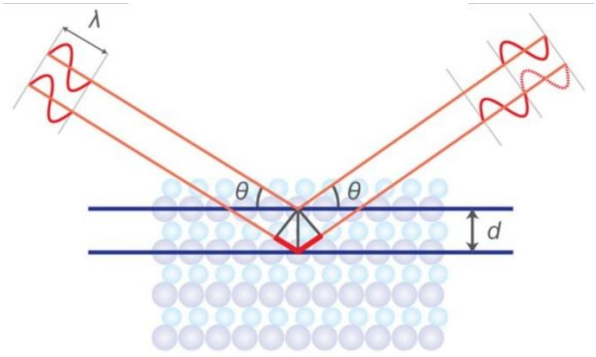

Figure 2. 2 Schematic of XRD measurement.[12]

2.2.2 Scanning Electron Microscopy (SEM)

Figure 2. 3 shows the comparison of the typical spatial resolution of key materials

characterization imaging methods. Compared to light microscopy, high accelerating voltages lead to a resolution ranging from 1 ~ 10 nm, resulting in a potential step change in image spatial resolution. Thus, SEM is one of the most versatile instruments available for the evaluation and analysis of microstructure morphology and chemical composition characterizations.[13]

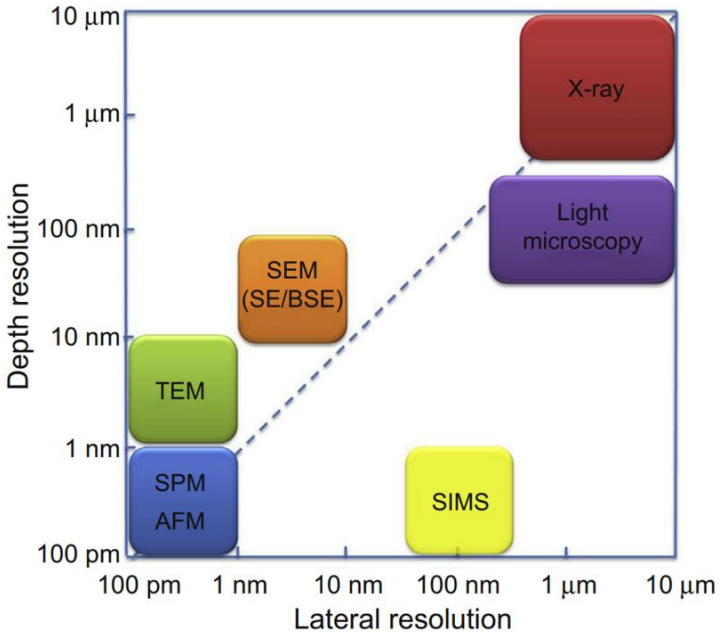

Figure 2. 3 Comparison of the typical spatial resolution of key materials characterization imaging methods SPM, AFM, TEM, SEM, SIMS, X-ray imaging, and light microscopy.[14]

Figure 2. 4 shows a schematic of a scanning electron microscope, including an electron gun (electron source and accelerating anode), electromagnetic lenses to focus the electrons, a vacuum chamber housing the specimen stage, and a selection of detectors to collect the signals emitted from the specimen.[14,15] Electrons are produced at the top of the column in the electron gun and accelerated through the column at an accelerating voltage. Lenses focus the electron beam on the sample surface. The position of the

electron beam on the sample is controlled by scan coils situated above the objective lens. The sample is struck by a scanned electron beam, generating various signals, including secondary electrons, backscattered electrons, and characteristic X-rays, which provide information on the sample's topography and composition. These signals are then detected by appropriate detectors. The intensity of electrons captured from each point on the sample surface is then converted into an image.

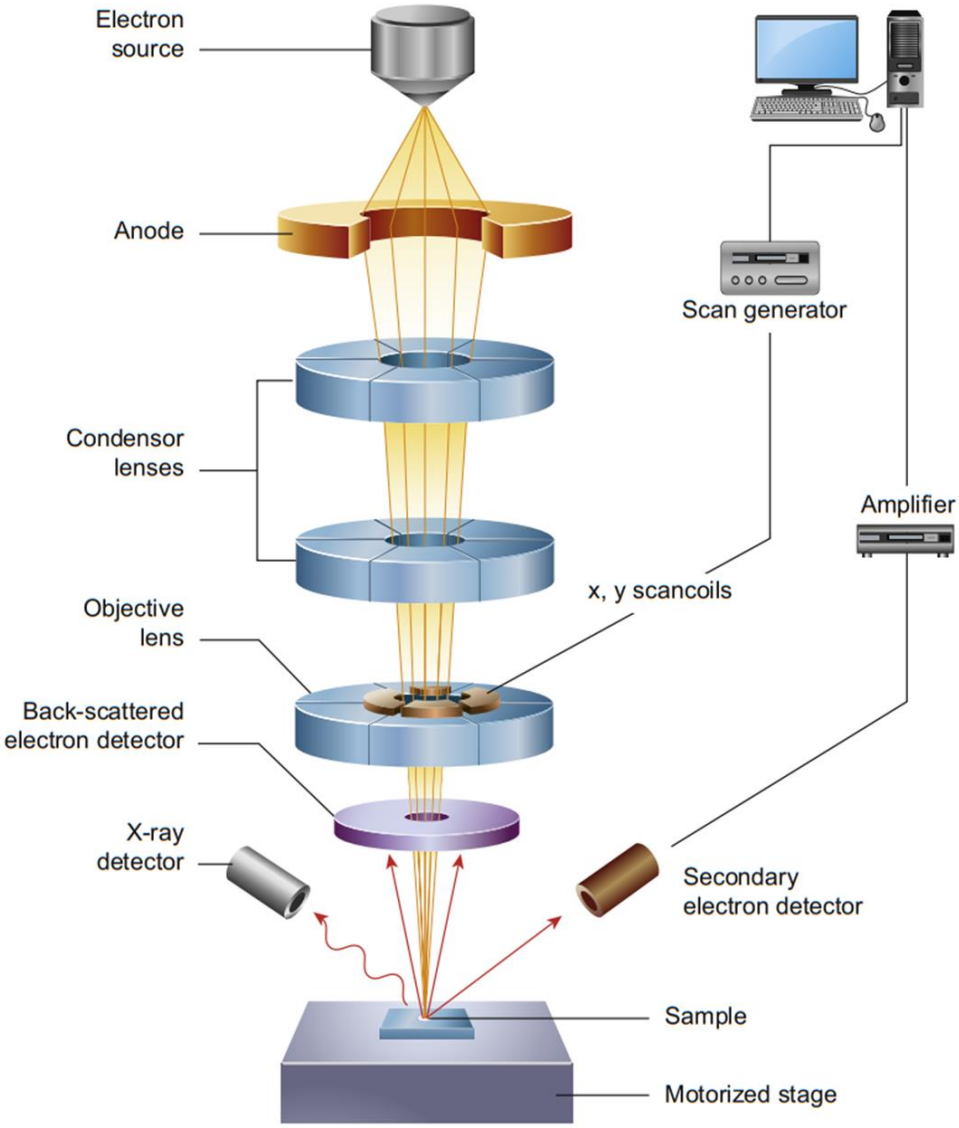

Figure 2. 4 Schematic of a scanning electron microscope.[14]

2.2.3 Thermal Desorption Spectroscopy (TDS)

Thermal Desorption Spectroscopy (TDS) is an analysis technique widely used to investigate gas desorption processes.[16] Figure 2. 5 shows a schematic of the TDS system. The TDS system is divided into three portions for (i) pre-evacuating and transporting system, (ii) heating system in the main chamber, and (iii) detecting system by QMS (quadrupole mass spectrometer). TC: thermo couple, TMP: turbo-molecular pump, RP: rotary pump, VG: vacuum gague, PS: pressure switch.

In TDS measurement, the sample is gradually heated in a base pressure below 5×10^{-7} Pa, enabling it to acquire sufficient thermal energy for desorption. The desorbed molecules, including hydrogen, H_2O, O_2, and In, are then detected using a QMS, providing data about the desorbed species, the temperatures at which desorption occurs, and the desorption rate. Analyzing this data enables inferences on the chemical composition of the material, adsorption energies, and the kinetics of surface reactions. TDS is extensively utilized in semiconductors, surface chemistry, catalyst characterization, and investigations of material surface changes.[16–18]

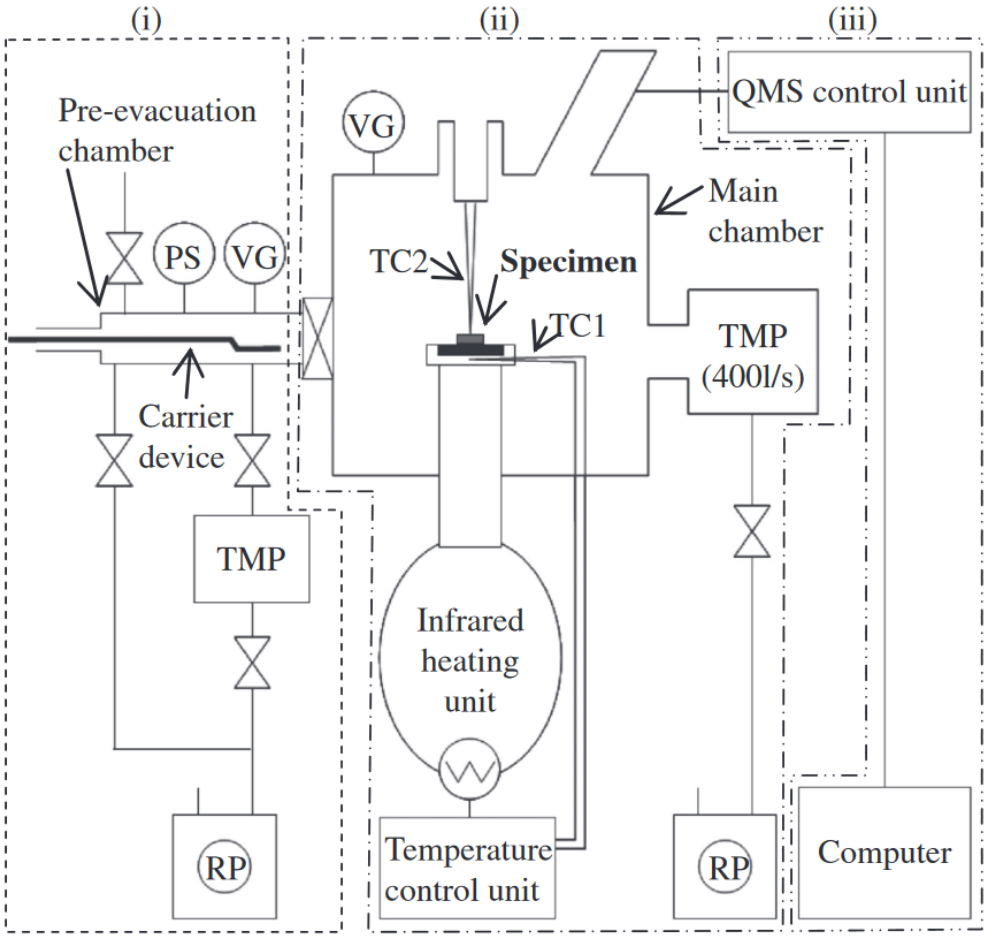

Figure 2. 5 A schematic of the thermal desorption spectroscopic system.[18]

2.2.4 Hard X-ray photoelectron spectroscopy (HAXPES)

Since the pioneering works of Kai Siegbahn and his co-workers, X-ray photoelectron spectroscopy (XPS) has grown to be a popular analytical technique in materials science as it can assess the surface chemistry of a broad range of samples.[19–21] XPS is based on the photoelectric effect, which can be described in equation 2.2. The kinetic energy of the ejected electrons is named E_k. The binding energy of an electron is represented by E_b. The energy of a photon is given by $h\nu$, where h is the Plank's constant and ν is the frequency of a photon. The work function is represented by the symbol ϕ, which is the minimum energy needed to remove an electron from a solid.

$$E_k = h\nu - E_b - \phi \quad (2.2)$$

When X-rays hit a material, the photons have a certain energy and the electrons from the atoms in the sample are then ejected from the atom as photoelectrons. The electrons ejected are analyzed in the XPS detector by measuring the kinetic energy of electrons, which provides the information to determine the kind of elements present in the sample.[22–24]

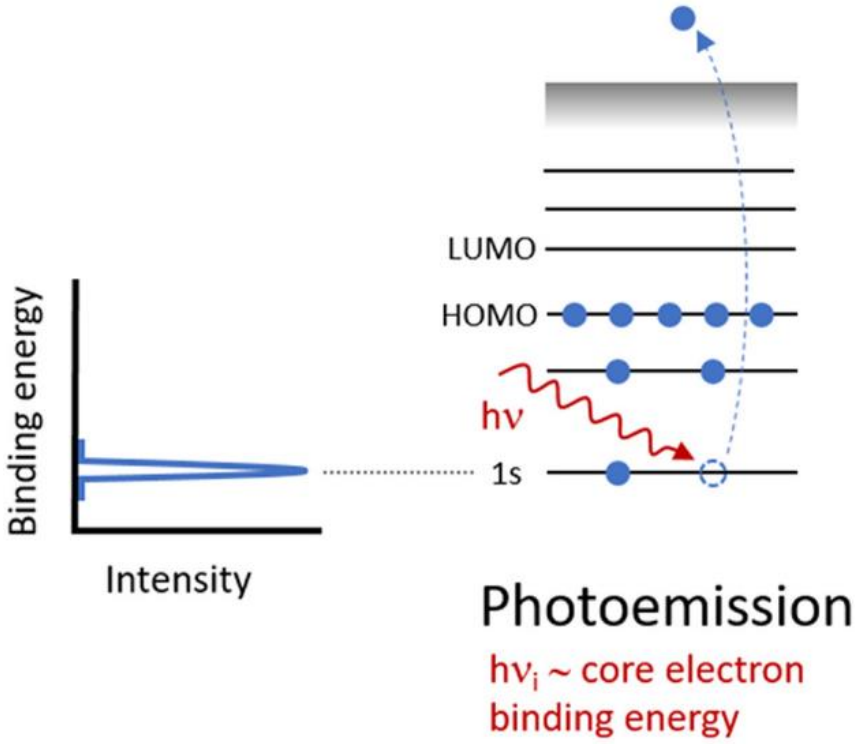

Figure 2. 6 Schematic representation of the energy level diagrams with the associated transitions and the corresponding peaks in XPS spectra.[25]

XPS and Hard X-ray Photoelectron Spectroscopy (HAXPES) are both surface analysis techniques based on the photoelectric effect, with the primary difference being the energy of the X-rays. XPS generally uses low-energy X-ray sources, typically Al-Kα (1486.7 eV) or Mg-Kα (1253.6 eV), which restrict the penetration depth to a few nanometers of the

sample surface. On the other hand, HAXPES uses higher-energy X-ray, typically greater than 2.5 keV. One of the most advantageous features of HAXPES compared to conventional photoemission spectroscopy is its potential for bulk sensitive measurements, as shown in Figure 2. 7.[20] Compared to conventional XPS, HAXPES, utilizing higher energy X-rays, increases the depth of investigation, which effectively avoids contamination or oxidation caused by air exposure, resulting in more accurate measurement results. [26]

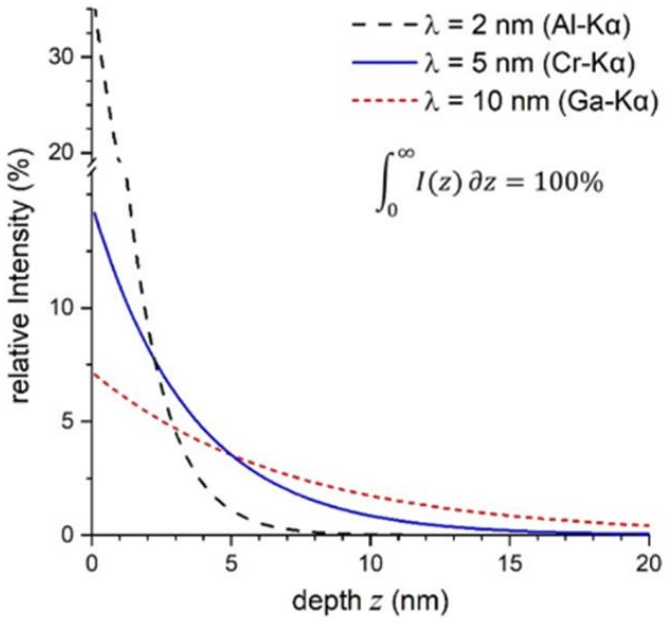

Figure 2. 7 Typical values of the inelastic mean free path of photoelectrons emitted using different X-ray sources.[27]

2.2.5 Hall measurement

Electrical properties of oxide semiconductor films are evaluated by Hall Effect Measurement system using van der Pauw geometry. The van der Pauw Method is a widely used technique for measuring the electrical properties of materials in thin film form. This

method operates in a four-probe mode and can be used in any arbitrary shape with a flat shape of uniform thickness, no isolated holes, and the four contacts must be located at the edges of the sample, as shown in Figure 2. 8.[28–31]

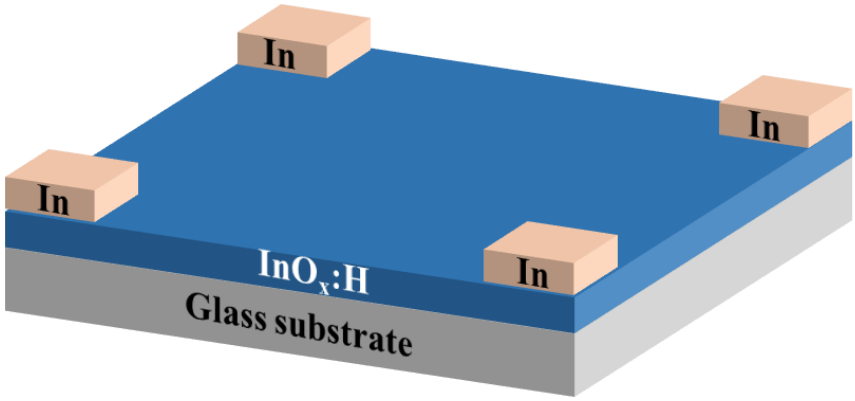

Figure 2. 8 Sample preparation for Hall measurements.

References

1. Alexeeva, O.K.; Fateev, V.N. Application of the Magnetron Sputtering for Nanostructured Electrocatalysts Synthesis. *International Journal of Hydrogen Energy* **2016**, *41*, 3373–3386, doi:10.1016/j.ijhydene.2015.12.147.
2. Gudmundsson, J.T. Physics and Technology of Magnetron Sputtering Discharges. *Plasma Sources Sci. Technol.* **2020**, *29*, 113001, doi:10.1088/1361-6595/abb7bd.
3. Kelly, P.J.; Arnell, R.D. Magnetron Sputtering: A Review of Recent Developments and Applications. *Vacuum* **2000**, *56*, 159–172, doi:10.1016/S0042-207X(99)00189-X.
4. Ellmer, K. Magnetron Sputtering of Transparent Conductive Zinc Oxide: Relation between the Sputtering Parameters and the Electronic Properties. *J. Phys. D: Appl. Phys.* **2000**, *33*, R17, doi:10.1088/0022-3727/33/4/201.
5. Han, J.G. Recent Progress in Thin Film Processing by Magnetron Sputtering with Plasma Diagnostics. *J. Phys. D: Appl. Phys.* **2009**, *42*, 043001, doi:10.1088/0022-3727/42/4/043001.
6. Maurya, D.K.; Sardarinejad, A.; Alameh, K. Recent Developments in R.F. Magnetron Sputtered Thin Films for pH Sensing Applications—An Overview. *Coatings* **2014**, *4*, 756–771, doi:10.3390/coatings4040756.
7. Rebohle, L.; Prucnal, S.; Berencén, Y.; Begeza, V.; Zhou, S. A Snapshot Review on Flash Lamp Annealing of Semiconductor Materials. *MRS Advances* **2022**, *7*, 1301–1309, doi:10.1557/s43580-022-00425-w.
8. Nomura, K.; Kamiya, T.; Ohta, H.; Hirano, M.; Hosono, H. Defect Passivation and Homogenization of Amorphous Oxide Thin-Film Transistor by Wet O_2 Annealing. *Applied Physics Letters* **2008**, *93*, 192107, doi:10.1063/1.3020714.
9. Misra, N.; Xu, L.; Rogers, M.S.; Ko, S.H.; Grigoropoulos, C.P. Pulsed Laser Annealing of Semiconductor Structures for Functional Devices. *physica status solidi c* **2008**, *5*, 3264–3270, doi:10.1002/pssc.200779506.
10. Fiory, A.T. Recent Developments in Rapid Thermal Processing. *J. Electron. Mater.* **2002**, *31*, 981–987, doi:10.1007/s11664-002-0031-9.
11. Cullity, B.D.; Smoluchowski, R. Elements of X-Ray Diffraction. *Physics Today* **1957**, *10*, 50, doi:10.1063/1.3060306.
12. X-Ray Diffraction (XRD) Available online: https://rigaku.com/resources/techniques/x-ray-diffraction-xrd (accessed on 27

February 2025).

13. Zhou, W.; Apkarian, R.; Wang, Z.L.; Joy, D. Fundamentals of Scanning Electron Microscopy (SEM). In *Scanning Microscopy for Nanotechnology: Techniques and Applications*; Zhou, W., Wang, Z.L., Eds.; Springer: New York, NY, 2007; pp. 1–40 ISBN 978-0-387-39620-0.
14. Inkson, B.J. 2 - Scanning Electron Microscopy (SEM) and Transmission Electron Microscopy (TEM) for Materials Characterization. In *Materials Characterization Using Nondestructive Evaluation (NDE) Methods*; Hübschen, G., Altpeter, I., Tschuncky, R., Herrmann, H.-G., Eds.; Woodhead Publishing, 2016; pp. 17–43 ISBN 978-0-08-100040-3.
15. Goldstein, J. *Practical Scanning Electron Microscopy: Electron and Ion Microprobe Analysis*; Springer Science & Business Media, 2012; ISBN 978-1-4613-4422-3.
16. Castro, F.J.; Sánchez, A.D.; Meyer, G. Bulk Effects in Thermal Desorption Spectroscopy. *The Journal of Chemical Physics* **1998**, *109*, 6940–6946, doi:10.1063/1.477261.
17. Kirchheim, R. Bulk Diffusion-Controlled Thermal Desorption Spectroscopy with Examples for Hydrogen in Iron. *Metall Mater Trans A* **2016**, *47*, 672–696, doi:10.1007/s11661-015-3236-2.
18. Izumi, T.; Itoh, G. Thermal Desorption Spectroscopy Study on the Hydrogen Trapping States in a Pure Aluminum. *Materials Transactions* **2011**, *52*, 130–134, doi:10.2320/matertrans.L-M2010825.
19. Siegbahn, K.; C, N.; A, F.; Nordberg, R.; arlsson, S.E.; Lindgren, I. Molecular and Solid State Structure Studied by Means of Electron Spectroscopy. *Almqvist and Wiksells AB,* **1967**, 108.
20. Kobayashi, K. Hard X-Ray Photoemission Spectroscopy. *Nuclear Instruments and Methods in Physics Research Section A: Accelerators, Spectrometers, Detectors and Associated Equipment* **2009**, *601*, 32–47, doi:10.1016/j.nima.2008.12.188.
21. Greczynski, G.; Haasch, R.T.; Hellgren, N.; Lewin, E.; Hultman, L. X-Ray Photoelectron Spectroscopy of Thin Films. *Nat Rev Methods Primers* **2023**, *3*, 1–19, doi:10.1038/s43586-023-00225-y.
22. Bagus, P.S.; Ilton, E.S.; Nelin, C.J. The Interpretation of XPS Spectra: Insights into Materials Properties. *Surface Science Reports* **2013**, *68*, 273–304, doi:10.1016/j.surfrep.2013.03.001.

23. Watts, J.F.; Wolstenholme, J. *An Introduction to Surface Analysis by XPS and AES*; John Wiley & Sons, 2019; ISBN 978-1-119-41758-3.

24. Corcoran, C.J.; Tavassol, H.; Rigsby, M.A.; Bagus, P.S.; Wieckowski, A. Application of XPS to Study Electrocatalysts for Fuel Cells. *Journal of Power Sources* **2010**, *195*, 7856–7879, doi:10.1016/j.jpowsour.2010.06.018.

25. Ketenoglu, D. A General Overview and Comparative Interpretation on Element-Specific X-Ray Spectroscopy Techniques: XPS, XAS, and XRS. *X-Ray Spectrometry* **2022**, *51*, 422–443, doi:10.1002/xrs.3299.

26. Pal, B.; Mukherjee, S.; Sarma, D.D. Probing Complex Heterostructures Using Hard X-Ray Photoelectron Spectroscopy (HAXPES). *Journal of Electron Spectroscopy and Related Phenomena* **2015**, *200*, 332–339, doi:10.1016/j.elspec.2015.06.005.

27. Siol, S.; Mann, J.; Newman, J.; Miyayama, T.; Watanabe, K.; Schmutz, P.; Cancellieri, C.; Jeurgens, L.P.H. Concepts for Chemical State Analysis at Constant Probing Depth by Lab-Based XPS/HAXPES Combining Soft and Hard X-Ray Sources. *Surface and Interface Analysis* **2020**, *52*, 802–810, doi:10.1002/sia.6790.

28. Gonzalez Hernandez, Y.L. Impact of Oxygen on the Conduction Mechanism through Hf0.5zr0.5o2 for ReRAM Memory Applications. phd, Doctorat en sciences de l'énergie et des matériaux: Québec, 2022.

29. Green, R.; Instruments, K. Hall Effect Measurements in Materials Characterization.

30. Agarwal, A.; Fiory, A.T.; Gossmann, H.-J.L.; Rafferty, C.S.; Frisella, P. Ultra-Shallow Junction Formation by Spike Annealing in a Lamp-Based or Hot-Walled Rapid Thermal Annealing System: Effect of Ramp-up Rate. *Materials Science in Semiconductor Processing* **1998**, *1*, 237–241, doi:10.1016/S1369-8001(98)00030-4.

31. Kinder, R.; Mikolášek, M.; Donoval, D.; Kováč, J.; Tlaczala, M. Measurement System with Hall and a Four Point Probes for Characterization of Semiconductors. *Journal of Electrical Engineering* **2013**, *64*, 106–111, doi:10.2478/jeec-2012-0015.

Chapter 3

Improvement of electrical properties of indium oxide films by hydrogen doping

3.1 Introduction

As technology advances at high speed, emerging applications and new device concepts continuously raise the standards for display technologies, requiring high characteristics of TFT. IGZO, a representative amorphous metal oxide semiconductor, has gained significant attention since Nomura et al. reported the use of IGZO as the channel layer in TFTs in 2004.[1] IGZO TFT shows a field effect mobility of 10 cm^2/Vs. However, further improvement in mobility is required to expand their applications. Thus, there have been active efforts to increase mobility, such as optimization of the composition of IGZO. Among oxide semiconductors, indium oxide is a candidate material for use as a channel layer due to its single-crystal Hall mobility of 160 cm^2/Vs.[2] Amorphous InO_x film exhibited low Hall mobility of ~40 cm^2/Vs. Hall mobility of polycrystalline InO_x film with different crystal qualities ranged from 50 cm^2/Vs to 70 cm^2/Vs, depending on the deposition and post-deposition treatment method.[3–5] Polycrystalline InO_x film with high Hall mobility requires extra complex processes and additional equipment, which increases fabrication costs.

In order to enhance the electrical properties of InO_x films by simple material and a simple process, elements such as H, Sn, Ti, Mo, and Ga were doped into films. The Hall mobility of these films is shown in Table 3. 1.

Table 3. 1 Summary of dopant elements in InO_x and their Hall mobility.

Dopant	Hall mobility (cm^2/Vs)	Reference
H	> 130	[5]
Sn	40	[6]
Ti	80	[7]
Zr	62-76	[8]
Mo	80-130	[9]
W	60-112	[10]
Ga	40	[11]

Amorphous metal oxide semiconductors, such as IGZO, ZnO, and indium oxide films, were fabricated at RT. Three categories of defects are identified: point defects, which create structural anomalies including metal–metal or oxygen–oxygen bonds; defects caused by modifications in material stoichiometry, including vacancies and interstitial atoms; and interfacial defects that inevitably occur in the active channel and at the interfaces between the channel and insulator layers.[12] Hydrogen was widely used as a dopant in oxide semiconductors, including binary and multinary semiconductors, to solve these issues. Because the dopant of hydrogen has been found to be an effective and straightforward method to passivate defects and increase electron mobility.[13–16] Nomura[17] reports that the carrier density of IGZO film was controlled, ranging from $10^{15} \sim 10^{20}$ cm^{-3}, by annealing in H_2. Rostislav Velichko[18] and S. G. Mehadi Aman[19] demonstrated that the introduction of hydrogen decreases activation temperature and defects, and enhances electrical properties of IGZO:H film. Hydrogen doping shows significant potential for enhancing the electrical properties of the semiconductor film.

Kataoka et al.[20] investigated InO_x and InO_x:H films in detail. It was found that InO_x film showed a polycrystalline phase before and after annealing. Whereas hydrogen-doped

InO_x film started to convert from amorphous to polycrystalline phase at a temperature above 175 °C, as shown in Figure 3. 1 and Figure 3. 2.

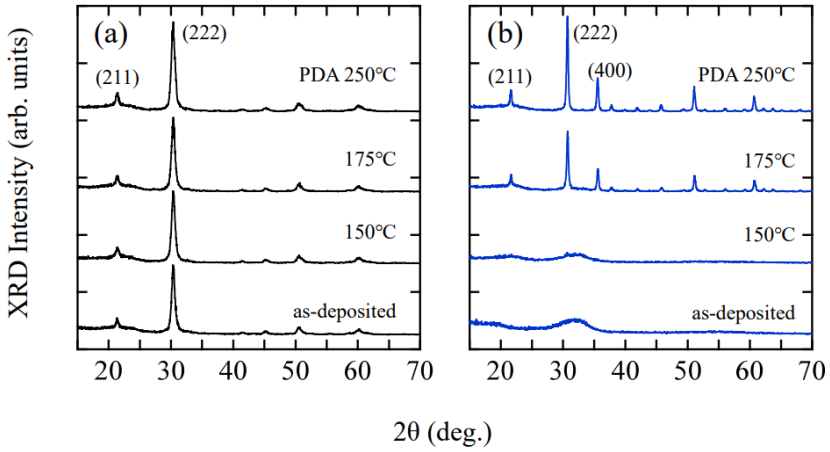

Figure 3. 1 Changes in XRD spectra of (a) InO_x and (b) InO_x:H (R[H_2] = 5%) films with PDA at different temperatures for 60 min.[20]

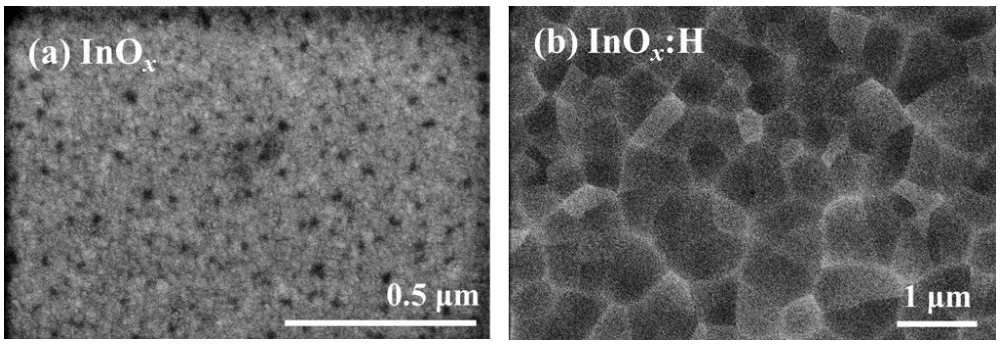

Figure 3. 2 SEM surface views of (a) poly-InO_x (R[H_2] = 0]) and (b) poly-InO_x:H (R[H_2] = 5%) films after PDA at 250 °C.[20]

Figure 3. 3 shows that InO_x film exhibited low Hall mobility of ~40 cm^2/Vs before and after annealing. In contrast, Hall mobility of InO_x:H films significantly increased from ~30 cm^2/Vs to 80 cm^2/Vs after annealing in N_2. The increase of Hall mobility corresponded with the occurrence of solid phase crystallization (SPC).[5,21–24]

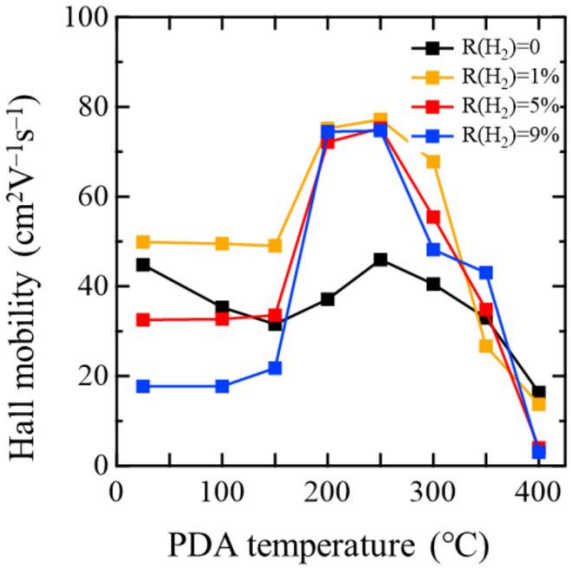

Figure 3. 3 Hall mobility of In_2O_3 and In_2O_3:H deposited at different R[H_2] values as a function of the annealing temperature in N_2.[20]

Even though hydrogen doping has been demonstrated to improve the electrical characteristics of InO_x and has been successfully used in the fabrication of TFTs. However, the effect of deposition conditions has not been investigated in detail. In this chapter, the effects of gas during the deposition of InO_x were investigated.

3.2 Experiment

50-nm-thick InO_x and InO_x:H films were deposited by RF magnetron sputtering (Shinko, SRL3320) at room temperature from a ceramic In_2O_3 target at room temperature on glass (EAGLE XG) or SiO_2 (100 nm)/Si substrates. Figure 3. 4 shows the schematic RF magnetron sputtering system. The O_2 gas flow ratio, which was defined as R[O_2] = O_2 / (Ar + O_2+ H_2), ranged from 2% to 4%, while the H_2 gas flow ratio, which was defined as R[H_2] = H_2 / (Ar + O_2 + H_2), ranged from 0% to 5% for InO_x and InO_x:H films. Equipment and process parameters are shown in Table 3. 2. The electrical properties of

the films were measured by Hall effect measurements using van der Pauw geometry (Toyo, ResiTest8400). The surface of the InO_x and InO_x:H films were analyzed by scanning electron microscope (SEM). The amounts of hydrogen and hydroxyl groups in the films were measured by thermal desorption spectroscopy (TDS). Chemical bonding states of the films were evaluated by hard X-ray photoelectron spectroscopy (HAXPES) system at the BL09XU of SPring-8.

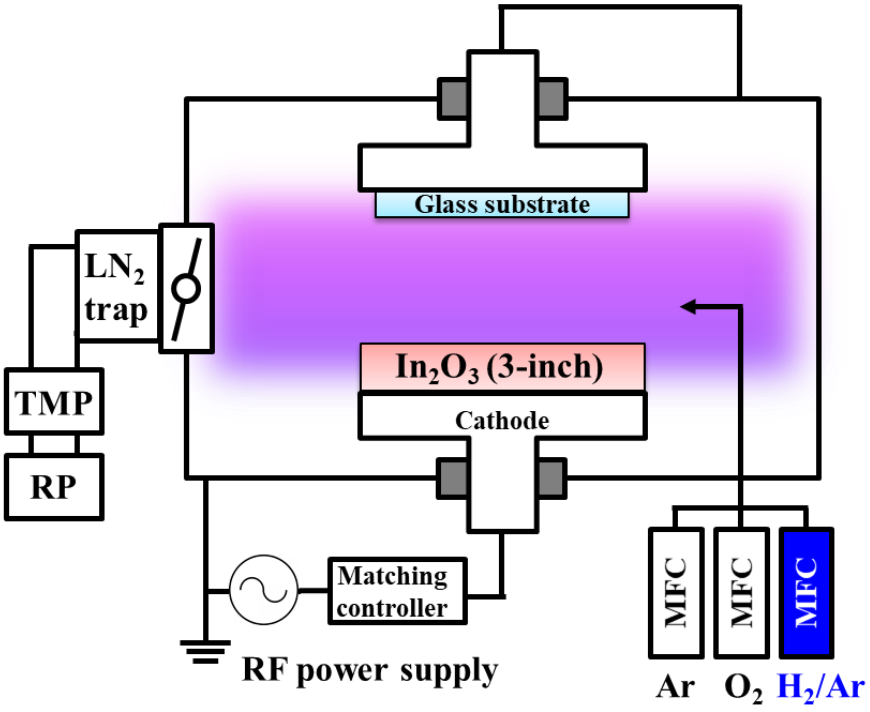

Figure 3. 4 RF magnetron sputtering system for InO_x film deposition in vacuum.

Table 3. 2 Deposition and annealing parameters of the InO_x and InO_x:H films.

Target	In_2O_3
Substrate	EAGLE XG Glass SiO_2 (100 nm)/Si substrates
Film thickness	50 nm
Deposition time	3′4″
Back pressure	$< 1\times10^{-4}$for InO_x $< 3\times10^{-4}$for InO_x:H
Deposition pressure	0.4 Pa
RF power	200 W
Total gas flow ($Ar+O_2+H_2$)	10 sccm
Deposition temperature (°C)	RT
$R[O_2] = O_2 / (Ar+O_2+H_2)$ (%)	2~4%
$R[H_2] = H_2 / (Ar+O_2+H_2)$ (%)	0~5%
Annealing temperature	150 ℃ ~ 400 ℃
Annealing time	0 ~ 60 min
Annealing Ramp rate	115 ℃/min

3.3 Development of electrical properties of InO_x film by H_2 doping

3.3.1 Effect of H_2 flow ratio on the electrical properties of InO_x and InO_x:H films

Electrical properties of the InO_x and InO_x:H films deposited at fixed $R[O_2]$ of 4% and at various $R[H_2]$ were analyzed. Figure 3. 5 shows Hall mobility and carrier density of InO_x and InO_x:H films with different hydrogen flow ratios as a function of annealing temperature in N_2 for 60 min. Hall mobility and carrier density of InO_x films ranged from 18 ~ 47 cm^2/Vs and 4.2×10^{19} ~ 2.2×10^{20} cm^{-3}, respectively, which did not change dramatically. Whereas with the increase in temperature, Hall mobility of InO_x:H films initially rises from ~20 cm^2/Vs for as-deposited film and reaches a peak value of ~60 cm^2/Vs above 200 ℃ in N_2 regardless of hydrogen flow ratio. Then, as the annealing temperature continues to increase, the Hall mobility drops to below 10 cm^2/Vs. Carrier

density of InO_x:H films decrease from 10^{20} to 10^{18} cm^{-3} with the annealing temperature increasing. The results demonstrated that the introduction of hydrogen increased Hall mobility of InO_x:H films significantly after annealing in N_2. For as-deposited films, the Hall mobility decreased and carrier density increased with the increase of hydrogen. It is considered that impurity scattering originating from doped hydrogen in films was increased, leading to the decrease of Hall mobility. In addition, doped impurities ionized, leading to a increase of carrier density.

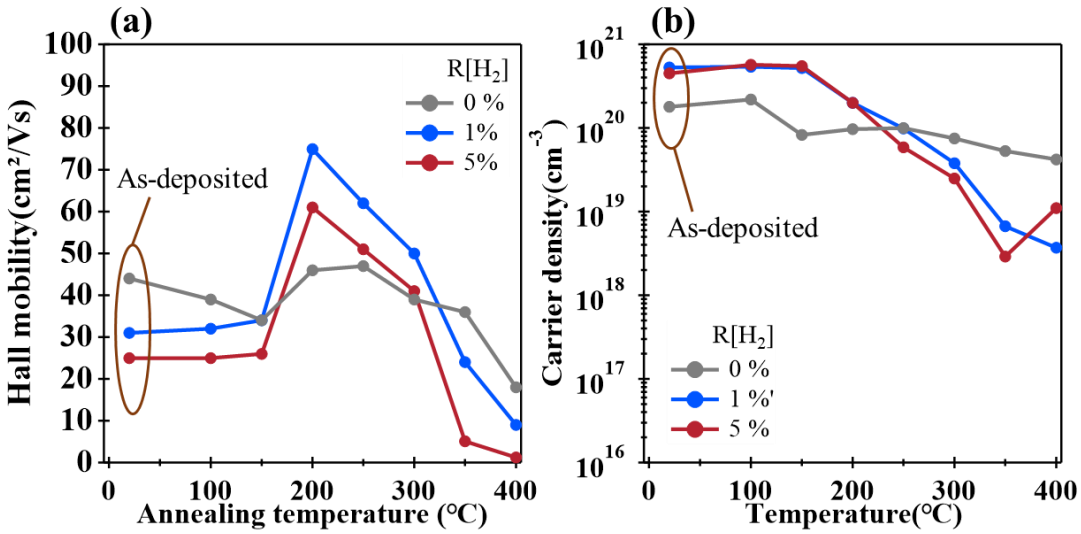

Figure 3. 5 (a) Hall mobility and (b) carrier density of InO_x and InO_x:H films with hydrogen flow ratio of 1% and 5% as a function of annealing temperature (in N_2).

Figure 3. 6 shows Hall mobility and carrier density of InO_x and InO_x:H films with different hydrogen flow ratios as a function of annealing time in N_2 at a temperature of 250 ℃. Figure 3. 7 shows SEM surface views of InO_x and InO_x:H films before and after annealing at 250 ℃ for 5 and 60 min. InO_x film exhibits constant Hall mobility and carrier density with the extension of annealing time. InO_x films maintained nanocrystalline phase before and after annealing. On the other hand, Hall mobility of InO_x:H films rapidly

increased to maximum value within 5 min due to SPC, regardless of the hydrogen flow ratio during deposition. As the annealing time extends, the Hall mobility and carrier density of InO_x:H films were approximately 60 cm^2/Vs and ~10^{20} cm^{-3}, respectively. InO_x:H film was converted from amorphous phase to polycrystalline phase within 5 min, resulting in a large grain size, as shown in Figure 3. 7. The grain size did not show a significant change with an annealing time extension to 60 min, as shown in Figure 3. 7, which corresponds well with the results of the time dependence of electrical properties. In contrast to InO_x film, which maintains a constant carrier density after annealing, the carrier density of InO_x:H film decreases with increasing H_2 flow ratio after annealing in N_2. With an increase in H_2 flow ratio to 5%, the carrier concentration drops by an order of magnitude after annealing. Next, the change in chemical bonding states during SPC was investigated by HAXPES and TDS.

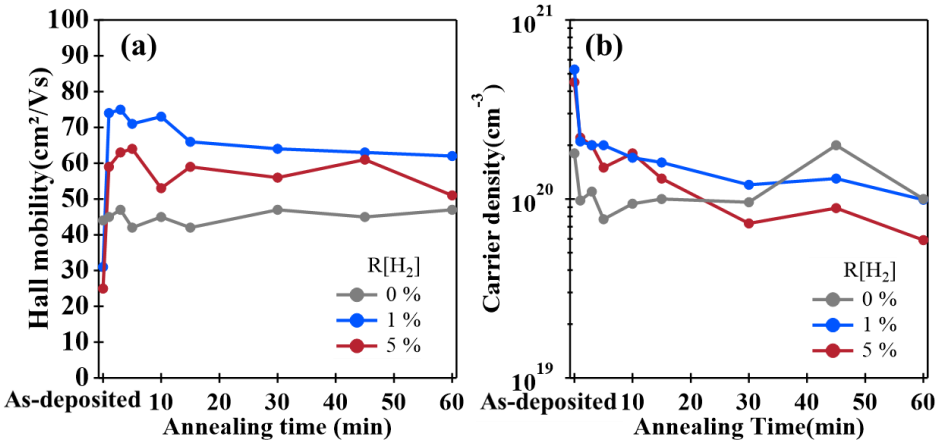

Figure 3. 6 (a) Hall mobility and (b) carrier density of InO_x and InO_x:H films with oxygen flow ratio of 1% and 5% as a function of annealing time (in N_2).

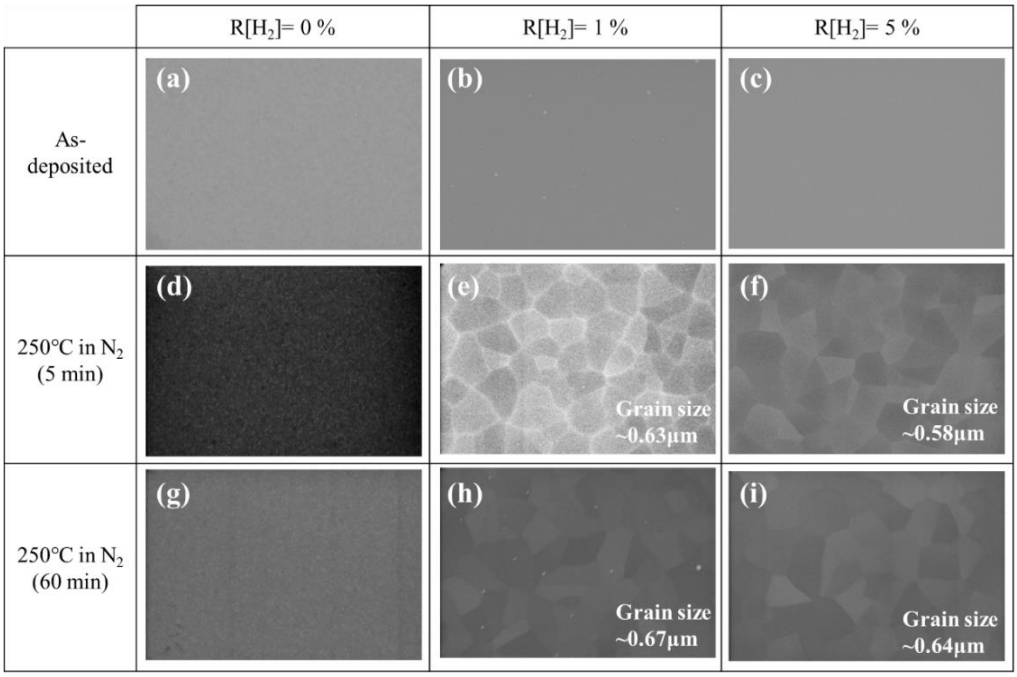

Figure 3. 7 SEM surface views of (a) as-deposited, annealing for (d) 5 and (g) 60 min InO_x films, respectively; (b) as-deposited, annealing at 250 ℃ for (e) 5 and (h) 60 min InO_x:H films($R[H_2]$ = 1%); (c) as-deposited, annealing for (f) 5 and (i) 60 min InO_x:H films($R[H_2]$ = 5%).

The chemical bonding states of InO_x and InO_x:H films were evaluated by HAXPES in order to characterize their chemical composition. Figure 3. 8 shows O 1s spectra obtained from both the InO_x and InO_x:H ($R[H_2]$ = 5%) samples before and after annealing in N_2 at 250 °C. A noticeable difference is a shoulder in the region of higher binding energy was found between the as-deposited InO_x and InO_x:H samples, as shown in Figure 3. 8(a), while a reduction of disparity in the same region was observed, as shown in Figure 3. 8(b). The obtained O 1s spectra after deconvolution are shown in Figure 3. 8(c) and (d). According to the best fitting, the corresponding binding energies were assigned to 530.0 eV, 530.6 eV, and 531.8 eV as the metal-oxygen (M-O), oxygen vacancies (V_O), and oxygen in the hydroxides (-OH), respectively.[25–28] Table 3. 3 is a summary of the relative area ratio of the M-O, V_O, and -OH in InO_x and InO_x:H films. The initial content

of chemical bonds in InO_x and InO_x:H films shows significant differences. Relative area ratio of M-O (R[M-O]) decreased, and V_O (R[V_O]) and -OH (R[-OH]) increased with the increase of H_2 flow ratio. Hydrogen doped in InO_x:H films acts as -OH, resulting in the increase of V_O. The relative area ratio of the chemical bonds, including M-O, V_O, and -OH, almost did not change in the InO_x films. The introduction of hydrogen promotes the formation of V_O and -OH. Then, R[M-O] increases, and R[V_O] decreases enormously after annealing in N_2. Due to the precision limitations of HAXPES, the differences and variations of hydrogen in the film cannot be clearly compared. Next, the changes of hydrogen in the film will be discussed using the TDS method.

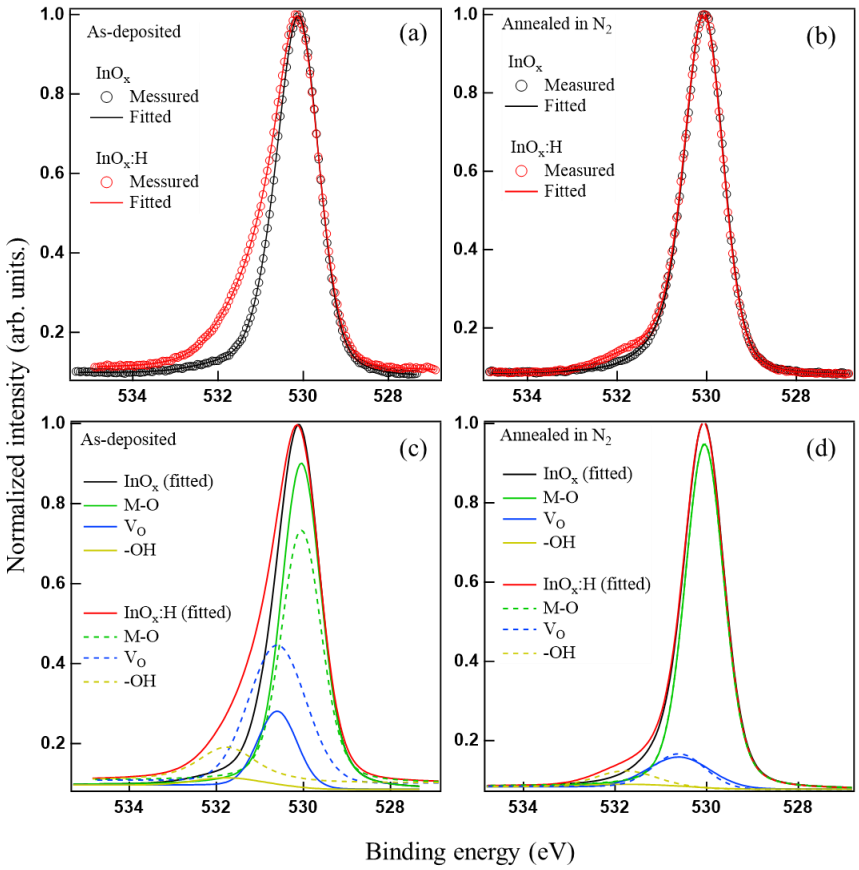

Figure 3. 8 HAXPES analysis of InO_x and InO_x:H films: O 1s spectra of (a) and (c) as-deposited before and after deconvolution, respectively; (b) and (d) annealed films in N_2 for 60 min before and after deconvolution.

Table 3. 3 Relative area ratio of the M-O, V_O, and -OH in InO_x and InO_x:H films deposited at fixed R[O_2] of 4% and at various R[H_2] before and after annealing at 250 °C for 60 min.

	Hydrogen flow ratio (%)	R[M-O] (%)	R[Vo] (%)	R[-OH] (%)
As-deposited	0	87.52	10.35	2.13
	1	61.37	32.76	5.86
	5	57.05	37.01	5.93
After annealing	0	87.69	11.04	1.27
	1	81.56	13.83	4.61
	5	85.06	9.70	5.24

Figure 3. 9 shows TDS spectra of H_2 and H_2O for InO_x (R[H_2] = 0) and InO_x:H films (R[H_2] = 1, 5%). These desorption states reflected the crystallization process, changes in chemical structure, and composition of the film. There is no change in H_2 desorption with the introduction of hydrogen. On the other hand, the results of desorption of H_2O exhibited significant change. InO_x film shows the smallest desorption peak of H_2O during the whole measurement process. Compared to InO_x film, InO_x:H film shows obvious H_2O desorption peak at the stage temperature of ~200 ℃ and 600~800 ℃. SPC started at approximately 200 ℃ with a desorption peak of H_2O, as shown in Figure 3. 9 (b). InO_x:H films with R[H_2] of 1% exhibited a lower H_2O desorption peak than that of films with R[H_2] of 5%. The H_2O desorption peak located at the stage temperature of 600~800 ℃ is attributed to -OH.[24] It is indicated that doped hydrogen acts as interstitial H and -OH in InO_x:H films. Ionized H increased the impurity scattering, leading to a decrease in Hall mobility. Interstitial H was desorbed at temperature of ~200 ℃ as H_2O, resulting in dramatical structural rearrangements. The content of -OH increased with the increase of hydrogen flow ratio. It is considered that the balance of impurity scattering caused by

interstitial H and -OH formed by doped H and intrinsic oxygen plays an important role in improvement of Hall mobility.

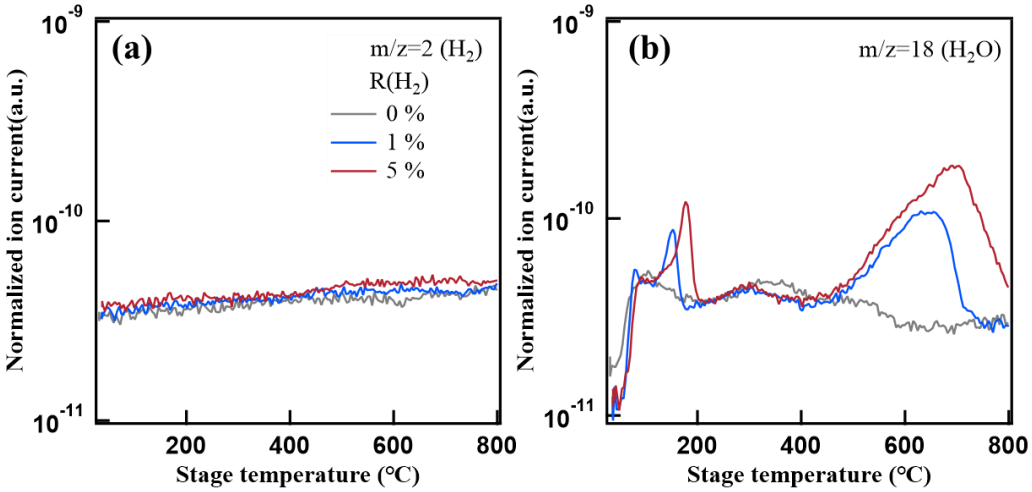

Figure 3. 9 TDS spectra of as-deposited (a) H_2 and (b) H_2O for InO_x and InO_x:H films with different H_2 flow ratios during deposition.

3.3.2 Effect of oxygen flow ratio on the electrical properties of InO_x:H films

Figure 3. 10 shows Hall mobility and carrier density of InO_x:H films deposited at fixed $R[H_2]$ of 5% and at various $R[O_2]$ as a function of annealing temperature in N_2 for 60 min. Hall mobility of as-deposited InO_x:H films increased with the increase of $R[O_2]$. As described above, a portion of doped hydrogen acts as ionized interstitial hydrogen. It is considered that excess ionized H increased impurity scattering, resulting in the decrease of Hall mobility.

As described above, the Hall mobility of InO_x:H films increased enormously when SPC occurred. InO_x:H films with $R[O_2]$ of 2% required a higher SPC temperature of above 250 ℃. Carrier density of all the films decreased by one to two orders of magnitude with annealing temperature increasing, regardless of $R[O_2]$.

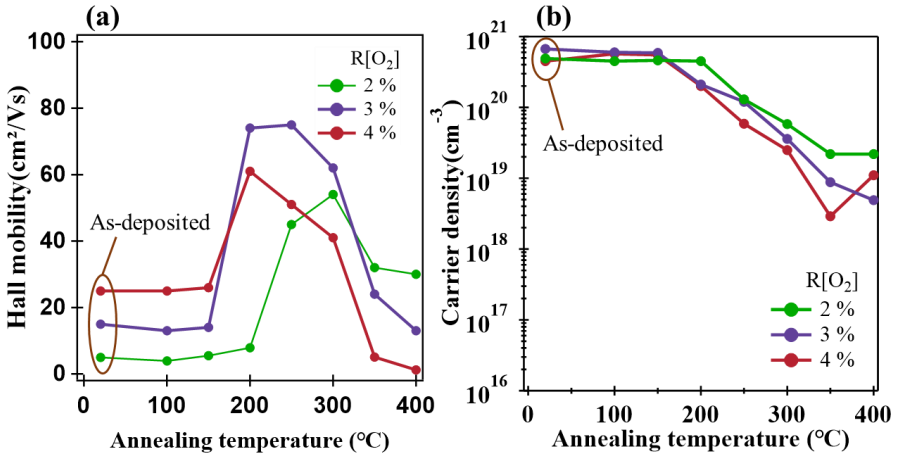

Figure 3. 10 (a) Hall mobility and (b) carrier density of InO_x:H films with oxygen range from 2% to 4% as a function of annealing temperature (in N_2).

Figure 3. 11 shows Hall mobility and carrier density of InO_x:H films with R[O_2] ranging from 2% to 4% as a function of annealing time at 250°C (in N_2). Figure 3. 12 shows SEM surface views of InO_x:H films before and after annealing at 250 °C for 5 and 60 min in N_2. SPC of all the films completed within 5 min, with an increase in Hall mobility, regardless of R[O_2] during deposition. All the films exhibited the same trend in Hall mobility, indicating that R[O_2] showed little effect on the SPC process. SEM surface of all the polycrystalline InO_x:H films did not exhibit noticeable differences in grain size. It is noticeable that the carrier density of InO_x:H films with R[O_2]-R[H_2] of 4-5% decreased by an order of magnitude after SPC, indicating the intrinsic oxygen decreased carrier density during SPC.

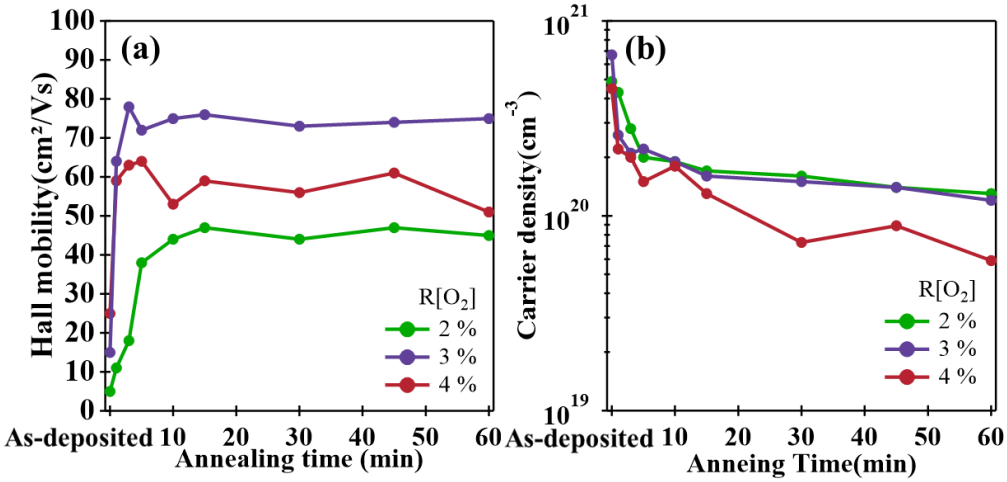

Figure 3. 11 (a) Hall mobility and (b) carrier density of InO_x:H films with oxygen range from 2% to 4% as a function of annealing time (in N_2).

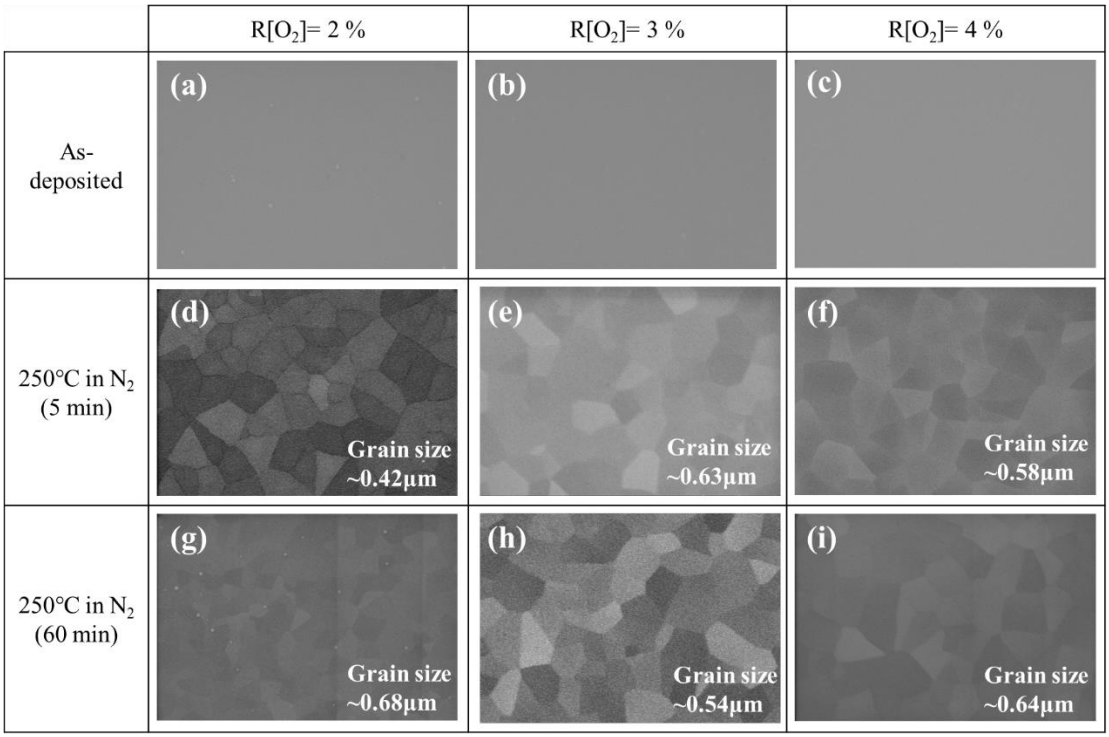

Figure 3. 12 SEM surface views of InO_x:H films (a) before and after annealing for (d) 5 and (g) 60 min[R[O_2] = 2%]; InO_x:H films (b) before and after annealing for (e) 5 and (h) 60 min[R[O_2] = 3%]; InO_x:H films (c) before and after annealing for (f) 5 and (i) 60 min[R[O_2] = 4%].

Figure 3. 13 shows O 1s spectra obtained from both InO_x:H samples with R[O_2] ranging from 2% to 4% before and after annealing at 250 ℃ for 60 min. Table 3. 4 is a summary of the relative area ratio of the M-O, V_O, and -OH. For as-deposited films, the R[V_O] did not show significant changes with the increase in R[O_2]. However, as the R[O_2] increased from 2% to 4%, the R[V_O] decreased from 21.13% to 9.70% after annealing, as shown in Figure 3. 13 and Table 3. 4. Although the increase of R[O_2] during film deposition did not markedly change the R[V_O] before annealing, it influenced the stability of these V_O during thermal treatment. The annealing enhances the passivation of V_O, leading to a rearrangement of crystal and the increase of Hall mobility.

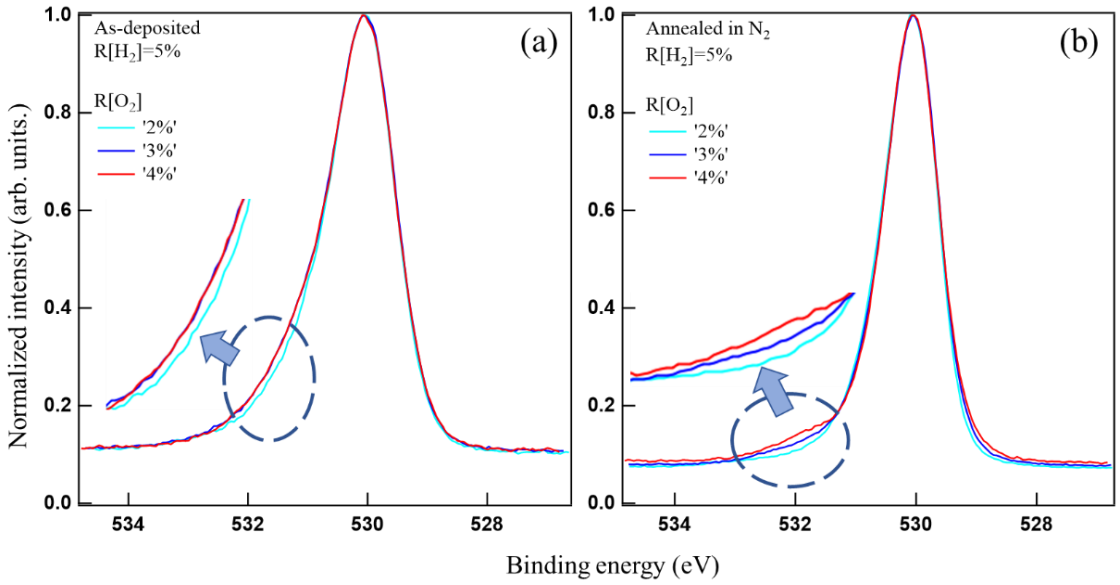

Figure 3. 13 HAXPES analysis of InO_x:H films deposited at fixed R[H_2] of 5% and at various R[O_2]: O 1s spectra of (a) as-deposited and (b) annealed samples.

Table 3. 4 Relative area ratio of the M-O, V_O, and -OH in InO_x:H films deposited at fixed R[H_2] of 5% and at various R[O_2] before and after annealing at 250 °C for 60 min.

	oxygen flow ratio (%)	M-O (%)	V_O (%)	-OH (%)
As-deposited	2	57.87	35.56	6.57
	3	54.28	38.88	6.85
	4	57.05	37.01	5.93
After annealing	2	73.46	21.13	5.40
	3	79.17	15.96	4.87
	4	85.06	9.70	5.24

Figure 3. 14 shows TDS spectra of H_2 and H_2O for as-deposited InO_x:H films with R[O_2] ranging from 2% to 4% during deposition. When R[O_2] decreases to 2%, a desorption peak for H_2 is observed at 20 0℃, corresponding with a desorption peak for H_2O at the same temperature due to SPC. InO_x:H film with R[O_2] of 2% shows the highest desorption peak of H_2O at a stage temperature of ~200 ℃ and the smallest peak at a stage temperature of 600~800 ℃. Intrinsic oxygen plays a crucial role in stabilizing hydrogen. Excessive interstitial H desorbs significantly into H_2 and H_2O at 200 ℃, as shown in Figure 3. 1, resulting in lower Hall mobility. The increase of -OH decreased Hall mobility for films with R[O_2] increasing from 3% to 4%. It is considered that excessive H or O will result in the reduction of Hall mobility due to impurity scattering and -OH, respectively. Therefore, InO_x:H film with R[O_2] of 3% achieved an optimal equilibrium between scattering suppression and -OH, obtaining a high Hall mobility of 75 cm^2/Vs.

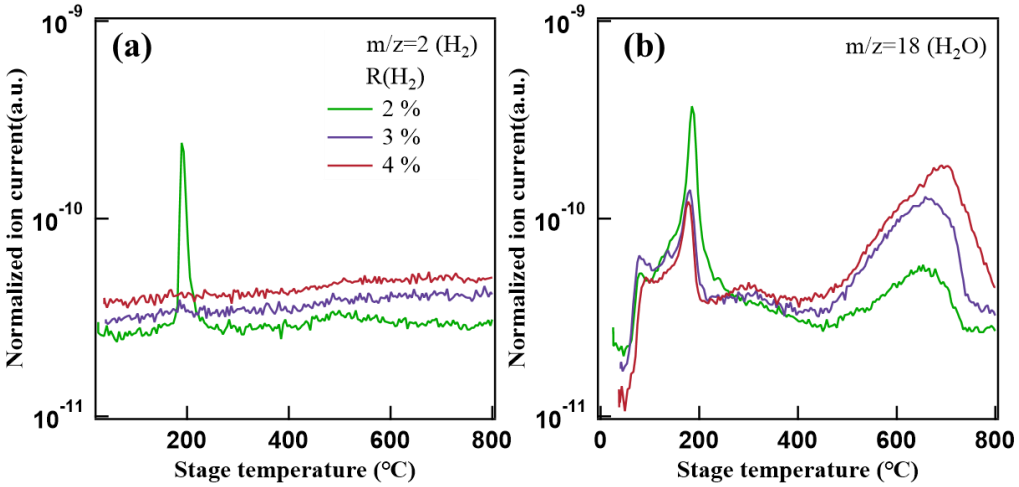

Figure 3. 14 TDS spectra of as-deposited (a) H_2 and (b) H_2O for InO_x:H films with O_2 flow ratios ranging from 2~4% during deposition.

3.4 Conclusion

In this chapter, InO_x and InO_x:H films with various oxygen and hydrogen flow ratios were deposited by RF magnetron sputtering. The structure and electrical properties, and chemical bonding states of both the InO_x and InO_x:H films were investigated to clarify the effect of the gas flow ratio during deposition.

1. Hydrogen acts as shallow donor to adjust electrical properties. Hydrogen doped in InO_x film acted as interstitial H and -OH, resulting in changes in as-deposited InO_x film. Furthermore, the introduction of hydrogen promoted the formation of V_O, resulting in a decrease in the Hall mobility. Impurity scattering, originating from interstitial H and V_O, decreased Hall mobility for as-deposited film. The oxygen adjusted the ionized interstitial H and free carrier in as-deposited films. At a low oxygen flow ratio, ionized H increased, resulting in the decrease of Hall mobility due to increasing impurity scattering.

2. Solid phase crystallization occurred at the annealing temperature of ~200 ℃ in N_2 for InO_x:H films, resulting in a significant increase of Hall mobility to 60~70 cm^2/Vs. In

contrast, the Hall mobility of InO_x films did not exhibit an enormous increase after annealing. It is considered that InO_x films exhibited a nanocrystalline phase. The introduction of hydrogen caused dramatical structural rearrangements by SPC, leading to a large grain size in polycrystalline film. The oxygen has a significant impact on the SPC process. A high $R[O_2]$ promoted the passivation of oxygen vacancies during SPC and reduced the SPC temperature. Oxygen enhanced the stability of hydrogen in the film, leading to the reduction of H_2 and H_2O desorption during the SPC process, while increasing the relative area ratio of -OH in the film.

3. After annealing, hydrogen desorbed from the InO_x:H film in the form of H_2 and H_2O, leading to a decrease in the relative area ratio of V_O. Ionized H and V_O were passivated by SPC, causing the increase in Hall mobility. However, during the SPC process, the reduction of defects and the increase in grain size, due to the introduction of hydrogen, significantly improved the Hall mobility of InO_x:H films. Even though H promoted the formation of V_O, significant passivation of V_O occurred during SPC, reducing its relative area ratio to ~10%, which is the same as that of InO_x:H films. The intrinsic oxygen affected the electrical properties of the film after annealing. At high $R[O_2]$ during deposition, the relative area ratio of V_O decreased, resulting in a further reduction in carrier density after SPC. In addition, excessive H or O will result in the reduction of Hall mobility due to impurity scattering and -OH, respectively.

References

1. Nomura, K.; Ohta, H.; Takagi, A.; Kamiya, T.; Hirano, M.; Hosono, H. Room-Temperature Fabrication of Transparent Flexible Thin-Film Transistors Using Amorphous Oxide Semiconductors. *Nature* **2004**, *432*, 488–492, doi:10.1038/nature03090.
2. Weiher, R.L. Electrical Properties of Single Crystals of Indium Oxide. *J. Appl. Phys.* **2004**, *33*, 2834–2839, doi:10.1063/1.1702560.
3. Buchholz, D.B.; Ma, Q.; Alducin, D.; Ponce, A.; Jose-Yacaman, M.; Khanal, R.; Medvedeva, J.E.; Chang, R.P.H. The Structure and Properties of Amorphous Indium Oxide. *Chem. Mater.* **2014**, *26*, 5401–5411, doi:10.1021/cm502689x.
4. Shigesato, Y.; Paine, D.C. Study of the Effect of Sn Doping on the Electronic Transport Properties of Thin Film Indium Oxide. *Applied Physics Letters* **1993**, *62*, 1268–1270, doi:10.1063/1.108703.
5. Koida, T.; Ueno, Y.; Shibata, H. In_2O_3-Based Transparent Conducting Oxide Films with High Electron Mobility Fabricated at Low Process Temperatures. *Phys. Status Solidi* **2018**, *215*, 1700506, doi:10.1002/pssa.201700506.
6. Granqvist, C.G. Transparent Conductive Electrodes for Electrochromic Devices: A Review. *Appl. Phys. A* **1993**, *57*, 19–24, doi:10.1007/BF00331211.
7. van Hest, M.F.A.M.; Dabney, M.S.; Perkins, J.D.; Ginley, D.S.; Taylor, M.P. Titanium-Doped Indium Oxide: A High-Mobility Transparent Conductor. *Applied Physics Letters* **2005**, *87*, 032111, doi:10.1063/1.1995957.
8. Asikainen, T.; Ritala, M.; Leskelä, M. Atomic Layer Deposition Growth of Zirconium Doped In_2O_3 Films. *Thin Solid Films* **2003**, *440*, 152–154, doi:10.1016/S0040-6090(03)00822-8.
9. Meng, Y.; Yang, X.; Chen, H.; Shen, J.; Jiang, Y.; Zhang, Z.; Hua, Z. A New Transparent Conductive Thin Film In_2O_3:Mo. *Thin Solid Films* **2001**, *394*, 218–222, doi:10.1016/S0040-6090(01)01142-7.
10. Newhouse, P.F.; Park, C.-H.; Keszler, D.A.; Tate, J.; Nyholm, P.S. High Electron Mobility W-Doped In_2O_3 Thin Films by Pulsed Laser Deposition. *Applied Physics Letters* **2005**, *87*, 112108, doi:10.1063/1.2048829.
11. Ebata, K.; Tomai, S.; Tsuruma, Y.; Iitsuka, T.; Matsuzaki, S.; Yano, K. High-Mobility Thin-Film Transistors with Polycrystalline In–Ga–O Channel Fabricated by DC Magnetron Sputtering. *Appl. Phys. Express* **2012**, *5*, 011102,

doi:10.1143/APEX.5.011102.

12. Wang, H.; He, J.; Xu, Y.; André, N.; Zeng, Y.; Flandre, D.; Liao, L.; Li, G. Impact of Hydrogen Dopant Incorporation on InGaZnO, ZnO and In_2O_3 Thin Film Transistors. *Phys. Chem. Chem. Phys.* **2020**, *22*, 1591–1597, doi:10.1039/C9CP05050G.
13. Abliz, A.; Huang, C.-W.; Wang, J.; Xu, L.; Liao, L.; Xiao, X.; Wu, W.-W.; Fan, Z.; Jiang, C.; Li, J.; et al. Rational Design of ZnO:H/ZnO Bilayer Structure for High-Performance Thin-Film Transistors. *ACS Appl. Mater. Interfaces* **2016**, *8*, 7862–7868, doi:10.1021/acsami.5b10778.
14. Abliz, A.; Gao, Q.; Wan, D.; Liu, X.; Xu, L.; Liu, C.; Jiang, C.; Li, X.; Chen, H.; Guo, T.; et al. Effects of Nitrogen and Hydrogen Codoping on the Electrical Performance and Reliability of InGaZnO Thin-Film Transistors. *ACS Appl. Mater. Interfaces* **2017**, *9*, 10798–10804, doi:10.1021/acsami.6b15275.
15. Gaspar, D.; Pereira, L.; Gehrke, K.; Galler, B.; Fortunato, E.; Martins, R. High Mobility Hydrogenated Zinc Oxide Thin Films. *Solar Energy Materials and Solar Cells* **2017**, *163*, 255–262, doi:10.1016/j.solmat.2017.01.030.
16. Kronenberger, A.; Polity, A.; Hofmann, D.M.; Meyer, B.K.; Schleife, A.; Bechstedt, F. Structural, Electrical, and Optical Properties of Hydrogen-Doped ZnO Films. *Phys. Rev. B* **2012**, *86*, 115334, doi:10.1103/PhysRevB.86.115334.
17. Nomura, K.; Kamiya, T.; Hosono, H. Effects of Diffusion of Hydrogen and Oxygen on Electrical Properties of Amorphous Oxide Semiconductor, In-Ga-Zn-O. *ECS J. Solid State Sci. Technol.* **2012**, *2*, P5, doi:10.1149/2.011301jss.
18. Velichko, R.; Magari, Y.; Furuta, M. Defect Passivation and Carrier Reduction Mechanisms in Hydrogen-Doped In-Ga-Zn-O (IGZO:H) Films upon Low-Temperature Annealing for Flexible Device Applications. *Materials* **2022**, *15*, 334, doi:10.3390/ma15010334.
19. Aman, S.G.M.; Magari, Y.; Shimpo, K.; Hirota, Y.; Makino, H.; Koretomo, D.; Furuta, M. Low-Temperature (150 °C) Activation of $Ar+O_2+H_2$-Sputtered In–Ga–Zn–O for Thin-Film Transistors. *Appl. Phys. Express* **2018**, *11*, 081101, doi:10.7567/APEX.11.081101.
20. Kataoka, T.; Magari, Y.; Makino, H.; Furuta, M. Nondegenerate Polycrystalline Hydrogen-Doped Indium Oxide (InOx:H) Thin Films Formed by Low-Temperature Solid-Phase Crystallization for Thin Film Transistors. *Materials* **2022**, *15*, 187, doi:10.3390/ma15010187.

21. Magari, Y.; Kataoka, T.; Yeh, W.; Furuta, M. High-Mobility Hydrogenated Polycrystalline In_2O_3 (In_2O_3:H) Thin-Film Transistors. *Nat. Commun.* **2022**, *13*, 1078, doi:10.1038/s41467-022-28480-9.

22. Koida, T.; Fujiwara, H.; Kondo, M. Hydrogen-Doped In2O3 as High-Mobility Transparent Conductive Oxide. *Jpn. J. Appl. Phys.* **2007**, *46*, L685, doi:10.1143/JJAP.46.L685.

23. Koida, T.; Fujiwara, H.; Kondo, M. High-Mobility Hydrogen-Doped In_2O_3 Transparent Conductive Oxide for a-Si:H/c-Si Heterojunction Solar Cells. *Sol. Energy Mater. Sol. Cells* **2009**, *93*, 851–854, doi:10.1016/j.solmat.2008.09.047.

24. Koida, T.; Kondo, M.; Tsutsumi, K.; Sakaguchi, A.; Suzuki, M.; Fujiwara, H. Hydrogen-Doped In_2O_3 Transparent Conducting Oxide Films Prepared by Solid-Phase Crystallization Method. *J. Appl. Phys.* **2010**, *107*, 033514, doi:10.1063/1.3284960.

25. Magari, Y.; Furura, M. Effects of Water and Hydrogen Introduction during In–Ga–Zn–O Sputtering on the Performance of Low-Temperature Processed Thin-Film Transistors. *Jpn. J. Appl. Phys.* **2021**, *60*, SBBM04, doi:10.35848/1347-4065/abd9d2.

26. Detweiler, Z.M.; Wulfsberg, S.M.; Frith, M.G.; Bocarsly, A.B.; Bernasek, S.L. The Oxidation and Surface Speciation of Indium and Indium Oxides Exposed to Atmospheric Oxidants. *Surface Science* **2016**, *648*, 188–195, doi:10.1016/j.susc.2015.10.026.

27. Reddy, I.N.; Venkata Reddy, C.; Cho, M.; Shim, J.; Kim, D. Structural, Optical and XPS Study of Thermal Evaporated In_2O_3 Thin Films. *Mater. Res. Express* **2017**, *4*, 086406, doi:10.1088/2053-1591/aa7f59.

28. Barr, T.L.; Ying Li Liu An X-Ray Photoelectron Spectroscopy Study of the Valence Band Structure of Indium Oxides. *Journal of Physics and Chemistry of Solids* **1989**, *50*, 657–664, doi:10.1016/0022-3697(89)90001-2.

Chapter 4

Solid phase crystallization mechanism in Hydrogen-doped InO_x films

4.1 Introduction

Crystallization occurred when hydrogen-doped InO_x film was annealed at a low temperature of 250℃ in N_2, resulting in a significant increase in Hall mobility as described in Chapter 3, indicating that crystallization is a key process in improving the structural and electrical properties of oxide semiconductors. Since the first report of epitaxial reordering of amorphous silicon on a crystalline silicon substrate in 1968 by Mayer et al.[1] A large number of research on solid phase crystallization (SPC) was performed for decades years. Polycrystalline semiconductor thin films have attracted great attention for a wide variety of applications, such as solar cells[2,3], channel layers of thin film transistors[4–6], and sensors[7–9]. Table 4. 1 shows the comparison of crystallization methods and their typical applications in Semiconductors. In addition to SPC, there are several other methods that can be applied to the crystallization of semiconductors, such as CVD, laser annealing, and metal-induced crystallization (MIC). However, these methods each come with their own limitations. For instance, CVD and laser annealing require high temperature, which are unsuitable for flexible TFT application. MIC method can affect the electrical properties of the semiconductor film due to metal contamination[10,11]. Currently, SPC has been a common method for the fabrication of high-performance semiconductors.

Table 4. 1 Comparison of crystallization methods and their typical applications in Semiconductors.

Crystallization method	Temperature	Typical Semiconductor Materials	Reference
Solid phase crystallization	175 ~ 400 ℃	Oxide semiconductors, amorphous Si	[12]
CVD	800 ~ 1200 ℃	Si, GaAs, oxide semiconductor	[13]
Laser Annealing	800 ~ 1200 ℃	Amorphous Si	[14]
Metal-Induced Crystallization	200 ~ 600 ℃	Amorphous Si, oxide semiconductors	[15]
Melt Crystallization	>1000 ℃	Si, compound semiconductors	[16]
Solution process	~200 ℃	Organic material	[17]

It is shown that the improvement in grain size is the main cause of the increase in Hall mobility. In order to enlarge grain size to obtain the best optoelectronic properties, Macco et al.[18] reported the SPC- In_2O_3:H TCO films prepared by atomic layer deposition (ALD). To obtain the best optoelectronic properties for TCO application, it is crucial to deposit the In_2O_3:H films at the lowest possible temperature of ALD method because a low density of embedded crystallites acts as seeds for further crystallization, resulting in a large grain size after SPC.

However, most of the SPC poly-InO_x:H have focused on their film thickness of more than 100 nm for TCO applications. On the other hand, there are few papers on the study of the SPC poly-InO_x:H for TFT applications with a thickness of less than 50 nm. The understanding of SPC process for very thin (<50 nm) InO_x:H film, such as nucleation density and lateral growth rate, is essential for TFT applications.

In this chapter, we investigated the phase transition mechanism of 30-nm-thick

amorphous InO_x:H into poly-InO_x:H films during SPC process in detail. Nucleation density and lateral growth rate of the InO_x:H films were evaluated using electron backscatter diffraction (EBSD) measurements by varying the ramp rate and hold time during SPC process.

4.2 Experiment

In this experiment, 30-nm-thick InO_x and InO_x:H films were deposited by radio frequency magnetron sputtering from a ceramic In_2O_3 target at room temperature on glass or SiO_2 (100 nm)/Si substrates. Mixed gases of Ar, O_2, and H_2 were used to deposit InO_x and InO_x:H films. The O_2 gas flow ratio was set at 3% for both films, while the H_2 gas flow ratio was set at 0 and 5% for InO_x and InO_x:H films, respectively. All the films were deposited at 0.4 Pa. Then, the films were annealed in N_2 by rapid thermal annealing (RTA, ULVAC, MILA-3000) at temperatures (T_A) ranging from 100 to 400 ℃. The temperature profile of the RTA was shown in Figure 4. 1. Carrier density and Hall mobility of the films were measured by Hall effect measurements using van der Pauw geometry. Crystallinity and structure properties of the films were evaluated by X-ray diffraction (XRD, Rigaku Smart-Lab) and Electron Backscatter Diffraction (EBSD, AMETEK, EDAX-TSL) analyses. Deposition parameters of InO_x and InO_x:H films are summarized in Table 4. 2. Chemical bonding states of the films were evaluated by hard X-ray photoelectron spectroscopy (HAXPES) system at the BL09XU of SPring-8.

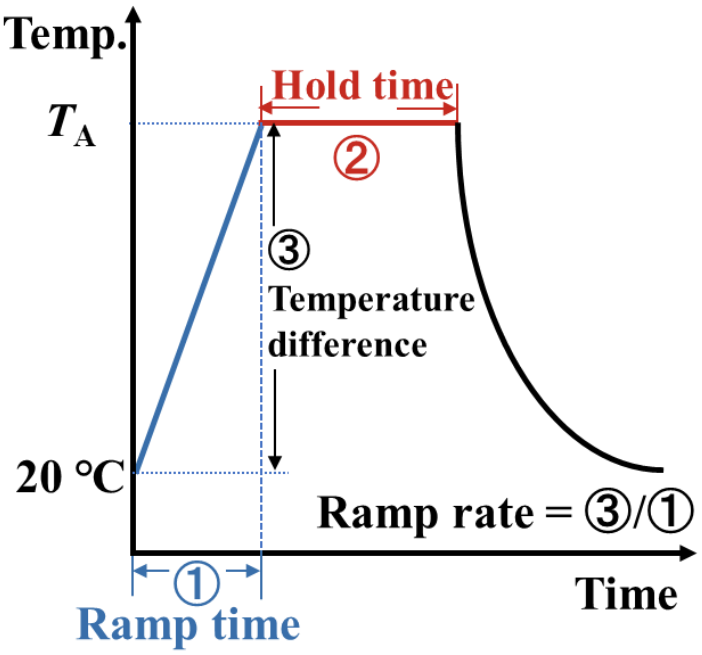

Figure 4. 1 Temperature profile of SPC.

Table 4. 2 Deposition parameters of the H doped InO_x and InO_x:H films.

Target	In_2O_3
Substrate	EAGLE XG Glass
Film thickness	30 nm
Deposition time	1′50″
Back pressure	$< 1\times10^{-4}$ for InO_x $< 3\times10^{-4}$ for InO_x:H
Deposition pressure	0.4 Pa
RF power	200 W
Total gad flow ($Ar+O_2+H_2$)	10 sccm
Deposition temperature (°C)	RT
$R[O_2] = O_2 / (Ar+O_2+H_2)$ (%)	3%
$R[H_2] = H_2 / (Ar+O_2+H_2)$ (%)	5%
Annealing temperature	150 ℃ ~ 400 ℃
Annealing time	0 ~ 60 min
Annealing Ramp rate	5.8 ℃/min ~ 115 ℃/min

4.3 Effect of hydrogen doping on poly-crystalline InO_x and InO_x:H Films

4.3.1 Comparison of crystallinity between InO_x and InO_x:H films

Figure 4. 2 shows the XRD spectra of the (a) InO_x and (b) InO_x:H films before (as-deposited) and after annealing at T_A of 175, 200, and 250 ℃ in N_2 for 3 min. The ramp time, which was shown in Figure 4. 1, was maintained at 2 min for each temperature. Both the InO_x and InO_x:H films showed amorphous phase before annealing. The InO_x film exhibited a polycrystalline nature after annealing at T_A of more than 200 ℃, while the amorphous InO_x:H films were converted to a polycrystalline phase after annealing at T_A of 250 ℃.

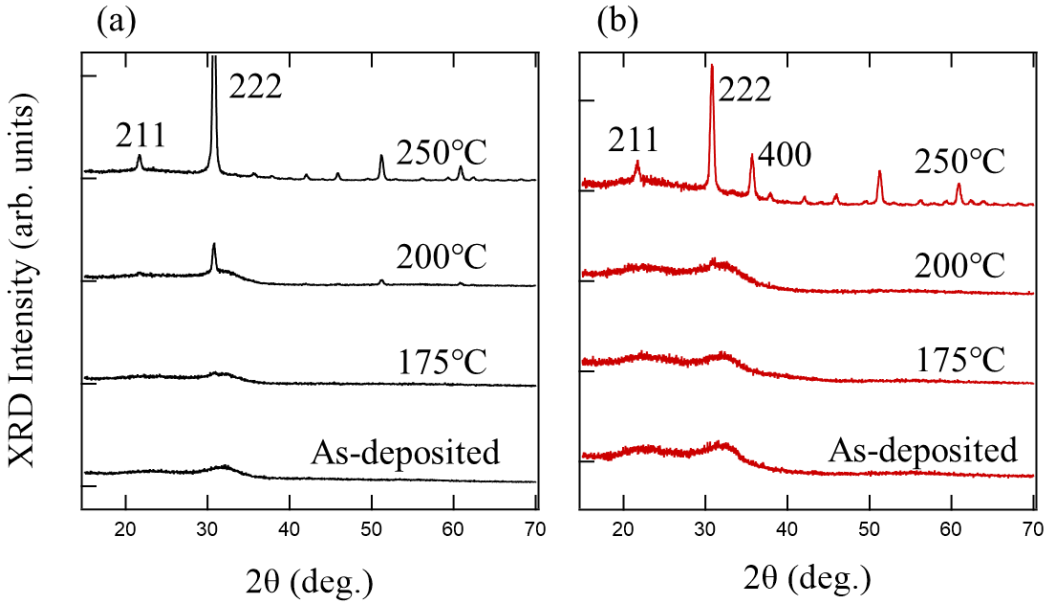

Figure 4. 2 Changes in XRD spectra of (a) InO_x and (b) InO_x:H films before and after annealing at 175, 200, and 250 ℃ for 3 min.

4.3.2 Hydrogen effect on electrical Properties of InO_x:H Films

Figure 4. 3 shows (a) Hall mobility and (b) carrier density of the InO_x and InO_x:H films

as a function of annealing temperature in N_2. The ramp time was maintained at 2 min for each T_A with a hold time for 3 min. After annealing at 250 °C, Hall mobility of the InO_x films increased from 32 (as-deposited) to 47 cm^2/Vs, whereas that of the InO_x:H films increased from 12 to 83 cm^2/Vs. Both the films remained in a degenerate state even after annealing in N_2. Although both the InO_x and InO_x:H films exhibited polycrystalline nature after annealing at 250 °C as shown in Figure 4. 2, Hall mobility of the poly-InO_x:H film markedly increased as compared with the poly-InO_x film. This result indicated that the introduction of hydrogen significantly increased Hall mobility of the poly-InO_x:H film.

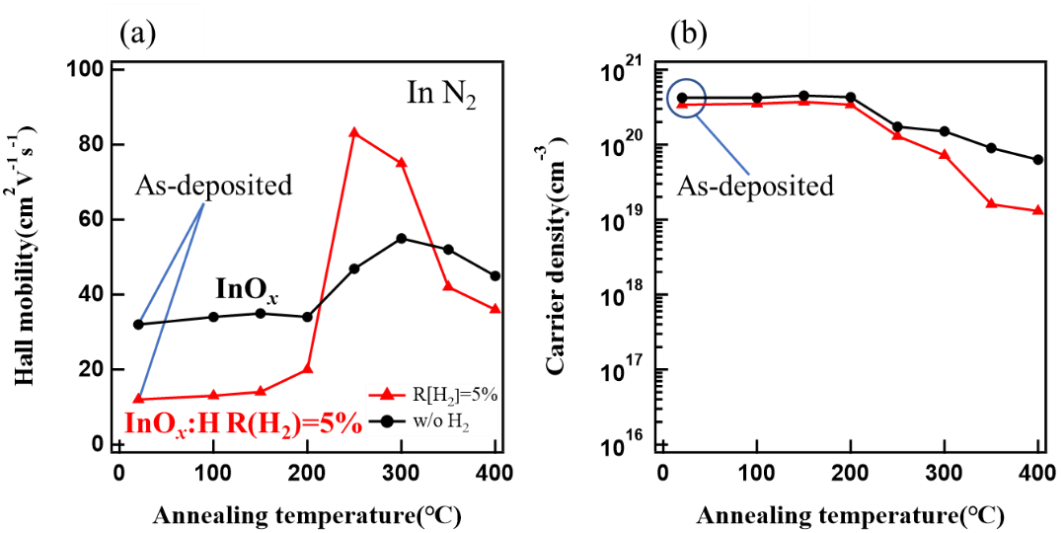

Figure 4. 3 (a) Hall mobility and (b) carrier density of InO_x and InO_x:H films as a function of annealing temperature (in N_2). Ramp and hold time are 2 and 3 min, respectively.

4.3.3 Cause for the increase in Hall mobility of InO_x:H films after SPC

To investigate the main cause of the difference of Hall mobility between poly-InO_x and poly-InO_x:H films, grain size of the as-deposited and 250 °C annealed [hold at 250 °C for 3 min with the ramp time of 2 min (115 °C/min)] InO_x and InO_x:H films were evaluated by EBSD. Area weighted grain size is the most useful 2D method for average grain

sizes.[19–21] Grain size was obtained by following equation:

$$\text{Average grain size} = \sum(d_i \times A_i) / \sum A_i \quad (4.1)$$

Where d_i and A_i are grain size and area fraction, respectively.

Figure 4. 4 shows the EBSD images (probe step 100 nm) and area fraction of grain size for both the InO_x and InO_x:H films. Initially, no grain was observed from both the as-deposited InO_x and InO_x:H films as shown in Figure 4. 4(a) and (b). Both the EBSD and XRD results indicated that the as-deposited InO_x and InO_x:H films were in an amorphous phase. When the hold time (250 ℃) increased for 3 min, both the InO_x and InO_x:H films completely converted to a polycrystalline phase without amorphous region as shown in Figure 4. 4(d) and (e). Figure 4. 4(f) shows the area fraction of the grain size of the InO_x and InO_x:H films after annealing at 250 ℃ with hold time of 3 min. Large grains with 1.03 μm in diameter were observed from the poly-InO_x:H film, while the grain size of the poly-InO_x film was 0.46 μm as shown in Figure 4. 4(f). These results indicated that the enlargement of the grain size plays an important role in the improvement of Hall mobility. Moreover, low-temperature (250 ℃) and fast SPC process is one of great advantages of the poly-InO_x:H film for enhancing the performance of flexible devices.

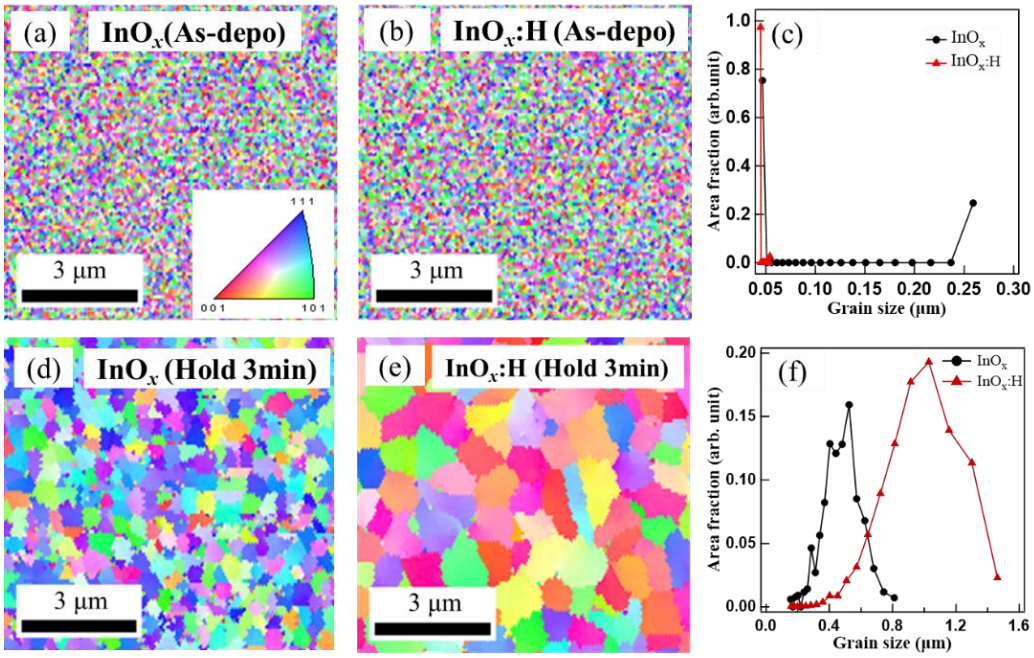

Figure 4. 4 EBSD images of as-deposited and SPC (a, d) InO_x and (b, e) InO_x:H films. SPC was carried out at 250 ℃ for 3 min. Area fraction of grain size of (c) as-deposited and (f) SPC films.

4.4 Mechanism of SPC poly-InO_x:H film

As we previously discussed in chapter 4.3, both the InO_x and InO_x:H films showed poly-crystalline phases with a hold time of 3 min at T_A of 250 ℃ in N_2. To investigate the main cause of the difference in grain size between poly-InO_x and poly-InO_x:H films, the hold time was varied from 0 to 60 min to investigate the process of the nucleation and lateral grain growth at T_A of 250 ℃ in detail. Ramp time was set for 2 min at T_A of 250 ℃.

4.4.1 Effects of H_2 doping on nucleation density and lateral growth rate of InO_x:H film

Figure 4. 5 shows (a) Hall mobility and (b) carrier density of the InO_x and InO_x:H films as a function of hold time at T_A of 250 ℃. Initially, Hall mobility of both the InO_x and InO_x:H films increased with an increase of hold time. Then Hall mobility remained at ~47

cm^2/Vs for the InO_x and ~80 cm^2/Vs for the InO_x:H after holding at 250 ℃ for more than 3min.

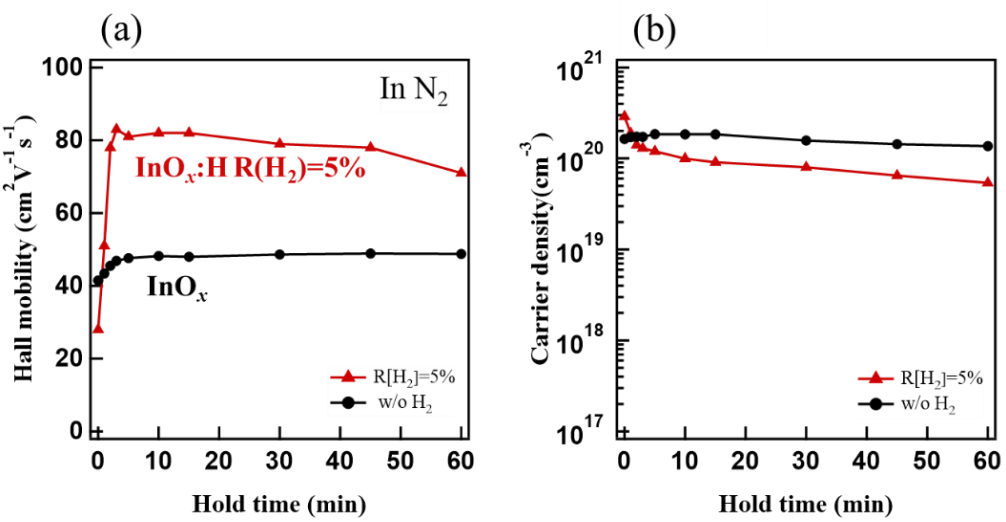

Figure 4. 5 (a) Hall mobility and (b) carrier density of InO_x and InO_x:H films as a function of hold time at 250 ℃ (in N_2).

Figure 4. 6 shows EBSD images and area fraction of grain size for both the InO_x and InO_x:H films annealed at 250 ℃ for 0 to 60 min. The InO_x film showed mostly polycrystalline grains even without a hold time at 250 ℃ as shown in Figure 4. 6(a). Grain size with 0.36 μm in diameter was observed from the InO_x film as shown in Figure 4. 6(c). When the hold time (250 ℃) increased for 3 and 60 min, InO_x films completely converted to a polycrystalline phase with grain size of ~0.54 μm as shown in Figure 4. 6(f) and 6(i). In contrast, The InO_x:H film showed a mixed phase of amorphous and polycrystalline when the hold time of less than 1 min as shown in Figure 4. 6 (b) and (d). Poly-crystalline InO_x:H films with large grain size of ~0.95 μm were obtained, and grain size almost no change when the hold time (250 ℃) increased more than 3 min as shown in Figure 4. 6(g) and (j). Changes in the grain size of the films are well agreed with the Hall mobility of the films.

Nucleation density of the InO_x and InO_x:H films were estimated by the EBSD results shown in Figure 4. 6(a) and (b), respectively. Table 4. 3 shows the nucleation density of both films. Result revealed that the introduction of hydrogen in the film markedly reduced nucleation density from 4.1 μm^{-2} for the InO_x film to 1.1 μm^{-2} for the InO_x:H film, resulting in an increase of the grain size after SPC. The laterally growth rate of crystal nuclei is defined by the grain size difference between the hold time from 0 (0.66 μm) to 1 min (1.10 μm). Lateral growth rate from the nucleus was estimated to be 220 nm/min for the InO_x:H film. Thus, an amorphous InO_x:H film could be converted to a poly-InO_x:H film within 3 min owing to a fast lateral growth rate from the nucleus. Hall mobility also exhibited ~80 cm^2/Vs for the poly-InO_x:H film with the hold time of more than 3 min.

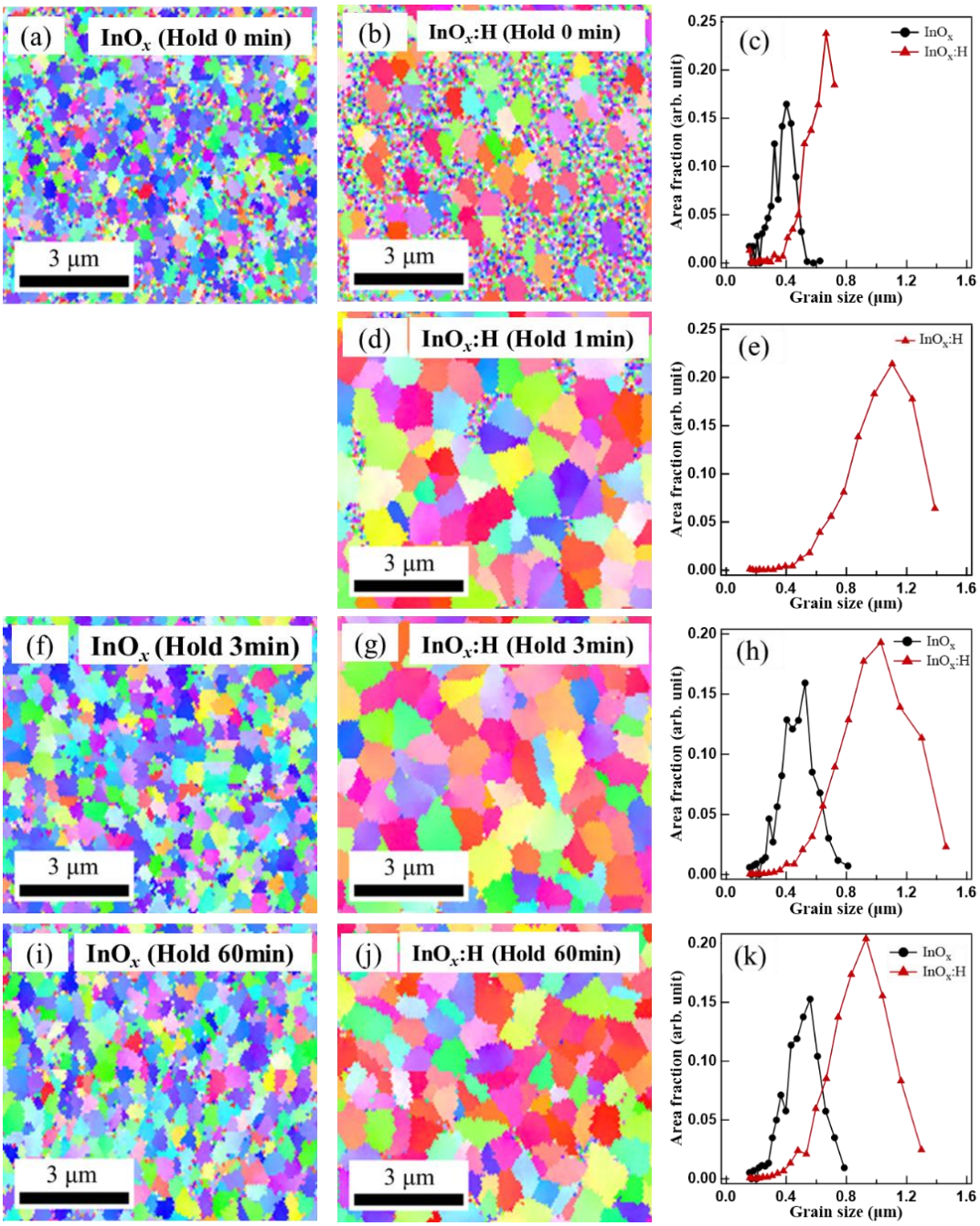

Figure 4. 6 EBSD images of (a, f, and i) InO_x and (b, d, g, and j) InO_x:H films annealed in N_2 at 250 ℃ with different hold time (0, 1, 3, and 60 min). (c, e, h, and k) Area fraction of the grain size of the films with different hold time (0, 1, 3, and 60 min).

Table 4. 3 Nucleation density of films at 250 ℃ without hold time.

Film (Hold 0)	InO_x	InO_x:H
Nucleation density (μm^{-2})	4.1	1.1

Figure 4. 7 shows the HAXPES O 1s core spectra of InO_x:H films as a function of hold time. A significant difference induced by change of V_O as a shoulder in the higher binding energy region was observed for the InO_x:H films. Four clear distinguishable Gaussian–Lorentzian curves after the O 1s spectra deconvolution were assigned to 530.1 eV, 530.6 eV, 531.8 eV, and 533.2 eV, corresponding to the metal-oxygen bonds (M-O), oxygen vacancies (V_O), oxygen-hydrogen (OH), and SiO_2 in substrate, respectively.[22,23] Table 4. 4 is a summary of the relative area ratio of the M-O, V_O, and -OH as a function of hold time. The relative area ratio of the V_O decreased enormously from 49.69% (hold time of 0 min) to 33.50% (hold time of 3 min) with InO_x:H film converted from mixed phase to polycrystalline phase. Then the relative area ratio of the V_O of poly-InO_x:H film decreased slightly from 33.50% to 28.29% with extension of hold time to 60 min. V_O is mainly located at the amorphous phase. After SPC completion, V_O in grain boundary was passivated gradually, without obvious change in grain size.

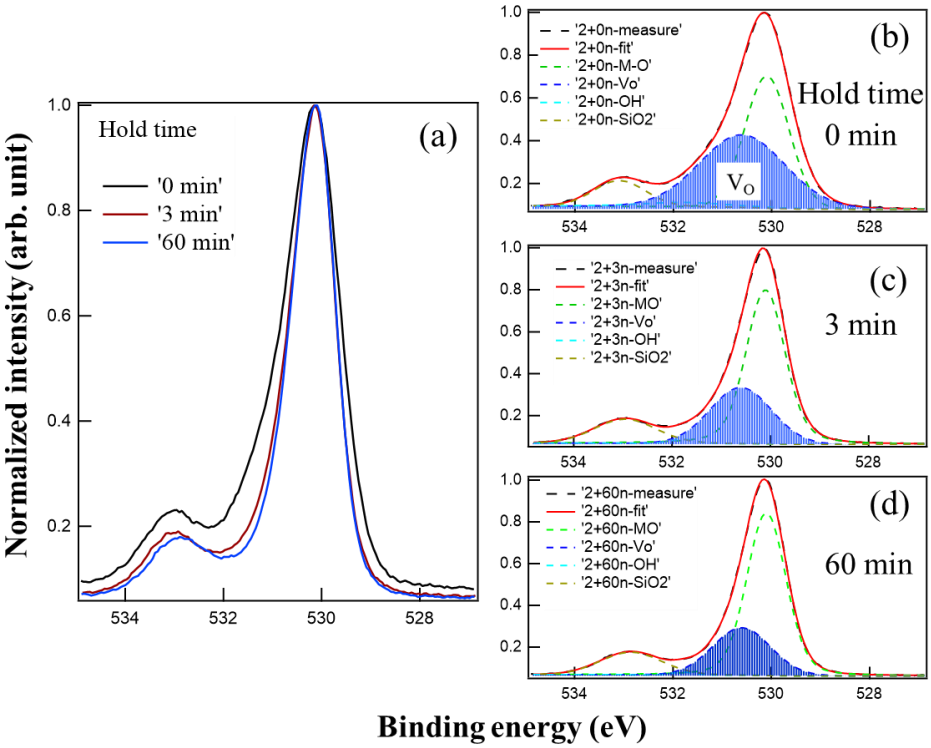

Figure 4. 7 O 1s HAXPES spectra obtained from InO_x:H films as a function of hold time without hold time (a) before and (b)-(c) after deconvolution.

Table 4. 4 Relative area ratio of the M-O, V_O, and -OH in InO_x:H films deposited at R[O_2]-R[H_2] of 3-5% as a function of hold time.

Hold time (min)	M-O (%)	V_O (%)	-OH (%)
0	46.34	49.69	3.98
3	65.55	33.50	0.96
60	71.13	28.29	0.58

As shown in Chapter 3, as-deposited InO_x film exhibited high relative area ratio of M-O (87.52%), then almost no change after annealing (87.69%). On the other hand, relative area ratio of M-O increased from 57.05% for as-deposited InO_x:H film to 85.06% for polycrystalline InO_x:H film.

The results indicated that the grains in polycrystalline phase are primarily composed of M-O. High relative area ratio of M-O promoted atomic aggregation, thereby forming

crystalline nuclei, resulting in high nucleation density for InO_x films. For InO_x:H film, the doped H, acting as interstitial H and -OH in InO_x:H films, suppressed and decelerated atomic aggregation. During the SPC process, the dramatical rearrangement of film structure also suppressed the formation of crystalline nuclei.

4.4.2 Influences of ramp rate on grain size and Hall mobility of InO_x:H films

As we previously discussed, nucleation density and resulting grain size of the film have a strong impact on Hall mobility. Next, the ramp rate of the SPC process, which was shown in Figure 4. 1, was varied to investigate its effect on grain size and Hall mobility of the InO_x:H film. Figure 4. 8(a)-(d) show EBSD images of the InO_x:H films after annealing at T_A of 250 ℃ with different ramp rate without hold time. Complete crystallization was observed from the films annealed at the ramp rates of 5.8 and 11.5 ℃/min. On the other hand, the films showed a mixed phase of amorphous and crystalline at the ramp rates of 23.0 and 115 ℃/min.

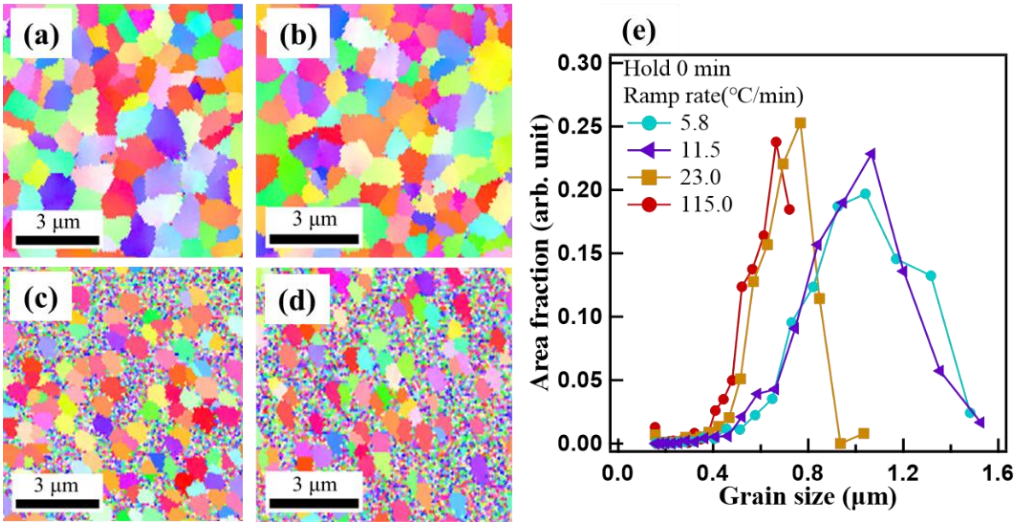

Figure 4. 8 EBSD images of SPC (250 ℃) poly-InO_x:H films without hold time. The ramp rate was set at (a) 5.8 ℃/min, (b) 11.5 ℃/min, (c) 23.0 ℃/min, and (d) 115.0 ℃/min, (e) Area fraction of the grain size of the films (250 ℃, 0 min) with different ramp rate.

Figure 4. 9 shows (a) Hall mobility and (b) carrier density of the InO_x:H films annealed at T_A of 250 ℃ as a function of ramp rate with different hold time. For the InO_x:H films without hold time, Hall mobility decreased and carrier density slightly increased for the films without hold time when the ramp rate increased due to crystalline volume fraction decreased. Hall mobility increased for the films with the ramp rate of more than 11.5 °C/min when the hold time increased from 0 to 3 min. This result indicated that the crystalline volume fraction of the films increased with the hold time owing to a lateral growth from crystalline nuclei as shown in Figure 4. 6. Almost the same Hall mobility (~80 cm^2/Vs) was obtained from all the films after hold time for 3 min irrespective of the ramp rate, suggesting that the ramp rate did not have an impact on the nucleation density and grain size of the film as shown in Table 4. 5.

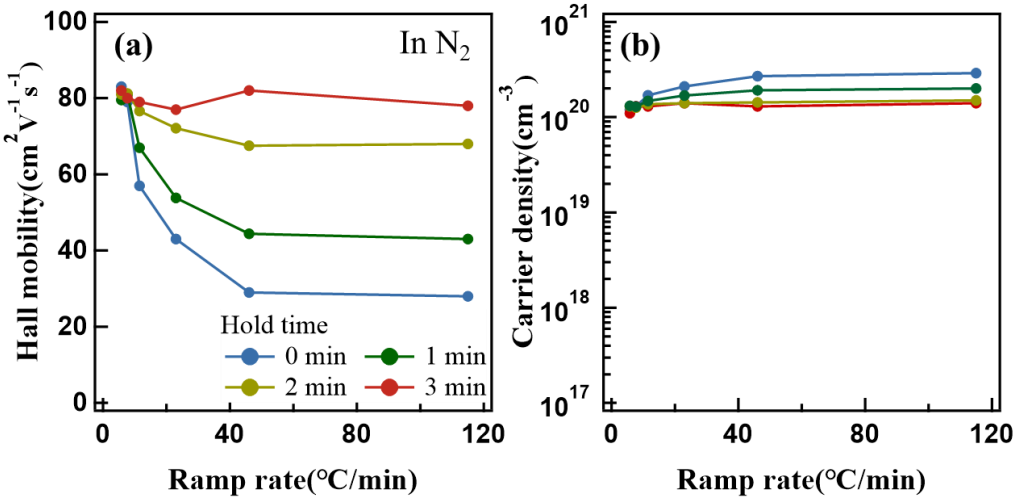

Figure 4. 9 (a) Hall mobility and (b) carrier density of SPC (250 ℃) poly-InO_x:H films as a function of ramp rate with different hold time.

Table 4. 5 Nucleation density of the InO_x:H films as a function of ramp rate without hold time.

Ramp rate(℃/min)	23.0	115.0
Nucleation density (μm^{-2})	1.1	1.1

Figure 4. 10 shows the HAXPES O 1s core spectra of InO_x:H films as a function of ramp rate without hold time. A noticeable difference as a shoulder in the higher binding energy region was observed for the InO_x:H films annealed at 250℃ [hold time 0 min] in N_2 with different ramp rate as shown in Figure 4. 10. Table 4. 6 is a summary of the relative area ratio of the V_O as a function of ramp rate without hold time. Relative area ratio of the V_O increased with the increase of ramp rate, indicating that a large amount of V_O was concentrated in amorphous regions of InO_x:H film, which facilitates the formation of defects due to the disorder of lattice structure. As crystalline volume fraction increased, the relative area ratio of the V_O decreased, corresponding to the decrease of carrier density, as shown in Figure 4. 9.

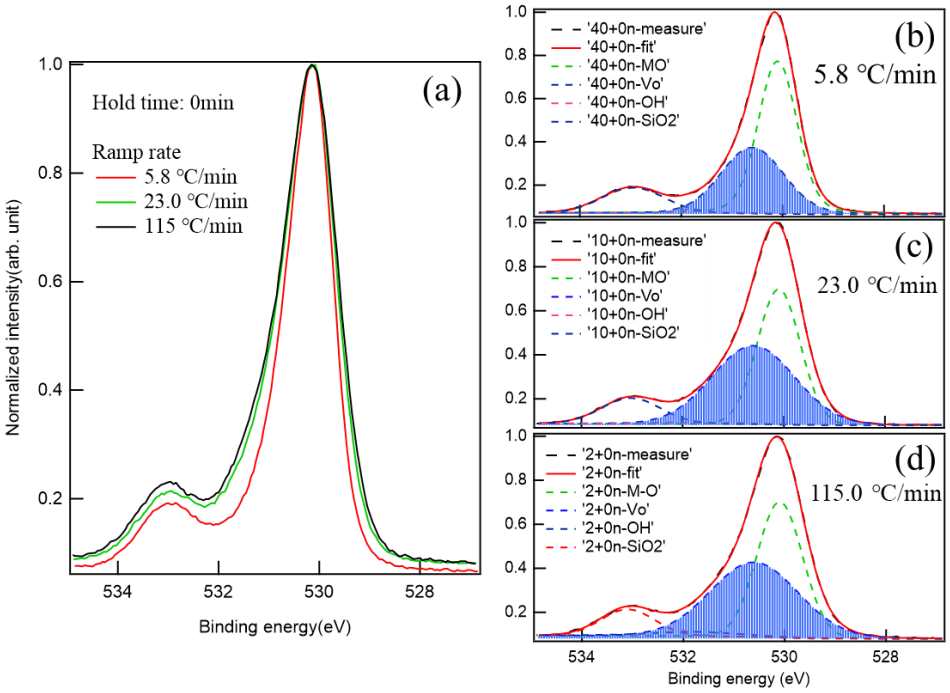

Figure 4. 10 O 1s HAXPES spectra obtained from InO_x:H films as a function of ramp rate without hold time (a) before and (b)-(c) after deconvolution.

Table 4. 6 Relative area ratio of the oxygen vacancies (V_O) of InO_x:H films as a function of ramp rate without hold time.

Ramp rate (℃/min)	5.8	23.0	115.0
V_O (hold 0) (%)	39.7	52.0	49.7

Figure 4. 11 shows (a)-(d) EBSD images and (e) area fraction of grain size of the poly-InO_x:H films after annealing at T_A of 250 ℃ for 3 min with the ramp rate in the range from 5.8 to 115.0 ℃/min. Polycrystalline phase was observed from all the films after annealing at 250 ℃ for 3 min even with different ramp rate. In addition, almost the same grain size was observed from all the films even with different ramp rate as shown in Figure 4. 11(e), indicating that the nucleation density was not changed by the ramp rate. Almost the same grain size, Hall mobility and carrier density could be obtained from the poly-InO_x:H films after annealing at 250 ℃ for 3 min, irrespective of the ramp rate. These results indicated that SPC poly-InO_x:H films have a wide range of processing windows which is also beneficial for the industrial applications.

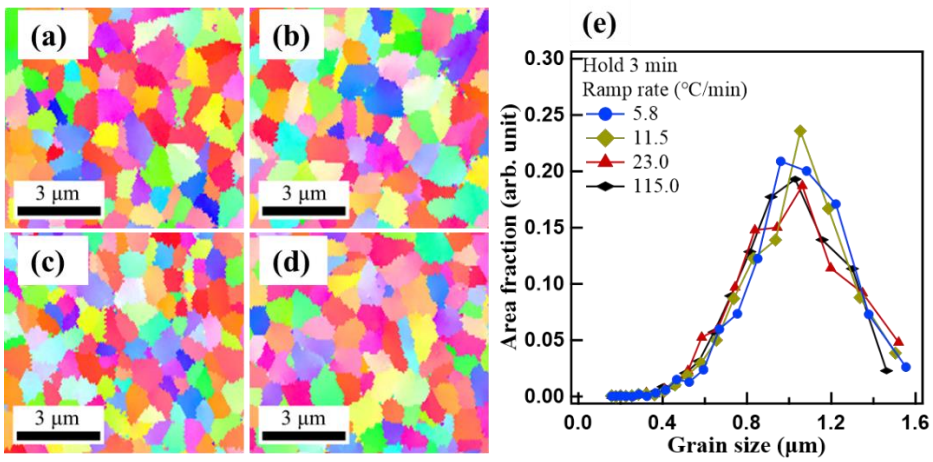

Figure 4. 11 EBSD images of SPC (250 ℃ for 3min) poly-InO_x:H films with the ramp rate of (a) 5.8 ℃/min, (b) 23.0 ℃/min, (c)11.5 ℃/min, and (d) 5.8 ℃/min. (e) area fraction of the grain size of the films (250 ℃, 3 min) with different ramp rate.

Figure 4. 12 shows the HAXPES O 1s core spectra of InO_x:H films as a function of ramp rate with hold time of 3 min. Table 4. 7 summarizes the relative area ratio of the V_O as a function of ramp rate with hold time of 3 min. All the films exhibited almost identical O 1s spectra and ratio of oxygen vacancies after SPC completion irrespective of the ramp rate. As the amorphous regions disappears, the relative area ratio of the V_O decreases to approximately 33.4% for polycrystalline InO_x:H films. It was demonstrated that InO_x:H films exhibit stability against ramp rate after SPC.

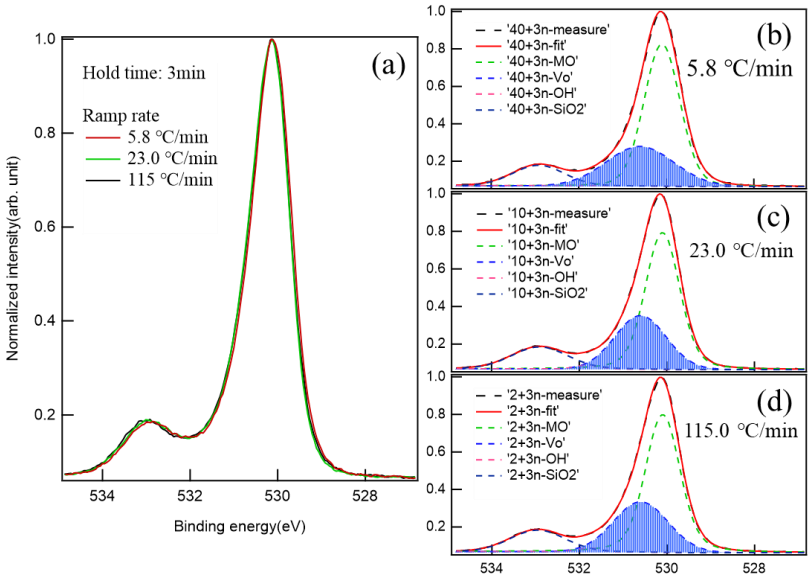

Figure 4. 12 O 1s HAXPES spectra obtained from InO_x:H films as a function of ramp rate with hold time of 3 min (a) before and (b)-(c) after deconvolution.

Table 4. 7 Relative area ratio of the oxygen vacancies (V_O) of InO_x:H films as a function of ramp rate after holding at 250 °C for 3 min.

Ramp rate (°C/min)	5.8	23.0	115.0
V_O (Hold 3 min) (%)	32.5	34.3	33.5

4.5 Conclusion

In this chapter, poly-InO_x and poly-InO_x:H films were formed by rapid SPC. Structure and electrical properties of both the InO_x and InO_x:H films were investigated to clarify the mechanism of phase transition of 30-nm-thick amorphous InO_x:H into poly-InO_x:H films during rapid SPC process. Hall mobility of the InO_x:H films significantly increased to 83 cm^2/Vs after annealing in N_2 at 250 ℃ for 3 min, whereas that of the InO_x films increased to 47 cm^2/Vs due to the difference of the grain size. We found that H_2-doping in InO_x:H films reduced a nucleation density at 250 ℃ from 4.1 to 1.1 μm^{-2}, result in an increase of a grain size and Hall mobility of the poly-InO_x:H films. The crystalline volume fraction in the InO_x:H films annealed at T_A of 250 ℃ without hold time decreased with an increase of the temperature ramp rate. The lateral growth rate from the nucleus was estimated to be 220 nm/min for the InO_x:H film. Thus, an amorphous InO_x:H film could be converted to a poly-InO_x:H film within 3 min owing to a fast lateral growth rate from the nucleus. Hall mobility exhibited ~80 cm^2/Vs for the poly-InO_x:H film with the hold time of more than 3 min. In addition, almost the same grain size, Hall mobility and carrier density could be obtained from the poly-InO_x:H films after annealing at 250 ℃ for 3 min irrespective of the ramp rate. These results indicated that SPC poly-InO_x:H films have a wide range of processing window which is also beneficial for the industrial applications. Low-temperature (250 ℃) and fast lateral growth is a great advantage of the poly-InO_x:H film for enhancing the performance of flexible devices.

Chapter contribution

Based on this chapter the manuscript titled «Nucleation and grain growth in low-temperature rapid solid-phase crystallization of hydrogen-doped indium oxide», Xiaoqian Wang, Yusaku Magari, and Mamoru Furuta, Japanese Journal of Applied Physics, 63, 03SP38 (2024), https://dx.doi.org/10.35848/1347-4065/ad21ba, was published

References

1. Mayer, J.W.; Eriksson, L.; Picraux, S.T.; Davies, J.A. Ion Implantation of Silicon and Germanium at Room Temperature. Analysis by Means of 1.0-MeV Helium Ion Scattering. Can. J. Phys. 1968, 46, 663–673, doi:10.1139/p68-082.
2. Altermatt, P.P.; Heiser, G. Development of a Three-Dimensional Numerical Model of Grain Boundaries in Highly Doped Polycrystalline Silicon and Applications to Solar Cells. Journal of Applied Physics 2002, 91, 4271–4274, doi:10.1063/1.1456962.
3. Wong, J.; Huang, J.L.; Eggleston, B.; Green, M.A.; Kunz, O.; Evans, R.; Keevers, M.; Egan, R.J. Lifetime Limiting Recombination Pathway in Thin-Film Polycrystalline Silicon on Glass Solar Cells. Journal of Applied Physics 2010, 107, doi:10.1063/1.3429206.
4. Lee, W.-K.; Han, S.-M.; Choi, J.; Han, M.-K. The Characteristics of Solid Phase Crystallized (SPC) Polycrystalline Silicon Thin Film Transistors Employing Amorphous Silicon Process. Journal of Non-Crystalline Solids 2008, 354, 2509–2512, doi:10.1016/j.jnoncrysol.2007.09.083.
5. Ebata, K.; Tomai, S.; Tsuruma, Y.; Iitsuka, T.; Matsuzaki, S.; Yano, K. High-Mobility Thin-Film Transistors with Polycrystalline In–Ga–O Channel Fabricated by DC Magnetron Sputtering. Appl. Phys. Express 2012, 5, 011102, doi:10.1143/APEX.5.011102.
6. Rabbi, Md.H.; Bae, J.; Lim, T.; Yamaguchi, K.; Sasaki, D.; Kawashima, E.; Tsuruma, Y.; Jang, J. 81-4: High Performance Coplanar Polycrystalline InGaO TFTs on Polyimide Substrate for Foldable AMOLED Display. SID Symposium Digest of Technical Papers 2023, 54, 1144–1146, doi:10.1002/sdtp.16776.
7. Estrela, P.; Migliorato, P. Chemical and Biological Sensors Using Polycrystalline Silicon TFTs. J. Mater. Chem. 2007, 17, 219–224, doi:10.1039/B612469K.
8. Zhang, C.; Liu, G.; Geng, X.; Wu, K.; Debliquy, M. Metal Oxide Semiconductors with Highly Concentrated Oxygen Vacancies for Gas Sensing Materials: A Review. Sensors and Actuators A: Physical 2020, 309, 112026, doi:10.1016/j.sna.2020.112026.
9. Gurlo, A.; Ivanovskaya, M.; Bârsan, N.; Schweizer-Berberich, M.; Weimar, U.; Göpel, W.; Diéguez, A. Grain Size Control in Nanocrystalline In_2O_3 Semiconductor Gas Sensors. Sens. Actuators B Chem. 1997, 44, 327–333, doi:10.1016/S0925-4005(97)00199-8.

10. Byun, C.W.; Son, S.W.; Lee, Y.W.; Joo, S.K. High Performance Low Temperature Polycrystalline Si Thin-Film Transistors Fabricated by Silicide Seed-Induced Lateral Crystallization. Electron. Mater. Lett. 2012, 8, 251–258, doi:10.1007/s13391-012-2079-x.
11. Jiang, M.; Ahn, D. Seed-Induced Crystallization of Polycrystalline Germanium Thin Films at Low Temperature. Results in Physics 2019, 14, 102502, doi:10.1016/j.rinp.2019.102502.
12. Koida, T.; Kondo, M.; Tsutsumi, K.; Sakaguchi, A.; Suzuki, M.; Fujiwara, H. Hydrogen-Doped In_2O_3 Transparent Conducting Oxide Films Prepared by Solid-Phase Crystallization Method. J. Appl. Phys. 2010, 107, 033514, doi:10.1063/1.3284960.
13. Benvenuto, A.G.; Buitrago, R.H.; Bhaduri, A.; Longeaud, C.; Schmidt, J.A. Characterization of Thin Polycrystalline Silicon Films Deposited on Glass by CVD. Semicond. Sci. Technol. 2012, 27, 125013, doi:10.1088/0268-1242/27/12/125013.
14. Kubo, N.; Kusumoto, N.; Inushima, T.; Yamazaki, S. Characteristics of Polycrystalline-Si Thin Film Transistors Fabricated by Excimer Laser Annealing Method. IEEE Transactions on Electron Devices 1994, 41, 1876–1879, doi:10.1109/16.324604.
15. Chen, R.; Zhou, W.; Zhang, M.; Wong, M.; Kwok, H.-S. High-Performance Polycrystalline Silicon Thin-Film Transistors Based on Metal-Induced Crystallization in an Oxidizing Atmosphere. IEEE Electron Device Letters 2015, 36, 460–462, doi:10.1109/LED.2015.2409858.
16. Mertens, P.W.; Wouters, D.J.; Maes, H.E.; De Veirman, A.; Van Landuyt, J. Role of Impurities in Zone Melting Recrystallization of 10 Mm Thick Polycrystalline Silicon Films. Journal of Applied Physics 1988, 63, 2660–2668, doi:10.1063/1.341006.
17. Iino, H.; Hanna, J. Polycrystalline Organic TFT Fabricated by Solution Process Using Liquid Crystalline Material. Molecular Crystals and Liquid Crystals 2009, 510, 259/[1393]-267/[1401], doi:10.1080/15421400903069582.
18. Macco, B.; Verheijen, M.A.; Black, L.E.; Barcones, B.; Melskens, J.; Kessels, W.M.M. On the Solid Phase Crystallization of In_2O_3:H Transparent Conductive Oxide Films Prepared by Atomic Layer Deposition. J. Appl. Phys. 2016, 120, 085314, doi:10.1063/1.4962008.
19. Berger, A.; Herwegh, M.; Schwarz, J.-O.; Putlitz, B. Quantitative Analysis of

Crystal/Grain Sizes and Their Distributions in 2D and 3D. Journal of Structural Geology 2011, 33, 1751–1763, doi:10.1016/j.jsg.2011.07.002.

20. Lehto, P.; Remes, H.; Saukkonen, T.; Hänninen, H.; Romanoff, J. Influence of Grain Size Distribution on the Hall–Petch Relationship of Welded Structural Steel. Materials Science and Engineering: A 2014, 592, 28–39, doi:10.1016/j.msea.2013.10.094.
21. Takayama, Y.; Furushiro, N.; Tozawa, T.; Kato, H.; Hori, S. A Significant Method for Estimation of the Grain Size of Polycrystalline Materials. Materials Transactions, JIM 1991, 32, 214–221, doi:10.2320/matertrans1989.32.214.
22. Kataoka, T.; Magari, Y.; Makino, H.; Furuta, M. Nondegenerate Polycrystalline Hydrogen-Doped Indium Oxide (InOx:H) Thin Films Formed by Low-Temperature Solid-Phase Crystallization for Thin Film Transistors. Materials 2022, 15, 187, doi:10.3390/ma15010187.
23. Kościelniak, P.; Sitarz, M.; Maciak, E.; Szuber, J. The Effect of Si Substrate Preparation on Surface Morphology and Surface Composition of In_2O_3 Ultrathin Films Deposited by Rheotaxial Growth and Vacuum Oxidation. Applied Surface Science 2012, 258, 8419–8424, doi:10.1016/j.apsusc.2012.03.173.

Chapter 5

Metal-semiconductor transition mechanism of InO_x:H film

5.1 introduction

Oxide semiconductors have been widely researched over the past few decades for use as transparent conductive oxides (TCO) [1], channel layers for flat panel display[2], sensors[3], and flexible devices[4], benefiting from their high electrical properties and low temperature fabrication process. Among them, IGZO (indium gallium zinc oxide) has attracted considerable attention as a channel layer since it was reported by Nomura et al.[5] in 2004. TFTs using IGZO as the channel layer exhibit a field effect mobility of 10 cm^2/Vs. In order to obtain TFTs with higher field effect mobility, we focus on polycrystalline film. Indium oxide has been studied as transparent conducting oxide for decades due to its high Hall mobility[6,7]. In Chapters 3 and 4, InO_x:H films with high Hall mobility were obtained by SPC. The mechanism of SPC was investigated. However, InO_x:H films before and after annealing in N_2 exhibited a high carrier density of 10^{20} cm^{-3}, which is not suitable for TFT application. Figure 5. 1 shows relationship between carrier density and application of (semi)conductive metal oxides as a function of their carrier density. It is essential to control the carrier density ranging from $10^{15} \sim 10^{18}$ cm^{-3} for TFT fabrication. Stable carrier density ensures long-term operational reliability and minimizes device degradation.

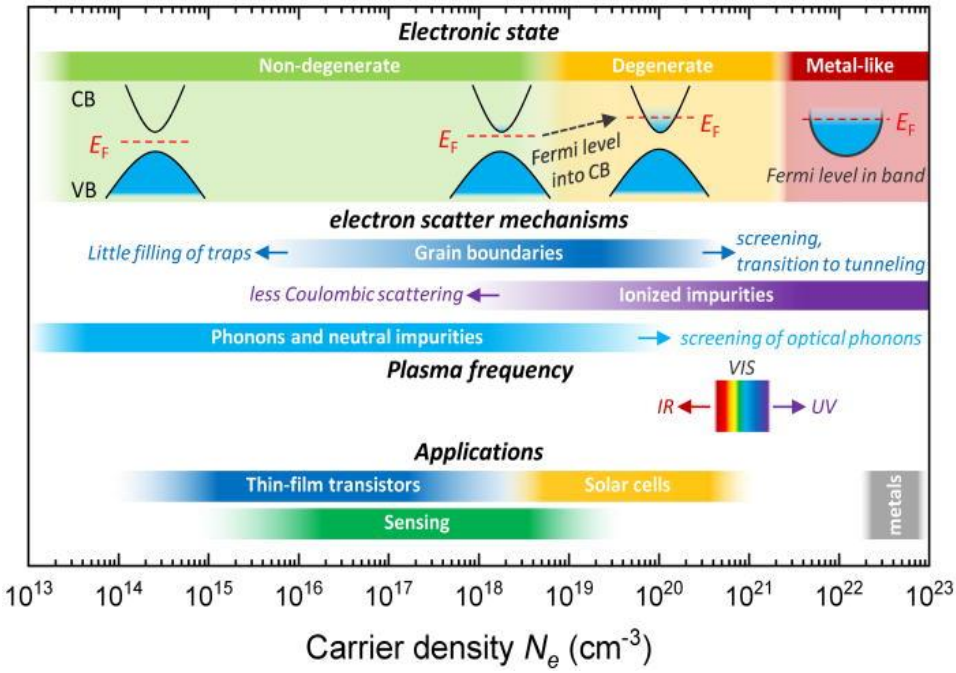

Figure 5. 1 Schematic of various aspects of (semi)conductive metal oxides as a function of their carrier density.[8]

M. Nistor et al. obtained nondegenerate undoped In_2O_3 films by pulsed electron beam deposition at a deposition temperature of 500 °C.[9] There are some issues with this fabrication. The obtaining of nondegenerate In_2O_3 films required high temperature and complex equipment. The carrier density of In_2O_3 films was very sensitive to oxygen gas pressure during deposition. Nondegenerate In_2O_3 films require improvement in stability at a wide range of deposition condition parameters, controlling carrier density in a wide range, using simple methods.

In oxide semiconductors, carrier density control methods primarily include doping, thermal annealing, controlling the atmosphere during deposition, and ion implantation. The carrier density controlling method is summarized in Table 5. 1. Among these methods, doping is widely used to change electrical and structural properties, which can achieve a wide range of carrier density films[10]. The advantages of doping are wide material

selection and carrier density adjustment range. Annealing is usually used to decrease carrier density. Annealing changes the defect structure (such as oxygen vacancies and interstitial impurities) inside the material through thermal treatment, thereby controlling the carrier density.

Table 5. 1 Carrier density controlling method for oxide semiconductor.

Method	Mechanism	Range of carrier density (cm^{-3})	Reference
Doping	Changing electronic structure	$10^{15} \sim 10^{21}$	[11–13]
Thermal annealing	Repair or generate defects at high temperature	$10^{15} \sim 10^{19}$	[14–16]
Control atmosphere during deposition	Repair or generate defects	$10^{17} \sim 10^{20}$	[17]
Hydrogen treatment	Passivate defects	$10^{17} \sim 10^{19}$	[18,19]
Ion implantation	Supply donor element	$10^{15} \sim 10^{21}$	[20–22]

As a representative semiconductor material, the carrier density of IGZO can be controlled within the range of ~10^{13} to ~10^{20} cm^{-3} by varying the oxygen pressure and annealing during the deposition and thermal treatment process, respectively.[23,24] Indium oxide shows a high carrier density of 10^{18} cm^{-3} due to the excess oxygen vacancy. In the research of semiconductors and applications, accurate control for carrier density is crucial for achieving high performance and stable operation of devices. The electrical properties of oxide semiconductors are determined by intrinsic band structure, impurities, and defects, which can be controlled by deposition conditions and post-deposition treatment.

Kataoka et al.[25] have reported that nondegenerate poly-InO_x:H thin films were successfully prepared by SPC. Figure 5. 2 shows carrier density of as-deposited and 250℃ annealed poly-InO_x and poly-InO_x:H films as a function of R[H_2] during film deposition. Carrier density slightly increased with hydrogen dopant. After annealing at N_2 for 60 min, all the films show almost the same carrier density of ~10^{20} cm^{-3}, regardless of R[H_2]. On the other hand, after annealing at 250 °C in air, poly-InO_x film remained in a degenerate state, while poly-InO_x:H films exhibited a nondegenerate state.[26]

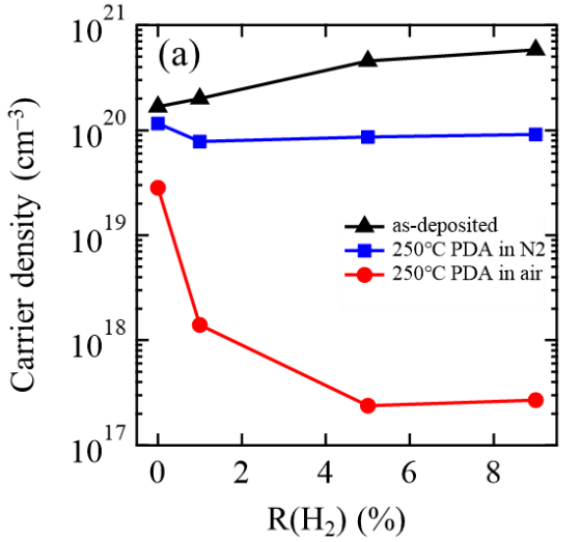

Figure 5. 2 Carrier density of InO_x (R[H_2] = 0) and InO_x:H (R[H_2] = 1, 5, 9%) films before (as-deposited) and after 250 ℃ PDA (in both N_2 and air) as a function of R[H_2].[25]

5.2 InO_x and InO_x:H films deposition conditions

In order to investigate the mechanism of carrier density reduction, 50-nm-thick InO_x and InO_x:H films were deposited by radio frequency magnetron sputtering from a ceramic In_2O_3 target at room temperature on glass or SiO_2 (100 nm)/Si substrates. Mixed gases of Ar, O_2, and H_2 were used to deposit InO_x and InO_x:H films. The O_2 and H_2 gas flow ratios

ranged from 2% to 4% and 0 to 5%, respectively. Since it is known that hydrogen generates carrier, which has an effect on the electrical properties of InO_x films, in order to minimize the influence of water from the atmosphere and residual H content after deposition, the main chamber was pumped out to a back pressure below 1×10^{-4} Pa. The RF power and deposition pressure were 200 W and 0.4 Pa, respectively. Deposition parameters of InO_x and InO_x:H films are summarized in Table 5. 2. Then, the films were annealed in N_2 and air by RTA at temperatures ranging from 100 to 400 ℃, as shown in Table 5. 3.

Table 5. 2 Deposition parameters of the H-doped InO_x and InO_x:H films.

Target	In_2O_3
Substrate	EAGLE XG Glass SiO_2 (100 nm)/Si
Film thickness	50 nm
Deposition time	3′4″
Back pressure	$< 1\times10^{-4}$for InO_x $< 3\times10^{-4}$for InO_x:H
Deposi+tion pressure	0.4 Pa
RF power	200 W
Total gad flow ($Ar+O_2+H_2$)	10 sccm
Deposition temperature (°C)	RT
R[O_2] = O_2 / ($Ar+O_2+H_2$) (%)	2 ~ 4%
R[H2] = H2 / ($Ar+O_2+H_2$) (%)	0, 5%

Table 5. 3 Annealing parameters of the H-doped InO_x and InO_x:H films.

Annealing temperature	150 ℃ ~ 400 ℃
Annealing time	0 ~ 60 min
Annealing Ramp rate	115 ℃/min
Annealing ambient gas	N_2, Air

5.3 Mechanism of carrier density reduction of InO_x:H film

5.3.1 Carrier density reduction by decrease of ionized impurities

Figure 5. 3 shows Hall mobility and carrier density of 50-nm-thick InO_x ($R[H_2]$ = 0%) and InO_x:H ($R[H_2]$ = 5%) films as a function of annealing temperature in N_2. As reported in Chapter 3, Hall mobility increased with the occurrence of crystallization for InO_x and InO_x:H films at 200 ℃. Carrier density of as-deposited films increased with the doping of H from 1.8×10^{20} cm^{-3} for InO_x film to 4.5×10^{20} cm^{-3} for InO_x:H film due to the ionized impurities. After annealing in N_2, carrier density of InO_x film almost did not change as the annealing temperature increased. On the other hand, carrier density of InO_x:H film started to decrease at the temperature of 200 ℃ and further reduced to 2.9×10^{18} cm^{-3} as the temperature increased to 350 ℃.

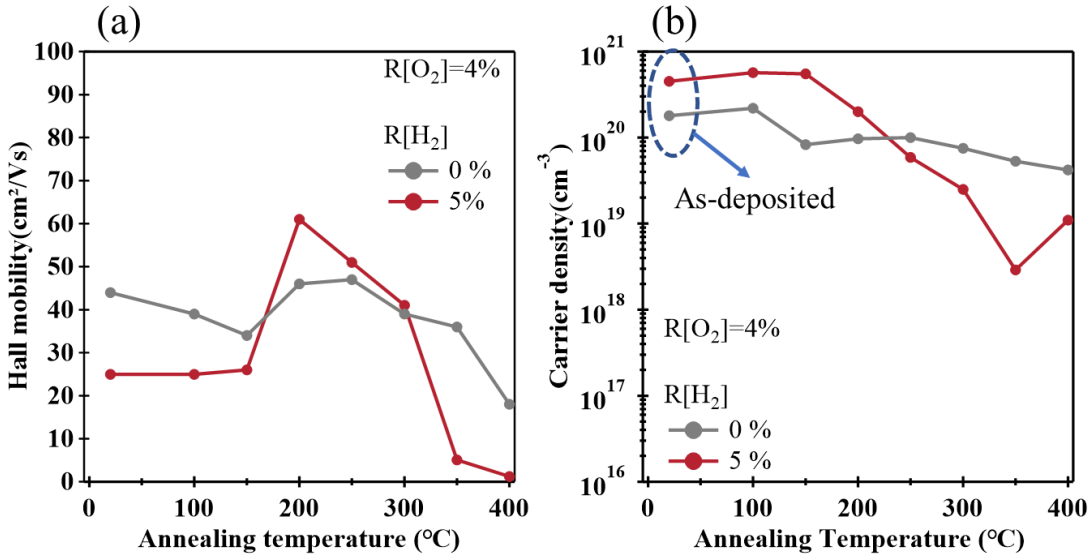

Figure 5. 3 (a) Hall mobility and (b) carrier density of InO_x ($R[H_2]$ = 0%) and InO_x:H ($R[H_2]$ = 5%) films as a function of annealing temperature (in N_2). $R[O_2]$ was set at 4%. Ramp and hold time are 2 and 60 min, respectively.

Figure 5. 4 shows SEM surface views of InO_x ($R[H_2]$ = 0%) and InO_x:H [$R[H_2]$ = 5%]

films before and after annealing in N_2. No significant change was observed in InO_x films before and after annealing. Whereas SPC occurred for InO_x:H films during annealing at 250 ℃, causing drastic rearrangement of crystal and obviously large grain size. It is considered that the obvious phase transition due to SPC is one of the causes of carrier density reduction.

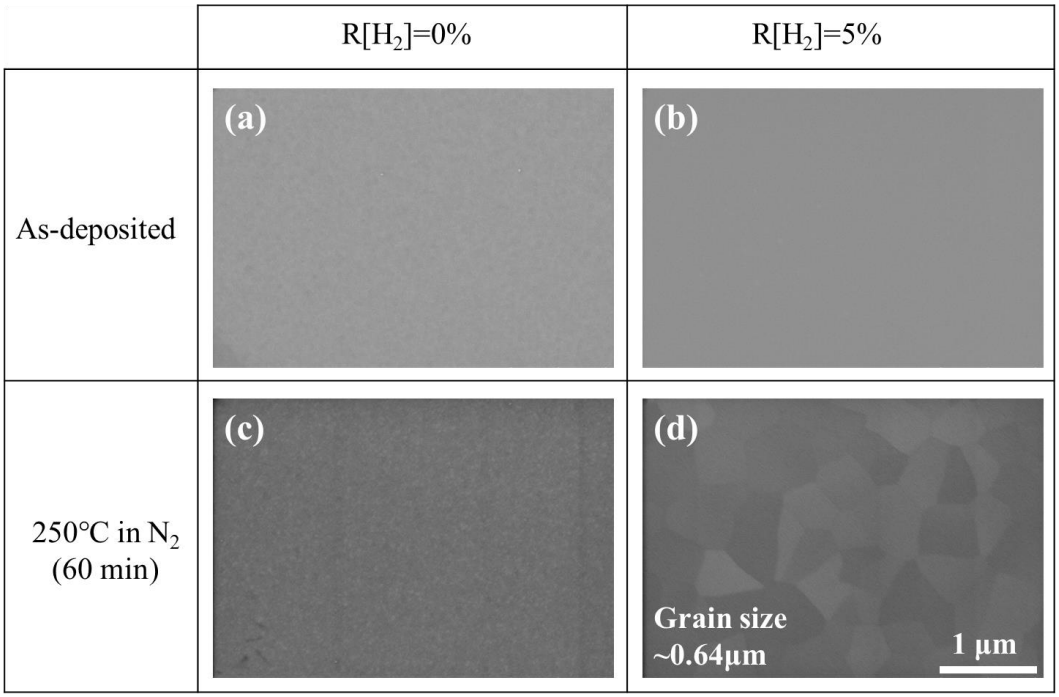

Figure 5. 4 SEM surface views of InO_x films ($R[H_2]$ = 0%): (a) as-deposited, (b) annealed in N_2 at 250 ℃ (60 min). InO_x:H films ($R[H_2]$ = 5%): (c) as-deposited, (d) annealed in N_2 at 250 ℃ (60 min).

Thermal desorption spectroscopy (TDS) analysis was performed in order to investigate the change in InO_x and InO_x:H films during SPC, as shown in Figure 5. 5. No desorption of H_2 was observed during the whole measurement, as shown in Figure 5. 5(a). There is a small desorption peak of H_2O at ~100 ℃ for InO_x film. In contrast, an obvious desorption peak of H_2O was observed at below 200 ℃. It is indicated that the ionized H

was desorbed as H_2O during SPC, causing the decrease in carrier density. It is considered that ionized H and V_O act as shallow donors, which were desorbed or passivated at low temperature. On the other hand, -OH was located at a deep level state, which can be desorbed at a high temperature of above 500 ℃, as shown in Figure 5. 5(b).

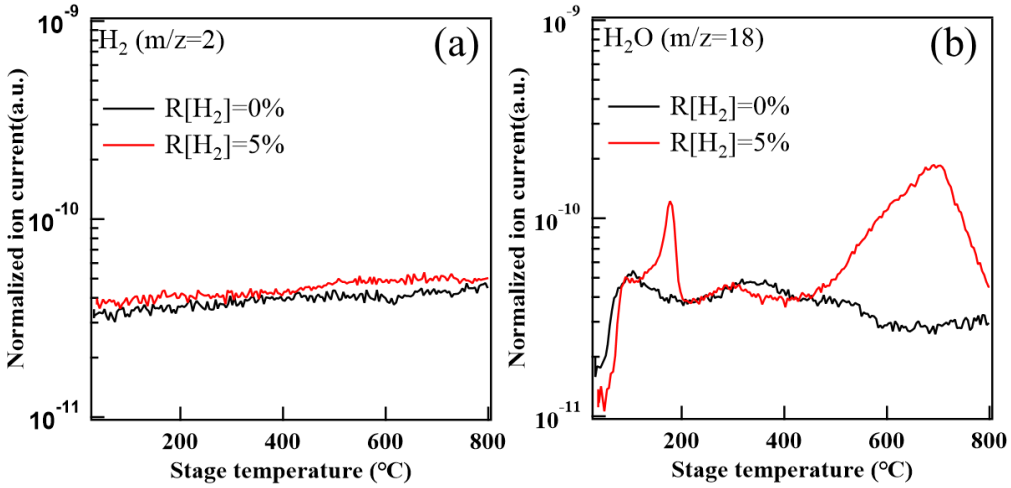

Figure 5. 5 TDS analysis of the 50-nm-thick as-deposited InO_x (R[H_2] = 0%) and InO_x:H (R[H_2] = 5%): films (a) m/z = 2 (H_2); (b) m/z = 18 (H_2O).

5.3.2 Carrier density reduction by passivation of oxygen vacancy

In order to investigate the role of H in films and clarify the change that occurred during SPC, chemical bonding states and subgap states of the InO_x and InO_x:H films were measured by HAXPES. Figure 5. 6 shows O 1s HAXPES spectra obtained from InO_x and InO_x:H films before and after annealing in N_2. Relative area ratios of metal-oxygen (M-O), oxygen vacancies (V_O), and oxygen-hydrogen (-OH) in the InO_x and InO_x:H films before and after annealing in N_2 are summarized in Table 5. 4. Relative area ratio of V_O increased from 10.35% for as-deposited InO_x films to 37.01% for as-deposited InO_x:H films with the introduction of H, indicating that H doping promoted the formation of V_O. R[V_O] of InO_x films almost did not change after annealing in N_2. Whereas R[V_O] of

InO_x:H films significantly decreased from 37.10% to 9.70%. It is considered that V_O provided a portion of the carrier density. Then, V_O was passivated due to rearrangement of crystal by SPC, causing the reduction of carrier density.

A low relative area ratio of -OH (2.13%) was observed in as-deposited InO_x films due to unintentional doping of H_2O. As H is intentionally introduced, the relative area ratio of -OH increased to 5.93% for as-deposited InO_x:H films. Relative area ratio of -OH of both the films slightly decreased after annealing. It is considered that -OH did not play an active role in carrier density reduction during annealing.

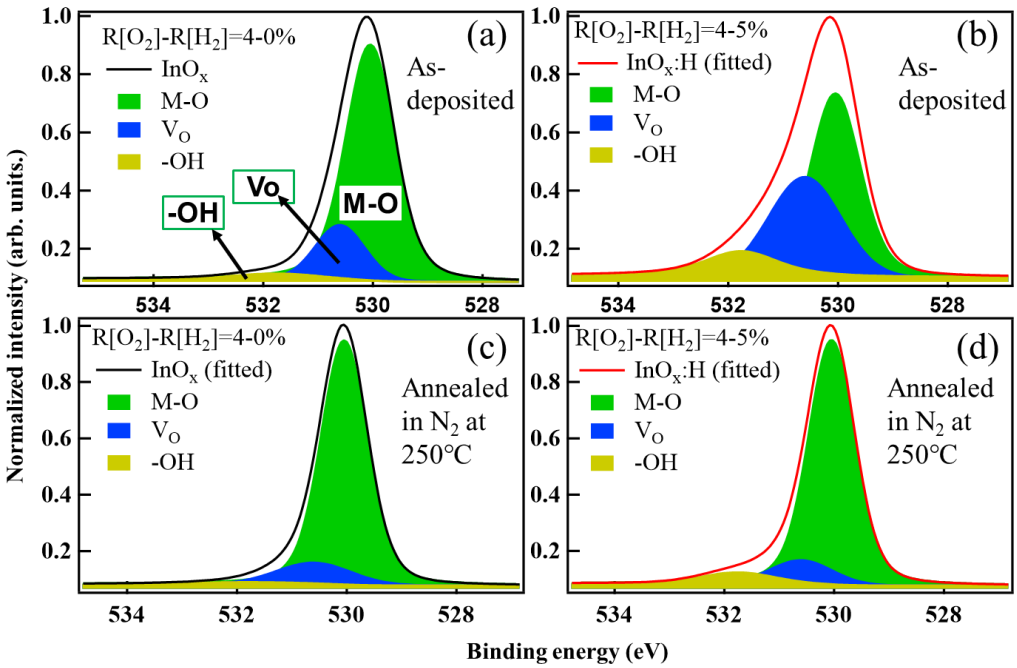

Figure 5. 6 O 1s HAXPES spectra obtained from as-deposited (a) InO_x ($R[H_2]$ = 0%) film and (b) InO_x:H ($R[H_2]$ = 5%) films; polycrystalline (c) InO_x films and (d) InO_x:H films after deconvolution.

Table 5. 4 Relative area ratio of the metal-oxygen (M-O), oxygen vacancies (V_O), and oxygen-hydrogen (-OH) in the InO_x and InO_x:H films before and after annealing in N_2 for 60 min after deconvolution of O 1s spectra.

	R[H_2] (%)	R[M-O] (%)	R[Vo] (%)	R[-OH] (%)
As-deposited	0	87.52	10.35	2.13
	5	57.05	37.01	5.93
Annealed in N_2	0	87.69	11.04	1.27
	5	85.06	9.70	5.24

Figure 5. 7 shows the valence band configuration from E_F of the (a) as-deposited and (b) annealed films, respectively. As can be seen in Figure 5. 7(a), near E_F states of as-deposited InO_x:H film was slightly increased as compared with the as-deposited conventional InO_x film. Then, near E_F states of InO_x:H film significantly decreased. Whereas that of InO_x film almost did not change. It turned out that the change in near E_F states reflects the change in V_O.

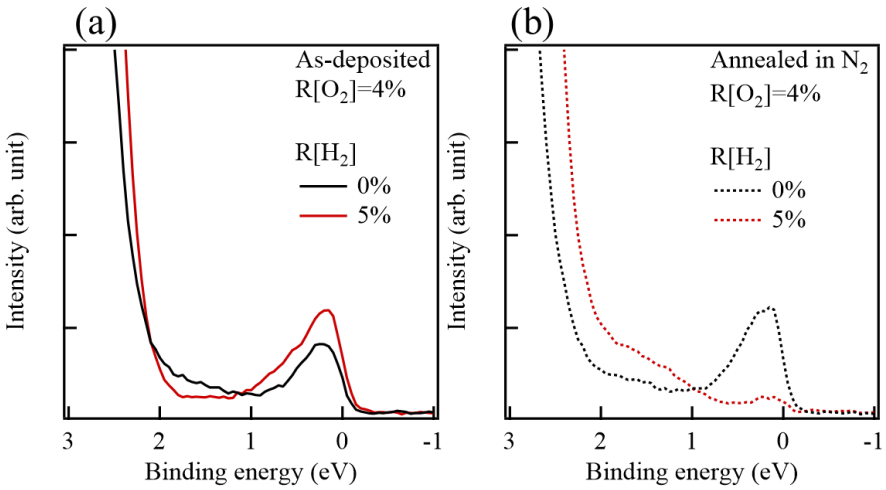

Figure 5. 7 HAXPES spectra around band gap of the InO_x (R[H_2] = 0%) and InO_x:H (R[H_2] = 5%) films deposited at fixed R[O_2] = 4%: (a) as-deposited; (b) after annealing for 60 min in N_2 at 250 ℃.

5.3.3 Effect of annealing atmosphere gas on carrier density reduction

Figure 5. 8 shows (a) Hall mobility and (b) carrier density of 50-nm-thick InO_x ($R[H_2]$ = 0) and InO_x:H ($R[H_2]$ = 5%) films as a function of annealing temperature in air. Nondegenerate InO_x films were obtained by annealing in air at above 300 ℃, causing a significant decrease in carrier density from 1.8×10^{20} cm^{-3} to 5.1×10^{17} cm^{-3}. In contrast, nondegenerate InO_x:H films were obtained at a lower temperature of 200 ℃, causing a wider reduction in carrier density, from 4.5×10^{20} cm^{-3} to 6.3×10^{16} cm^{-3}. In addition to the reduction in carrier concentration resulting from crystal rearrangement due to SPC, the annealing atmosphere is also a factor influencing the decrease in carrier concentration.

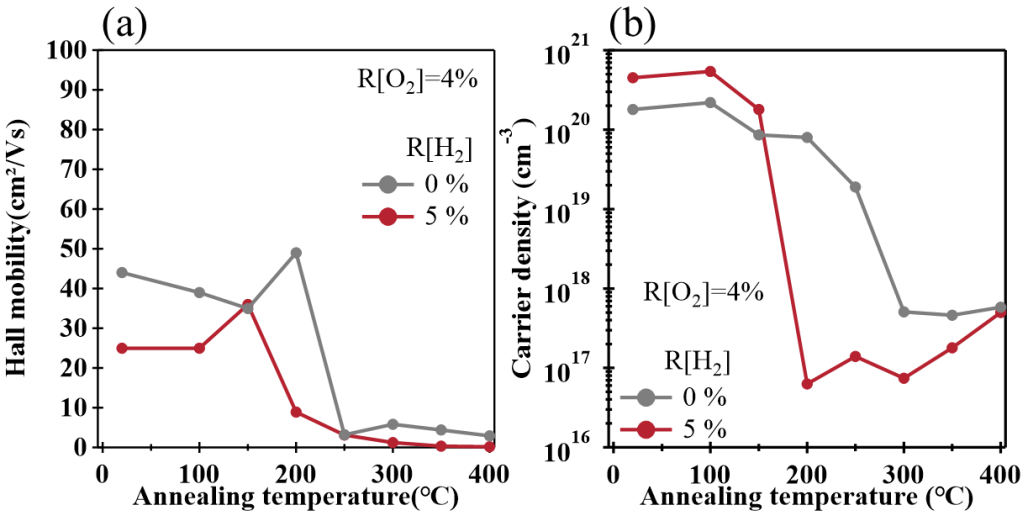

Figure 5. 8 (a) Hall mobility and (b) carrier density of InO_x ($R[H_2]$ = 0%) and InO_x:H ($R[H_2]$ = 5%) films as a function of annealing temperature (in air). $R[O_2]$ was set at 4%. Ramp and hold time are 2 and 60 min, respectively.

Figure 5. 9 shows TDS analysis of InO_x and InO_x:H films before and after annealing in N_2 and air. No desorption peak of H_2 was observed during the whole measurement for as-deposited and annealed films, as shown in Figure 5. 9(a) and (c). Compared to films after

annealing, an obvious H_2O desorption peak was observed at a temperature below 200 ℃ for as-deposited films. Interstitial H, substitutional H, and weakly bond O were desorbed as H_2O. However, as-deposited and annealed samples exhibited the same intensity at temperature above 500 ℃, indicating that annealing at 250 ℃ did not affect -OH, which formats deep localized states, as shown in Figure 5. 9(b) and (d).

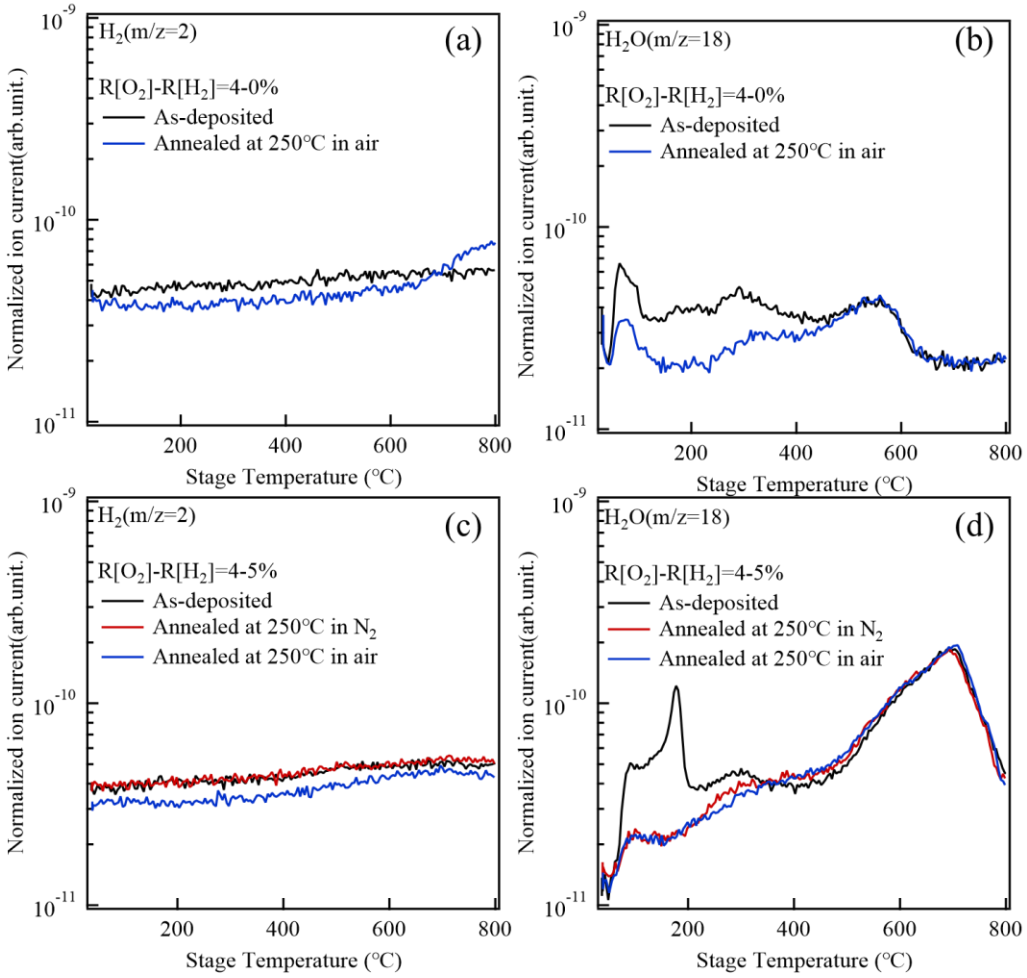

Figure 5. 9 TDS analysis of the 50-nm-thick InO_x films: (a) m/z = 2 (H_2) and (b) m/z = 18 (H_2O); InO_x:H films: (c) m/z = 2 (H_2) and (d) m/z = 18 (H_2O).

Figure 5. 10 shows SEM surface views of InO_x ($R[H_2] = 0$) and InO_x:H [$R[H_2] = 5\%$] films before and after annealing in air at 250 ℃. No significant change was observed in

InO_x films before and after annealing in N_2 and air. Large grain due to SPC was observed. However, polycrystalline films exhibited almost the same grain size of ~0.65μm, irrespective of the annealing atmosphere.

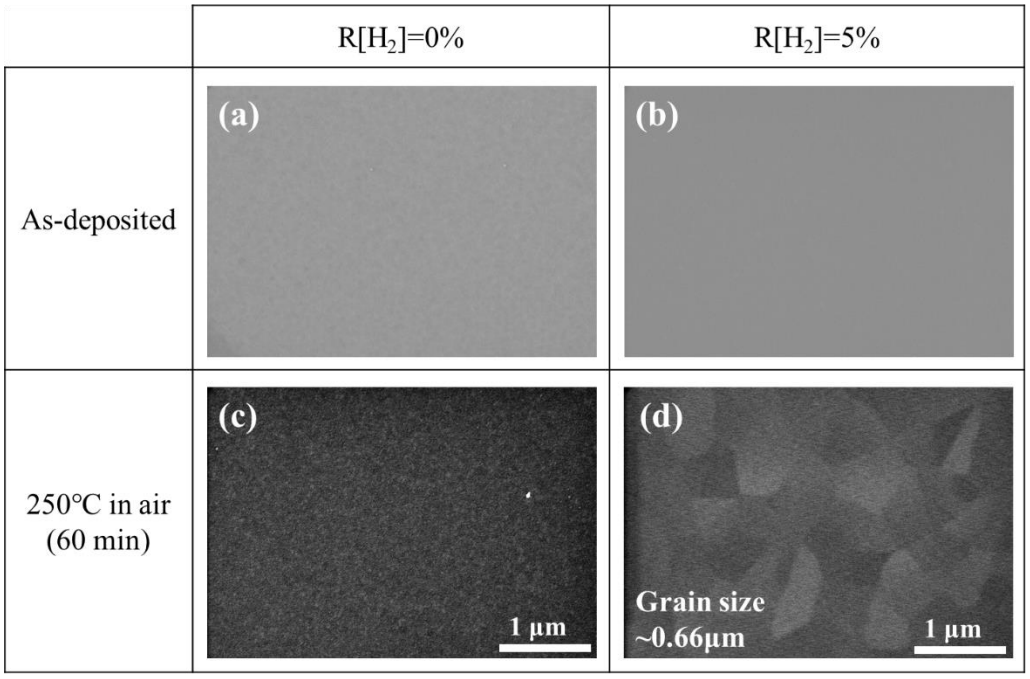

Figure 5. 10 SEM surface views of InO_x films ($R[H_2]$ = 0%): (a) as-deposited, (c) annealed in air at 250 ℃ (60 min); InO_x:H films ($R[H_2]$ = 5%): (b) as-deposited, (d) annealed in air at 250 ℃ (60 min).

As described above, crystallization is not the cause of metal-semiconductor transition. Next, chemical bonding states and subgap states of the InO_x and InO_x:H films were investigated. Figure 5. 11 shows O 1s HAXPES spectra obtained from InO_x and InO_x:H films before and after annealing in air. Relative area ratios of M-O, V_O, and -OH in the InO_x and InO_x:H films before and after annealing in air are summarized in Table 5. 5. Relative area ratio of V_O and -OH of InO_x films slightly decreased from 10.35% to 6.00% and 2.13% to 0.92%, respectively. The change of chemical bonds in InO_x films can not result in an obvious decrease. Relative area ratio of V_O of InO_x:H films shows a more

substantial decrease compared to films annealed in N_2, decreasing from 37.10% to 3.23%. The oxygen in annealing atmosphere further passivated the V_O, causing a further decrease in carrier density. Relative area ratio of -OH of InO_x:H films slightly decreased from 5.93% to 4.63%. However, the relative area ratio of -OH of InO_x:H films is higher than that of InO_x films after annealing. It is considered that -OH suppressed the formation of carrier density.

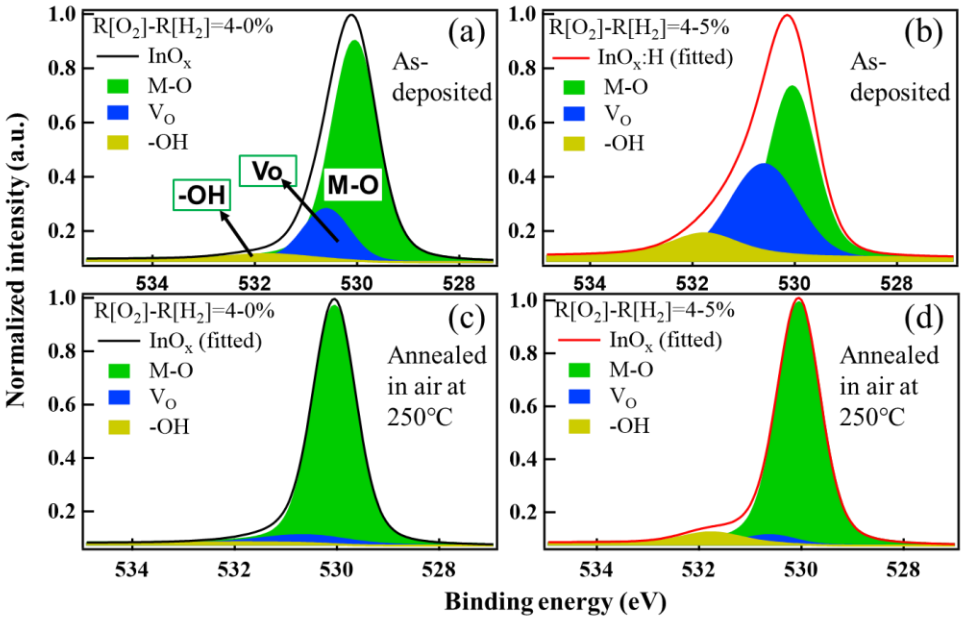

Figure 5. 11 O 1s HAXPES spectra obtained from as-deposited (a) InO_x ($R[H_2]$ = 0%) film and (b) InO_x:H ($R[H_2]$ = 5%) films; polycrystalline (c) InO_x films and (d) InO_x:H films annealed in air after deconvolution.

Table 5. 5 Relative area ratio of the M-O, V_O, and -OH in the InO_x and InO_x:H films before and after annealing in air for 60 min after deconvolution of O 1s spectra.

	R[H_2] (%)	R[M-O] (%)	R[Vo] (%)	R[-OH] (%)
As-deposited	0	87.52	10.35	2.13
	5	57.05	37.01	5.93
Annealed in air	0	93.07	6.00	0.92
	5	92.14	3.23	4.63

Figure 5. 12 shows the valence band configuration from E_F of the (a) as-deposited and (b) annealed (in air) InO_x and InO_x:H films, respectively. High near E_F states were observed for InO_x film even after annealing in air with almost no change in carrier density. Compared to InO_x films, near E_F states of InO_x:H film further decreased, which corresponded to the decrease in carrier density.

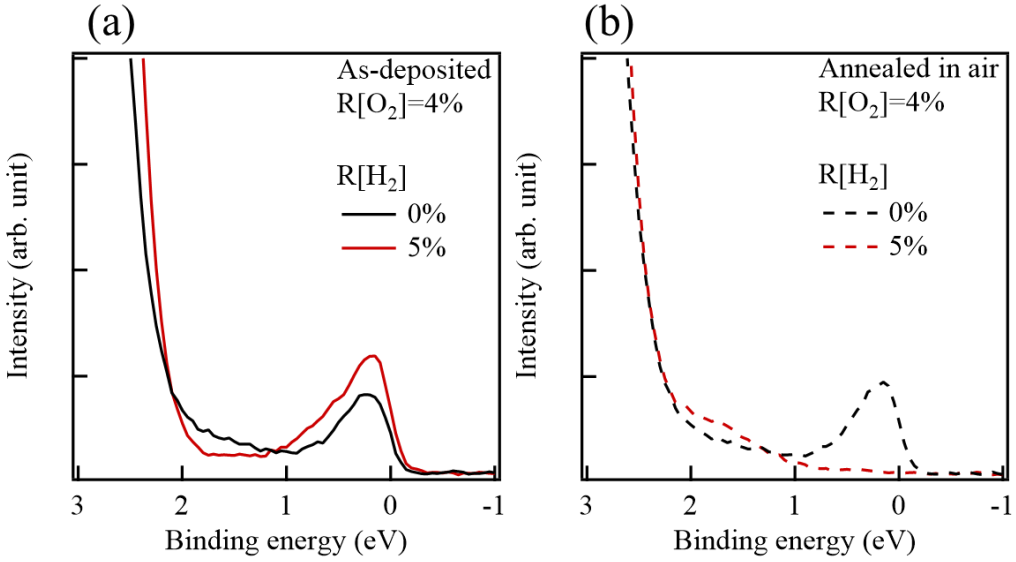

Figure 5. 12 HAXPES spectra around band gap of the InO_x (R[H_2] = 0%) and InO_x:H (R[H_2] = 5%) films deposited at fixed R[O_2] = 4%: (a) as-deposited; (b) after annealing for 60 min in air at 250 ℃.

Next, the change in HAXPES spectra around band gap during annealing in N_2 and air for InO_x and InO_x:H films was investigated in detail. Figure 5. 13 shows HAXPES spectra around band gap of the (a) InO_x ($R[H_2]$ = 0%) and (b) InO_x:H ($R[H_2]$ = 5%) films before and after annealing for 60 min in N_2 and air at 250 ℃. High near E_F states and the same near-VBM states were observed before and after annealing in N_2 and air. In contrast, a significant decrease in near E_F states was observed after annealing. An obvious increase in near-VBM states after annealing. It is considered that the extremely low relative area ratio of the V_O and the suppression of carriers by -OH jointly result in the formation of nondegenerate InO_x:H films.

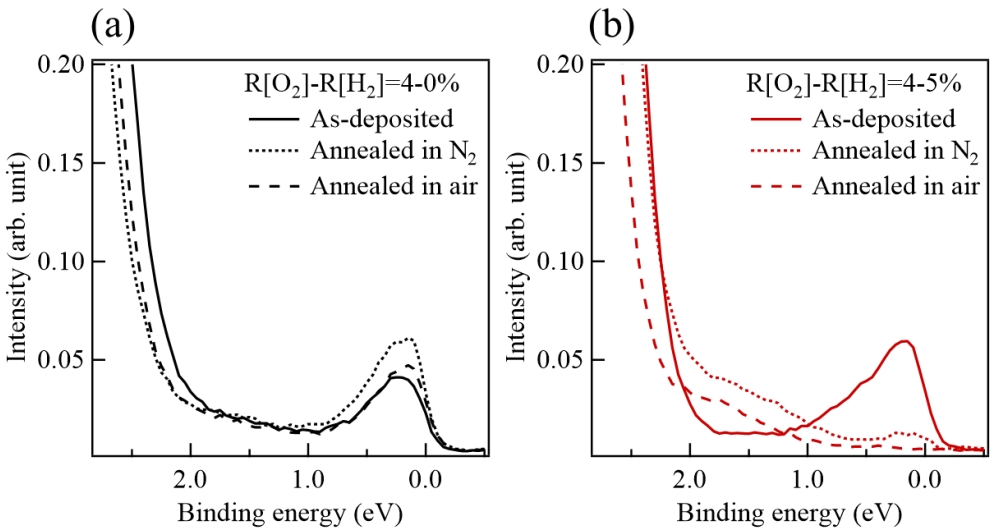

Figure 5. 13 HAXPES spectra around band gap of the (a) InO_x ($R[H_2]$ = 0%) and (b) InO_x:H ($R[H_2]$ = 5%) films before and after annealing for 60 min in N_2 and air at 250 ℃.

5.4 Effect of intrinsic oxygen on carrier density reduction

5.4.1 The effect of intrinsic oxygen on InO_x:H films before and after annealing in N_2

Figure 5. 14 shows the carrier density of InO_x:H films as a function of annealing temperature in N_2. As-deposited InO_x:H films exhibited almost the same carrier density

of 5 $\times 10^{20}$ cm^{-3} with R[O_2] ranging from 2 ~ 4%. The R[O_2] during deposition did not show an obvious effect on carrier density. Carrier density of all the InO_x:H films decreased with annealing temperature higher than 200°C. InO_x:H films with R[O_2] of 2% showed higher carrier density than films with R[O_2] of 3 and 4% after SPC in N_2. Intrinsic oxygen, determined by the oxygen flow ratio during deposition, reduced carrier density after SPC. However, carrier density of InO_x:H films showed a slight difference with different R[O_2]. Next, the SEM surface views were investigated.

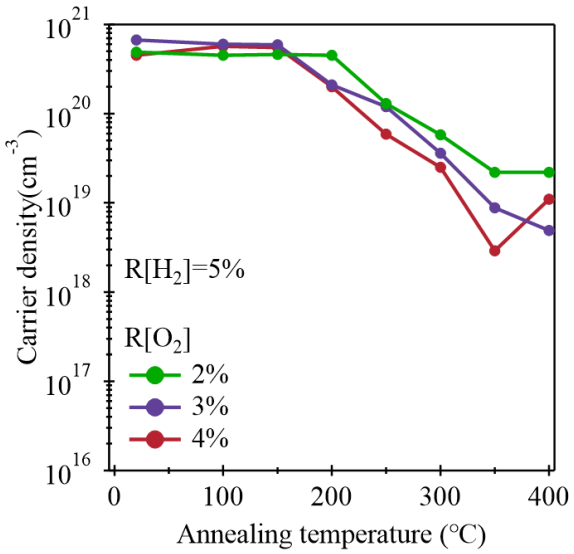

Figure 5. 14 Carrier density of InO_x:H (R[O_2] = 2 ~ 4%) films as a function of annealing temperature (in N_2). R[H_2] was set at 5%. Ramp and hold time are 2 and 60 min, respectively.

Figure 5. 15 shows SEM surface views of InO_x:H films with R[O_2] ranging from 2% to 4%. SPC occurred for all the films with hydrogen doping, causing a slight decrease of carrier density. Large grains were observed for all the films, irrespective of R[O_2]. No significant correlation was observed between grain size and carrier density of InO_x:H films.

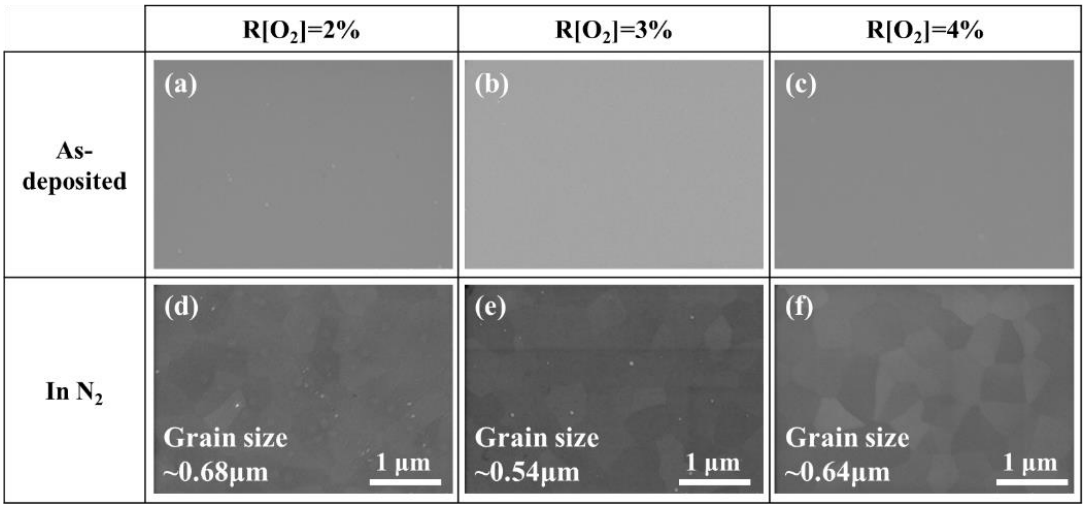

Figure 5. 15 SEM surface views of as-deposited InO_x:H films with R[O_2] of (a) 2%, (b) 3% and (c) 4%; annealed InO_x:H films with R[O_2] of (a) 2%, (b) 3% and (c) 4% (in N_2). Annealing time and temperature are 60 min and 250 ℃, respectively.

Figure 5. 16 shows O 1s HAXPES spectra obtained from InO_x:H films with R[O_2] ranging from 2 ~ 4% before and after annealing in N_2 at 250 ℃. Relative area ratios of M-O, V_O, and -OH in the InO_x:H films before and after annealing in N_2 are summarized in Table 5. 6. As-deposited InO_x:H films with different R[O_2] show almost the same chemical bonding states, corresponding to the same carrier density. In contrast, relative area ratios of M-O increased, and that of V_O and -OH decreased obviously with the increase of R[O_2] after annealing in N_2. It is discussed above that the near E_F states are related to the carrier density of InO_x:H films after annealing. Next, the HAXPES spectra around band gap was investigated.

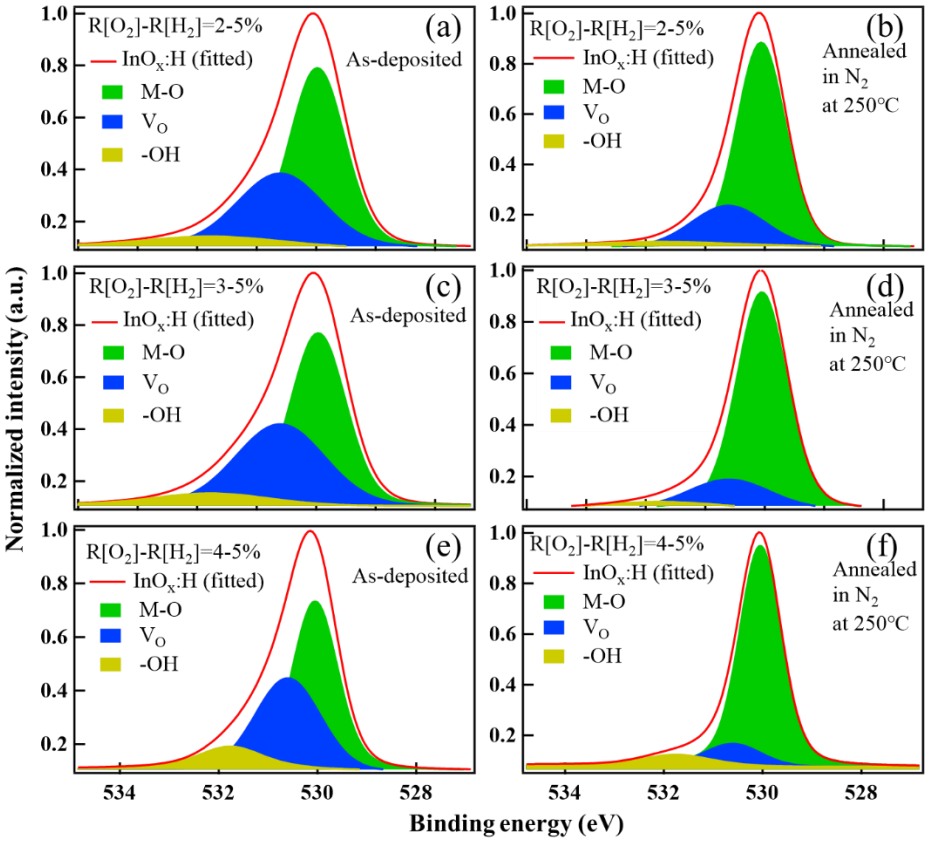

Figure 5. 16 O 1s HAXPES spectra obtained from as-deposited InO_x:H films with R[O_2] of (a) 2%, (c) 3%, and (e) 4%; InO_x:H films annealed in N_2 at 250 ℃ with R[O_2] of (a) 2%, (c) 3%, and (e) 4%.

Table 5. 6 Relative area ratio of the M-O, V_O, and -OH in the InO_x:H films with R[O_2] ranging from 2~4% before and after annealing in N_2 for 60 min after deconvolution of O 1s spectra.

	R[H_2] (%)	R[M-O] (%)	R[Vo] (%)	R[-OH] (%)
As-deposited	2	57.87	35.56	6.57
	3	54.28	38.88	6.85
	4	57.05	37.01	5.93
Annealed in N_2	2	73.46	21.13	5.40
	3	79.17	15.96	4.87
	4	85.06	9.70	5.24

Figure 5. 17 shows the valence band configuration from E_F of the InO_x:H films with $R[O_2]$ ranging from 2 ~ 4% after annealing for 60 min in N_2 at 250 ℃. Polycrystalline InO_x:H films with $R[O_2]$ of 2% show higher near E_F states and near-VBM states than films with $R[O_2]$ of 3 and 4%. It is indicated that the intrinsic oxygen decreased near E_F states and near-VBM states of polycrystalline films, resulting in the decrease of carrier density. However, the increase of $R[O_2]$ caused a slight change in carrier density of InO_x:H films. Next, a further reduction of carrier density was achieved.

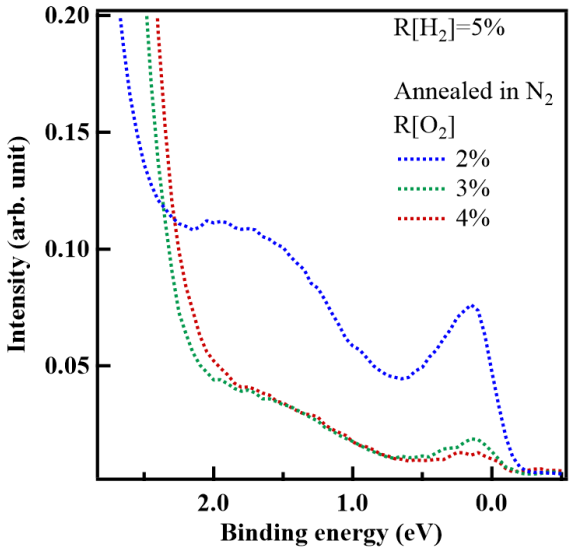

Figure 5. 17 HAXPES spectra around the band gap of the InO_x:H films with $R[O_2]$ ranging from 2 ~ 4% after annealing for 60 min in N_2 at 250 ℃. $R[H_2]$ was fixed at 4%.

5.4.2 Synergistic effect of intrinsic oxygen and annealing ambient oxygen on carrier reduction

Figure 5. 18 shows the carrier density of InO_x:H films as a function of annealing temperature in air. The metal-semiconductor transition temperature decreased with the increase of $R[O_2]$. Carrier density of InO_x:H films ($R[O_2]$ = 4%) decreased from 4.5×10^{20} cm^{-3} to 6.3×10^{16} cm^{-3} at a lower temperature of 200 ℃. In contrast, carrier density InO_x:H

films with R[O_2] of 2% decreased to 1.6×10^{17} cm^{-3} at the annealing temperature of 400 ℃. Nondegenerate InO_x:H films can be obtained at low temperature (below 250 ℃) with R[O_2] higher than 3% during deposition. Next, the cause of the difference in metal-semiconductor transition temperature was investigated.

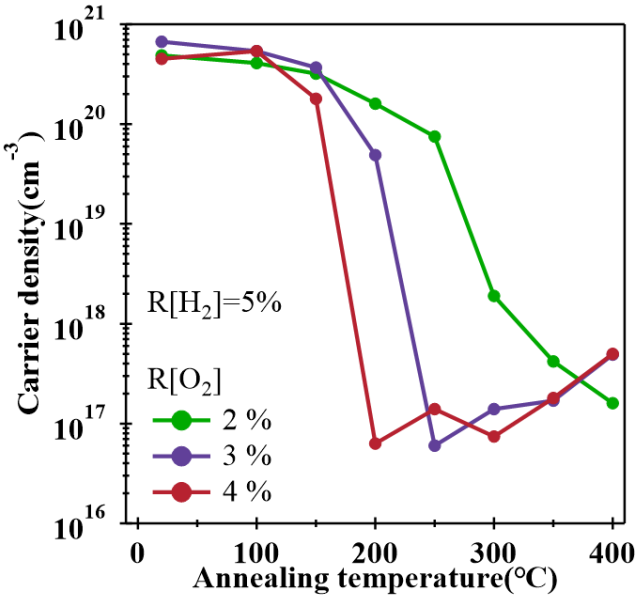

Figure 5. 18 Carrier density of InO_x:H (R[O_2] = 2 ~ 4%) films as a function of annealing temperature (in air). R[H_2] was set at 5%. Ramp and hold time are 2 and 60 min, respectively.

Figure 5. 19 shows carrier density of InO_x:H films as a function of annealing time. Carrier density of InO_x:H films with R[O_2] of 2% decreased by half an order of magnitude within 3 min. Then carrier density exhibited constant value with the extension of annealing time. Carrier density of InO_x:H films with R[O_2] of 3% decreased from 6.7×10^{20} to ~10^{17} cm^{-3} gradually during 30 min. Carrier density of films with R[O_2] of 4% decreased rapidly to 2.5×10^{16} cm^{-3} within 5 min. Then carrier density ranged from 1.9×10^{16} cm^{-3} to 1.4×10^{17} cm^{-3} with annealing time extending. The results indicated that

the increase of R[O_2] during deposition decreased the metal-semiconductor transition temperature, making it possible to obtain nondegenerate InO_x:H films at below 250 ℃. In addition, the increase of R[O_2] accelerated the decrease of carrier density during annealing in air.

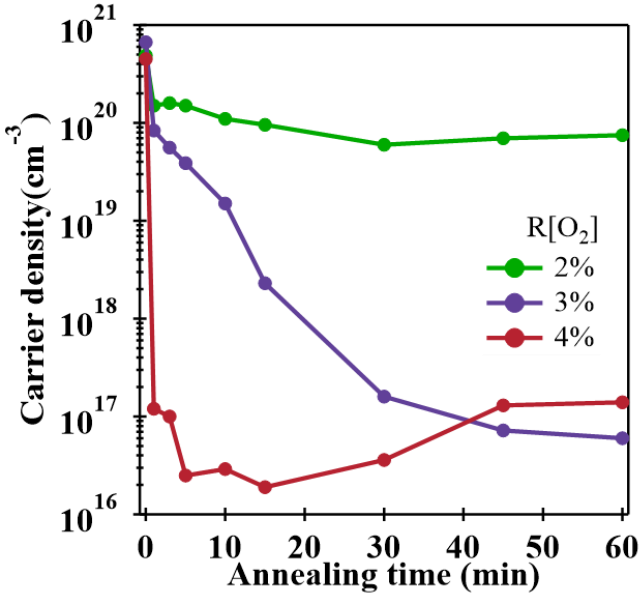

Figure 5. 19 Carrier density of InO_x:H (R[O_2] = 2 ~ 4%) films as a function of annealing time (in air). R[H_2] was set at 5%. Annealing temperature is 250 ℃, respectively.

Figure 5. 20 shows O 1s HAXPES spectra obtained from InO_x:H films with R[O_2] ranging from 2% to 4% after annealing in air. Relative area ratios of M-O, V_O, and -OH in the InO_x:H films after annealing in air are summarized in Table 5. 7. InO_x:H films with R[O_2] of 2% exhibited obviously higher R[Vo] of 12.68% than that (~2.96%) in InO_x:H films with R[O_2] of 3 and 4%, corresponding to the high carrier density of InO_x:H films with R[O_2] of 2%. The deficiency of intrinsic oxygen suppressed the passivation of V_O even after annealing in air.

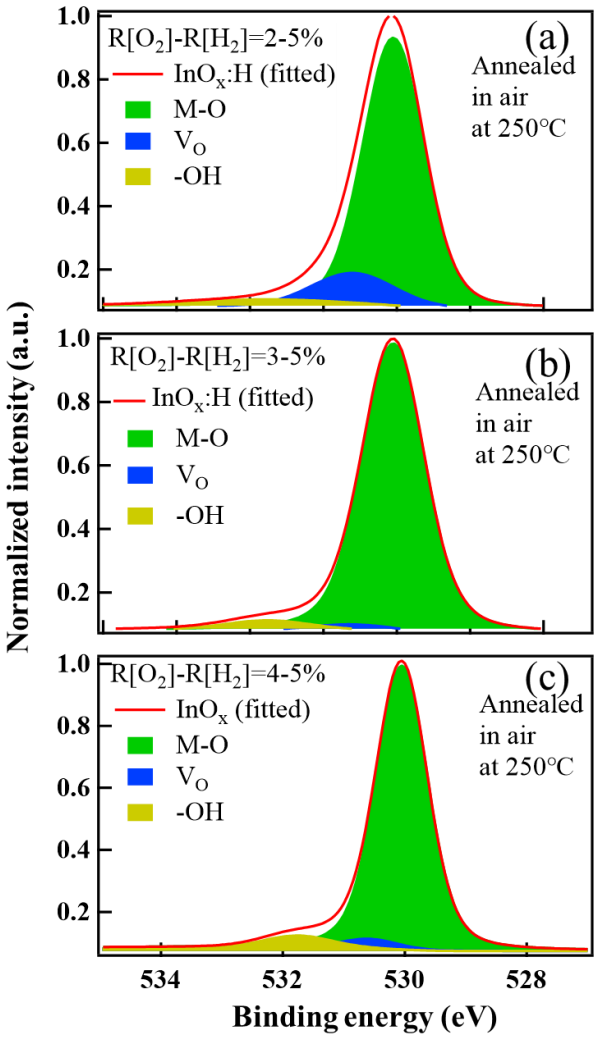

Figure 5. 20 O 1s HAXPES spectra obtained from InO_x:H films annealed in air at 250 ℃ with R[O_2] of (a) 2%, (c) 3%, and (e) 4%.

Table 5. 7 Relative area ratio of the M-O, V_O, and -OH in the InO_x:H films with R[O_2] ranging from 2~4% before and after annealing in air for 60 min after deconvolution of O 1s spectra.

	R[H_2] (%)	R[M-O] (%)	R[Vo] (%)	R[-OH] (%)
Annealed in air	2	82.50	12.68	4.83
	3	92.38	2.68	4.94
	4	92.14	3.23	4.63

As discussed above, the extremely low R[Vo] is essential for the formation of nondegenerate InO_x:H films. Figure 5. 21 shows the valence band configuration from E_F of the InO_x:H films with $R[O_2]$ ranging from 2 to 4% after annealing for 60 min in air at 250 ℃. A peak in near E_F states was clearly observed for InO_x:H films with $R[O_2]$ of 2%. Near E_F states decreased with the increase of $R[O_2]$ after annealing in air. Nondegenerate InO_x:H films with $R[O_2]$ of 3% and 4% show almost the same intensity in near E_F states. In addition to extremely low R[Vo], sufficient intrinsic oxygen in as-deposited films is another critical factor in the fabrication of nondegenerate InO_x:H film at low temperature.

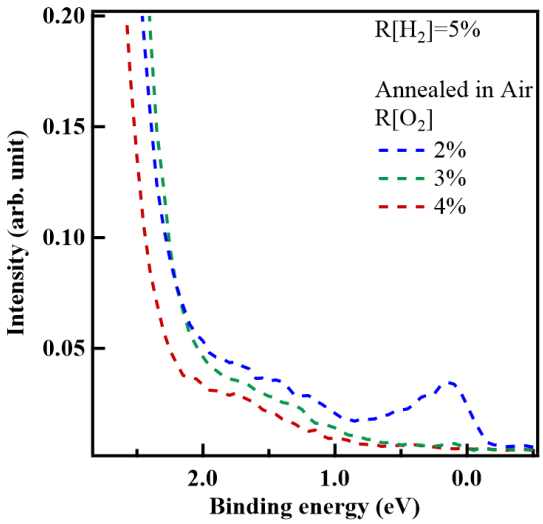

Figure 5. 21 HAXPES spectra around the band gap of the InO_x:H films with $R[O_2]$ ranging from 2 ~ 4% after annealing for 60 min in air at 250 ℃. $R[H_2]$ was fixed at 4%.

Figure 5. 22 shows SEM surface views of InO_x:H films before and after annealing in air for 5 and 60 min. All the films can be converted to polycrystalline phase with grain size ranging from 0.55 μm to 0.66 μm. InO_x:H films with sufficient intrinsic oxygen exhibited a clear grain boundary with annealing time extending to 60 min. In contrast, it is noteworthy that the InO_x:H film with $R[O_2]$ of 2% exhibits a change in grain boundary

with annealing time extending. Clear grain boundary was observed for InO_x:H films with $R[O_2]$ of 2% after annealing for 5 min, which is the same as other InO_x:H films with $R[O_2]$ of 3% and 4%. However, as the annealing time was extended, the grain boundary became blurred, as shown in Figure 5. 22(g). It is considered that the accumulation of oxygen in the annealing ambient at the film surface leads to a blurring of the grain boundary, thereby hindering the diffusion of oxygen from the annealing gas into the film. Therefore, the V_O in InO_x:H film with $R[O_2]$ of 2% was not passivated completely after annealing in air, resulting in a high carrier density of 10^{20} cm^{-3}.

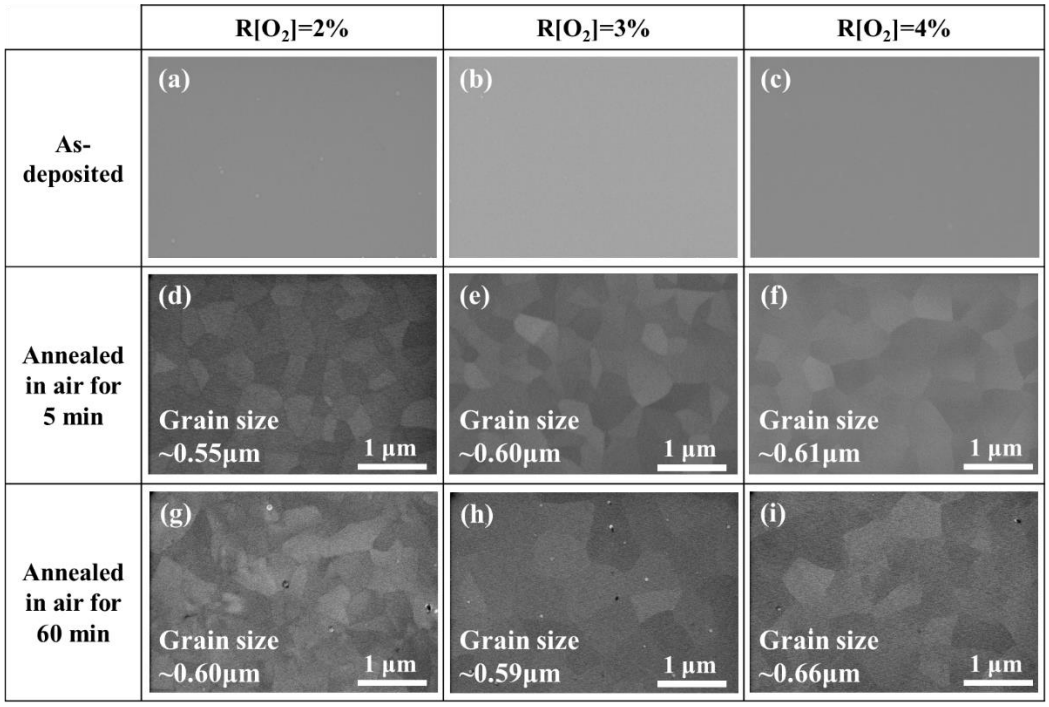

Figure 5. 22 SEM surface views of as-deposited InO_x:H films with $R[O_2]$ of (a) 2%, (b) 3% and (c) 4%; annealed InO_x:H films in N_2 with $R[O_2]$ of (d) 2%, (e) 3% and (f) 4%; annealed InO_x:H films in air with $R[O_2]$ of (g) 2%, (h) 3% and (i) 4%. Annealing temperature is 250 ℃.

5.5 Conclusion

In this chapter, nondegenerate poly-InO_x:H films were formed by rapid SPC in air. The chemical composition, structure, and electrical properties of both the InO_x and InO_x:H films were investigated to discuss the effect of hydrogen on the metal-semiconductor during the deposition process. Hydrogen in InO_x:H films act as shallow donors, providing free carriers, resulting in degenerate as-deposited InO_x:H films with higher carrier density than InO_x films. Ionized H, which provided a portion of carrier, was desorbed as H_2O at temperature of 200 ℃, causing reduction of carrier density. InO_x:H films exhibited higher relative area ratio of V_O, indicating that the doping of H promoted the formation of V_O. Significant reduction in oxygen vacancy were observed after annealing in N_2. Oxygen vacancy was passivated by crystal rearrangement in N_2, causing the decrease in carrier density. Oxygen vacancy decreased with the decrease of near E_F states, indicating that oxygen vacancy acts as shallow donor in InO_x:H films.

Carrier density of the InO_x:H films significantly decreased to ~10^{17} cm^{-3} after annealing in air at 250 ℃. Relative area ratio of V_O of InO_x:H films shows a more substantial decrease compared to films annealed in air, decreasing from 37.10% to 3.23%, with near E_F states decreasing to extreme low state. In contrast, the near VBM states increased with annealing. Extremely low relative area ratio of the V_O and the suppression of carriers by -OH jointly result in the formation of nondegenerate InO_x:H films.

The intrinsic oxygen for InO_x:H films was controlled by deposition conditions. The deficiency of intrinsic oxygen increased the metal-semiconductor transition temperature. InO_x:H films with R[O_2] of 2% remained in a degenerate state at a low annealing temperature of 250 ℃. We found that grain boundaries of InO_x:H films with deficient intrinsic oxygen shown on the film surface become blurred with the increase of annealing

time (in air). The diffusion of oxygen from the annealing gas into the film was hindered, leading to incomplete passivation of V_O during annealing in air. These unpassivated V_O act as shallow donor, resulting in high carrier density.

References

1. Wong, J.; Huang, J.L.; Eggleston, B.; Green, M.A.; Kunz, O.; Evans, R.; Keevers, M.; Egan, R.J. Lifetime Limiting Recombination Pathway in Thin-Film Polycrystalline Silicon on Glass Solar Cells. *Journal of Applied Physics* **2010**, *107*, doi:10.1063/1.3429206.
2. Park, J.-S.; Kim, H.; Kim, I.-D. Overview of Electroceramic Materials for Oxide Semiconductor Thin Film Transistors. *J Electroceram* **2014**, *32*, 117–140, doi:10.1007/s10832-013-9858-0.
3. Gurlo, A.; Ivanovskaya, M.; Bârsan, N.; Schweizer-Berberich, M.; Weimar, U.; Göpel, W.; Diéguez, A. Grain Size Control in Nanocrystalline In2O3 Semiconductor Gas Sensors. *Sens. Actuators B Chem.* **1997**, *44*, 327–333, doi:10.1016/S0925-4005(97)00199-8.
4. Petti, L.; Münzenrieder, N.; Vogt, C.; Faber, H.; Büthe, L.; Cantarella, G.; Bottacchi, F.; Anthopoulos, T.D.; Tröster, G. Metal Oxide Semiconductor Thin-Film Transistors for Flexible Electronics. *Applied Physics Reviews* **2016**, *3*, 021303, doi:10.1063/1.4953034.
5. Nomura, K.; Ohta, H.; Takagi, A.; Kamiya, T.; Hirano, M.; Hosono, H. Room-Temperature Fabrication of Transparent Flexible Thin-Film Transistors Using Amorphous Oxide Semiconductors. *Nature* **2004**, *432*, 488–492, doi:10.1038/nature03090.
6. Koida, T.; Fujiwara, H.; Kondo, M. High-Mobility Hydrogen-Doped In2O3 Transparent Conductive Oxide for a-Si:H/c-Si Heterojunction Solar Cells. *Sol. Energy Mater. Sol. Cells* **2009**, *93*, 851–854, doi:10.1016/j.solmat.2008.09.047.
7. Koida, T.; Sai, H.; Kondo, M. Application of Hydrogen-Doped In2O3 Transparent Conductive Oxide to Thin-Film Microcrystalline Si Solar Cells. *Thin Solid Films* **2010**, *518*, 2930–2933, doi:10.1016/j.tsf.2009.08.060.
8. Macco, B.; Kessels, W.M.M. (Erwin) Atomic Layer Deposition of Conductive and Semiconductive Oxides. *Applied Physics Reviews* **2022**, *9*, 041313, doi:10.1063/5.0116732.
9. Nistor, M.; Gherendi, F.; Perrière, J. Degenerate and Non-Degenerate In2O3 Thin Films by Pulsed Electron Beam Deposition. *Materials Science in Semiconductor Processing* **2018**, *88*, 45–50, doi:10.1016/j.mssp.2018.07.024.
10. Yang, B.; Li, P.; Chen, Z.; Xu, H.; Fu, C.; Ding, X.; Zhang, J. Effect of Titanium Cation Doping on the Performance of In2O3 Thin Film Transistors Grown via

Atomic Layer Deposition. *Coatings* **2023**, *13*, 605, doi:10.3390/coatings13030605.

11. Mitoma, N.; Aikawa, S.; Ou-Yang, W.; Gao, X.; Kizu, T.; Lin, M.-F.; Fujiwara, A.; Nabatame, T.; Tsukagoshi, K. Dopant Selection for Control of Charge Carrier Density and Mobility in Amorphous Indium Oxide Thin-Film Transistors: Comparison between Si- and W-Dopants. *Applied Physics Letters* **2015**, *106*, 042106, doi:10.1063/1.4907285.
12. Kim, Y.G.; Kim, T.; Avis, C.; Lee, S.-H.; Jang, J. Stable and High-Performance Indium Oxide Thin-Film Transistor by Ga Doping. *IEEE Transactions on Electron Devices* **2016**, *63*, 1078–1084, doi:10.1109/TED.2016.2518703.
13. Liang, L.Y.; Liu, Z.M.; Cao, H.T.; Xu, W.Y.; Sun, X.L.; Luo, H.; Cang, K. The Structural, Optical and Electrical Properties of Y-Doped SnO Thin Films and Their p-Type TFT Application. *J. Phys. D: Appl. Phys.* **2012**, *45*, 085101, doi:10.1088/0022-3727/45/8/085101.
14. Magari, Y.; Kataoka, T.; Yeh, W.; Furuta, M. High-Mobility Hydrogenated Polycrystalline In2O3 (In2O3:H) Thin-Film Transistors. *Nat. Commun.* **2022**, *13*, 1078, doi:10.1038/s41467-022-28480-9.
15. Cho, I.-T.; U, M.; Song, S.-H.; Lee, J.-H.; Kwon, H.-I. Effects of Air-Annealing on the Electrical Properties of p-Type Tin Monoxide Thin-Film Transistors. *Semicond. Sci. Technol.* **2014**, *29*, 045001, doi:10.1088/0268-1242/29/4/045001.
16. Velichko, R.; Magari, Y.; Furuta, M. Defect Passivation and Carrier Reduction Mechanisms in Hydrogen-Doped In-Ga-Zn-O (IGZO:H) Films upon Low-Temperature Annealing for Flexible Device Applications. *Materials* **2022**, *15*, 334, doi:10.3390/ma15010334.
17. Takagi, A.; Nomura, K.; Ohta, H.; Yanagi, H.; Kamiya, T.; Hirano, M.; Hosono, H. Carrier Transport and Electronic Structure in Amorphous Oxide Semiconductor, a-InGaZnO4. *Thin Solid Films* **2005**, *486*, 38–41, doi:10.1016/j.tsf.2004.11.223.
18. Abliz, A. Effects of Hydrogen Plasma Treatment on the Electrical Performances and Reliability of InGaZnO Thin-Film Transistors. *Journal of Alloys and Compounds* **2020**, *831*, 154694, doi:10.1016/j.jallcom.2020.154694.
19. Park, H.-W.; Choi, M.-J.; Jo, Y.; Chung, K.-B. Low Temperature Processed InGaZnO Thin Film Transistor Using the Combination of Hydrogen Irradiation and Annealing. *Applied Surface Science* **2014**, *321*, 520–524, doi:10.1016/j.apsusc.2014.09.180.
20. Kim, Y.J.; Park, J.C.; Lee, H.-N. Effects of Ion Implantation Doping on the

Characteristics of Amorphous Indium Gallium Zinc Oxide Thin Films. *Science of Advanced Materials* **2016**, *8*, 267–271, doi:10.1166/sam.2016.2477.

21. Kamada, Y.; Fujita, S.; Hiramatsu, T.; Matsuda, T.; Furuta, M.; Hirao, T. Analysis of Subthreshold Photo-Leakage Current in ZnO Thin-Film Transistors Using Indium-Ion Implantation. *Solid-State Electronics* **2010**, *54*, 1392–1397, doi:10.1016/j.sse.2010.04.001.
22. Sil, A.; Avazpour, L.; Goldfine, E.A.; Ma, Q.; Huang, W.; Wang, B.; Bedzyk, M.J.; Medvedeva, J.E.; Facchetti, A.; Marks, T.J. Structure–Charge Transport Relationships in Fluoride-Doped Amorphous Semiconducting Indium Oxide: Combined Experimental and Theoretical Analysis. *Chem. Mater.* **2020**, *32*, 805–820, doi:10.1021/acs.chemmater.9b04257.
23. Song, A.; Park, H.-W.; Chung, K.-B.; Rim, Y.S.; Son, K.S.; Lim, J.H.; Chu, H.Y. Modulation of the Electrical Properties in Amorphous Indium-Gallium Zinc-Oxide Semiconductor Films Using Hydrogen Incorporation. *Applied Physics Letters* **2017**, *111*, 243507, doi:10.1063/1.5003186.
24. Nomura, K.; Kamiya, T.; Ohta, H.; Hirano, M.; Hosono, H. Defect Passivation and Homogenization of Amorphous Oxide Thin-Film Transistor by Wet O_2 Annealing. *Applied Physics Letters* **2008**, *93*, 192107, doi:10.1063/1.3020714.
25. Kataoka, T.; Magari, Y.; Makino, H.; Furuta, M. Nondegenerate Polycrystalline Hydrogen-Doped Indium Oxide (InOx:H) Thin Films Formed by Low-Temperature Solid-Phase Crystallization for Thin Film Transistors. *Materials* **2022**, *15*, 187, doi:10.3390/ma15010187.
26. Yuan, D.; Liu, W.; Zhu, X. Efficient and Air-Stable n-Type Doping in Organic Semiconductors. *Chem. Soc. Rev.* **2023**, *52*, 3842–3872, doi:10.1039/D2CS01027E.

Chapter 6

Conclusion

6.1 Findings of this study

Chapter 3. Improvement of electrical properties of indium oxide films by hydrogen doping

In this chapter, InO_x and InO_x:H films with various oxygen and hydrogen flow ratios were deposited by RF magnetron sputtering. The structural properties, electrical properties, and chemical bonding states of both the InO_x and InO_x:H films were investigated to clarify the effect of the gas flow ratio during deposition.

Hydrogen acts as shallow donor to adjust electrical properties. Hydrogen doped in InO_x film acted as interstitial H and -OH, resulting in changes in as-deposited InO_x film. Furthermore, the introduction of hydrogen promoted the formation of V_O, resulting in a further increase in the carrier density. Impurity scattering decreased Hall mobility for as-deposited film. The oxygen adjusted the ionized interstitial H and free carrier in as-deposited films. At a low oxygen flow ratio, ionized H increased, resulting in the decrease of Hall mobility due to increasing impurity scattering.

Solid phase crystallization occurred at the annealing temperature of ~200 ℃ in N_2 for InO_x:H films, resulting in a significant increase of Hall mobility to 60~70 cm^2/Vs. In contrast, the Hall mobility of InO_x films did not exhibit an enormous increase after annealing. Nanocrystalline phase with a large area of grain boundary. The introduction of hydrogen caused dramatical structural rearrangements by SPC, leading to a large grain size in polycrystalline film. The oxygen has a significant impact on the SPC process. A high $R[O_2]$ promoted the passivation of oxygen vacancies during SPC and reduced the

SPC temperature. Oxygen enhanced the stability of hydrogen in the film, leading to the reduction of H_2 and H_2O desorption during the SPC process, while increasing the relative area ratio of -OH in the film.

After annealing, hydrogen desorbed from the InO_x:H films in the form of H_2 and H_2O, leading to decrease in relative area ratio of V_O. Ionized H and V_O were passivated by SPC, causing the increase in Hall mobility. In addition, the large grain size of InO_x:H films was considered one of the causes of high mobility. However, excessive H or O will result in the reduction of Hall mobility due to impurity scattering and -OH, respectively. Therefore, to obtain InO_x:H films with high Hall mobility, it is essential to achieve an optimal equilibrium between scattering suppression and -OH.

Chapter 4. Solid phase crystallization mechanism in Hydrogen-doped InO_x films

In this chapter, poly-InO_x and poly-InO_x:H films were formed by rapid SPC. The structure and electrical properties of both the InO_x and InO_x:H films were investigated to clarify the mechanism of phase transition of 30-nm-thick amorphous InO_x:H into poly-InO_x:H films during rapid SPC process.

Hall mobility of the InO_x:H films significantly increased to 83 cm^2/Vs after annealing in N_2 at 250 ℃ for 3 min, whereas that of the InO_x films increased to 47 cm^2/Vs due to the difference in the grain size. We found that H_2-doping in InO_x:H films reduced a nucleation density at 250 ℃ from 4.1 to 1.1 μm^{-2}, resulting in an increase of a grain size and Hall mobility of the poly-InO_x:H films. The crystalline volume fraction in the InO_x:H films annealed at T_A of 250 ℃ without hold time decreased with an increase of the temperature ramp rate. The lateral growth rate from the nucleus was estimated to be 220 nm/min for the InO_x:H film. Thus, an amorphous InO_x:H film could be converted to a

poly-InO_x:H film within 3 min owing to a fast lateral growth rate from the nucleus. Hall mobility exhibited ~80 cm^2/Vs for the poly-InO_x:H film with the hold time of more than 3 min. In addition, almost the same grain size, Hall mobility, and carrier density could be obtained from the poly-InO_x:H films after annealing at 250 ℃ for 3 min, irrespective of the ramp rate. These results indicated that SPC poly-InO_x:H films have a wide range of processing windows, which is also beneficial for the industrial applications. Low-temperature (250 ℃) and fast lateral growth are great advantages of the poly-InO_x:H film for enhancing the performance of flexible devices.

Chapter 5. Metal-semiconductor transition mechanism of InO_x:H film

In this chapter, nondegenerate poly-InO_x:H films were formed by rapid SPC in air. The chemical composition, structure, and electrical properties of both the InO_x and InO_x:H films were investigated to discuss the effect of hydrogen on the metal-semiconductor during the deposition process.

Hydrogen in InO_x:H films act as shallow donors, providing free carriers after ionization, resulting in degenerate as-deposited InO_x:H films with higher carrier density than InO_x films. Ionized H, which provided a portion of the carrier, was desorbed as H_2O at a temperature of 200 ℃, causing a reduction of carrier density.

H promoted the formation of V_O. V_O, acting as shallow donor, was passivated by crystal rearrangement by SPC, causing the decrease in carrier density. The change in near E_F states reflected the change of V_O. Carrier density decreased with the decrease of V_O and near E_F states.

Carrier density of the InO_x:H films significantly decreased to ~10^{17} cm^{-3} after annealing in air at 250 ℃, obtaining nondegenerate InO_x:H films. Relative area ratio of V_O of

InO_x:H films shows a more substantial decrease compared to films annealed in air, decreasing from 37.10% to 3.23%, with near E_F states decreasing to extreme low state. In contrast, the near VBM states increased with annealing. Extremely low relative area ratio of the V_O and the suppression of carriers by -OH jointly result in the formation of nondegenerate InO_x:H films.

The deficiency of intrinsic oxygen increased the metal-semiconductor transition temperature. InO_x:H films with R[O_2] of 2% remained in a degenerate state at a low annealing temperature of 250 ℃. We found that grain boundaries of InO_x:H films with deficient intrinsic oxygen shown on the film surface become blurred with the increase of annealing time (in air). The diffusion of oxygen from the annealing gas into the film was hindered, leading to incomplete passivation of V_O during annealing in air. These unpassivated V_O act as shallow donor, resulting in high carrier density.

6.2 Summary

The purpose of this study was to investigate the effects of H_2 doping to improve the electrical properties of indium oxide and to establish the mechanism of solid phase crystallization and metal-semiconductor transition.

From the research results described in Chapter 3, interstitial hydrogen and oxygen vacancy act as shallow donors, providing carrier after ionization. Ionized impurities (oxygen vacancy, H^+) increase impurity scattering, decreasing the Hall mobility of as-deposited InO_x:H film. SPC occurred during annealing in N_2, resulting in increase of Hall mobility. Interstitial H was desorbed as H_2O during SPC. Large grains were obtained for H-doped poly-InO_x films, which was one cause of high Hall mobility.

In Chapter 4, Hall mobility of the InO_x:H films significantly increased to 83 cm^2/Vs

after annealing in N_2 at 250 ℃ for 3 min, whereas that of the InO_x films increased to 47 cm^2/Vs due to the difference of the grain size. H_2-doping in InO_x:H films reduced a nucleation density at 250 ℃ from 4.1 to 1.1 μm^{-2}, resulting in an increase of a grain size and Hall mobility of the poly-InO_x:H films. The lateral growth rate from the nucleus was estimated to be 220 nm/min for the InO_x:H film. Thus, an amorphous InO_x:H film could be converted to a poly-InO_x:H film within 3 min owing to a fast lateral growth rate from the nucleus.

In Chapter 5, Ionization hydrogen provided carrier, resulting in degenerate as-deposited InO_x:H films with higher carrier density than InO_x films. Decrease in ionization hydrogen and V_O causes carrier density reduction of InO_x:H films with the reduction in near E_F states.

Nondegenerate poly-InO_x:H films were formed by rapid SPC in air. Relative area ratio of V_O of InO_x:H films shows a more substantial decrease compared to films annealed in air, with near E_F states decreasing to extreme low state. In contrast, the near VBM states increased with annealing. Extremely low relative area ratio of the V_O and the suppression of carriers by -OH jointly result in the formation of nondegenerate InO_x:H films.

Intrinsic oxygen in InO_x:H films, controlled by deposition conditions, plays an important role in the metal-semiconductor transition at low temperature. Degenerate InO_x:H films with sufficient intrinsic oxygen can be converted to a nondegenerate state after annealing in air at temperature below 250 ℃.

Research Achievements

1) X, Wang, Yusaku Magari, and Mamoru Furuta. “Nucleation and grain growth in low-temperature rapid solid-phase crystallization of hydrogen-doped indium oxide.”*Japanese Journal of Applied Physics* 63.3 (2024): 03SP38. (WQS-Q4)

2) Okamoto, N., Wang, X., Morita, K., Kato, Y., Alom, M. M., Magari, Y., & Furuta, M. “Uniformity and Reliability of Enhancement-mode Polycrystalline Indium Oxide Thin Film Transistors formed by Solid-phase Crystallization.” *IEEE Electron Device Letters*. (2024)(WQS-Q1)

Conference Presentations

1) Xiaoqian Wang, Mamoru Furuta, “Rapid Thermal Crystallization of H-doped InO_x for Thin Film Transistors”, The 55th Solid State Device and Materials, Nagoya Congress Center, September 5-8,2023, E-5-03.(Oral, English)

2) Xiaoqian Wang, Mamoru Furuta, “Rapid Thermal Crystallization of H-doped InO_x for Thin Film Transistors”, The 3rd MRM2023/IUMRS-ICA 2023, Kyoto International Conference Center, December 11-16, 2023, D1-O403-04. (Oral, English)

3) Xiaoqian Wang, Mamoru Furuta, “Non-degenerate Semiconductor Polycrystalline InO_x:H film for Thin-Film Transistors formed by Solid-phase Crystallization”, The 24th IMID 2024, ICC JEJU, JEJU ISLAND, KOREA, August 20-23, 2024, P1-082. (Poster, English)

4) Xiaoqian Wang, Mamoru Furuta, “Metal–semiconductor transition of hydrogen-doped In2O3 via solid-phase crystallization”, The 70th JSAP Spring Meeting 2023, Yotsuya Campus, Sophia University + Online, March 15-18,2023, 15p-E102-6 (Oral, Japanese)

5) Xiaoqian Wang, Mamoru Furuta, “Rapid Thermal Crystallization of H-doped InO_x for Thin Film Transistors”, The 84th JSAP Autumn Meeting 2023, Kumamoto-Jo Hall + Online, September 19-23,2023, 19p-A302-7. (Oral, Japanese)

Acknowledgement

I would like to express my sincere thanks to everyone who contributed to the successful completion of my doctoral research and the preparation of this thesis. This journey has been both highly rewarding and challenging, and it would not have been feasible without the support, guidance, and encouragement of numerous individuals and institutions.

First and foremost, I would like to extend my deepest gratitude to my supervisor, *Prof. Mamoru Furuta*, for giving me the opportunity to take this PhD journey at Kochi University of Technology. His insightful guidance, unwavering support, and constructive criticism have been invaluable throughout this process. He not only imparted knowledge and research techniques but also instilled in me a passion for inquiry and a drive for excellence. I have gained a greater understanding of the necessity and importance of these details in an academic research methodology.

I would like to express my very sincere gratitude to *Prof. Norbert Frühauf, Prof.Chaoyang Li, Prof. Toshiyuki Kawaharamura, and Prof. Hisao Makino* for their critical evaluations, thoughtful suggestions, and diverse perspectives that have significantly contributed to the refinement and depth of my work. Their expertise and guidance have been instrumental in broadening my understanding of the field and in improving the overall quality of this thesis.

I am also very thankful for the research support from Spring-8. The HAXPES analysis was performed at the BL09XU of SPring-8 with the approval of the Japan Synchrotron Radiation Research Institute (JASRI) (Proposal No. 2022A1301, 2023A1711, and 2024B1577). The EBSD analysis was supported by the Advanced Research Infrastructure for Materials and Nanotechnology in Japan (ARIM) of the Ministry of Education, Culture, Sports, Science and Technology (MEXT), Japan (Proposition No. JPMXP1223HK0102).

SPring-8 and Hokkaido University. HAXPES and EBSD were measured, respectively. This work was partly supported by JSPS KAKENHI Grant Number 22K04200 and 2023A171. The EBSD measurement was supported by "Advanced Research Infrastructure for Materials and Nanotechnology in Japan (ARIM)" of the Ministry of Education, Culture, Sports, Science and Technology (MEXT). Proposal Number JPMXP1223HK0102.

Thanks to all of my friends and lab members. Ms. Hu Chengmi supported me a lot in my daily life. Lab members helped me a lot in my research. Their friendship has provided a much-needed balance to the demands of academic life, offering moments of joy, laughter, and relaxation. Your companionship has made this experience even more meaningful, and I am fortunate to have such wonderful friends by my side.

I am eternally grateful to my parents and my brother, for their unconditional love, support, patience, and encouragement. I wish my father could be proud of me.

Finally, my sincere thanks to the doctor financial support of the scholarship from China Scholarship Council and KUT.

Kochi University of Technology,

Graduate School of Engineering

2025 March 06